

Reports

1982

Seasat SAR test of the Virginian Sea Wave Climate Model

John C. Munday Jr.
Virginia Institute of Marine Science

Christopher S. Welch
Virginia Institute of Marine Science

George R. Mapp
Virginia Institute of Marine Science

Follow this and additional works at: <https://scholarworks.wm.edu/reports>

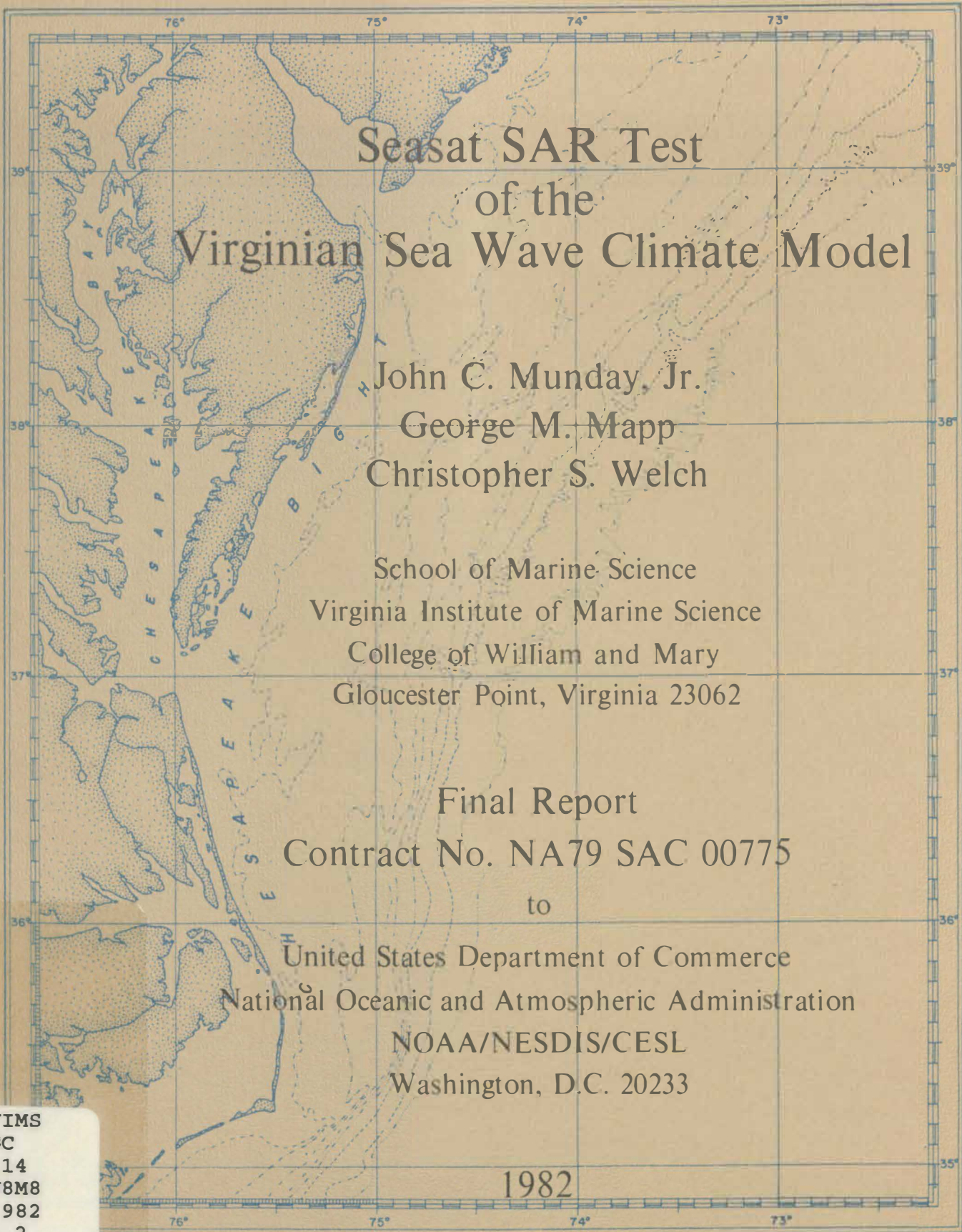


Part of the [Oceanography Commons](#)

Recommended Citation

Munday, J. C., Welch, C. S., & Mapp, G. R. (1982) Seasat SAR test of the Virginian Sea Wave Climate Model. Virginia Institute of Marine Science, William & Mary. <https://doi.org/10.25773/er2d-5h34>

This Report is brought to you for free and open access by W&M ScholarWorks. It has been accepted for inclusion in Reports by an authorized administrator of W&M ScholarWorks. For more information, please contact scholarworks@wm.edu.



Seasat SAR Test of the Virginian Sea Wave Climate Model

John C. Munday, Jr.
George M. Mapp
Christopher S. Welch

School of Marine Science
Virginia Institute of Marine Science
College of William and Mary
Gloucester Point, Virginia 23062

Final Report
Contract No. NA79 SAC 00775

to

United States Department of Commerce
National Oceanic and Atmospheric Administration
NOAA/NESDIS/CESL
Washington, D.C. 20233

1982

VIMS
GC
214
N8M8
1982
c. 2

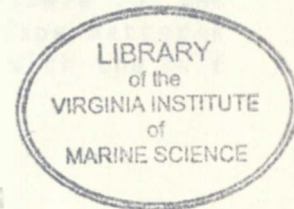
VIMS
GC
214
N8 M8
1982
C.2

Seasat SAR Test of the Virginian Sea Wave Climate Model

John C. Munday Jr.

George M. Mapp

Christopher S. Welch



School of Marine Science
Virginia Institute of Marine Science
College of William and Mary
Gloucester Point, Virginia 23062
804/642-2111

Final Report
Contract No. NA79 SAC 00775

to

United States Department of Commerce
National Oceanic and Atmospheric Administration
National Earth Satellite Data and Information Service
Climate and Earth Sciences Laboratory
NOAA/NESDIS/CES1
Oceanic Sciences Branch
Code E/RA13
Suitland Professional Center
Washington, D.C. 20233
301/763-4244

1982

ABSTRACT

Coastal wave refraction imaged by the Seasat Synthetic Aperture Radar is compared to simulations produced by the Virginian Sea Wave Climate Model. Seasat SAR passes 974 at Cape Hatteras, and 974 and 1404 at Long Island, were examined using OFT and ZTS methods. Results generally confirm the validity of linear wave theory in modeling of shallow-water wave refraction --roughly half the deviations between VSWCM and SAR data for direction and wavelength are within 2 degrees and 10 meters. Convergence of wave orthogonals is found in predicted caustic regions. Available bathymetric data were adequate for the analysis. Some details in the pattern of deviations near Cape Hatteras suggested current shear and tidal effects associated with the Gulf Stream.

ACKNOWLEDGMENTS

We thank Mr. Pat DeLeonibus of NOAA for his support of this project. For assistance in data acquisition and analysis, we thank Mr. Dave Lichy, Army Corps of Engineers, and Dr. Robert Beal, Applied Physics Laboratory, Johns Hopkins University. Dr. Victor Goldsmith assisted in early stages of the project. At the Virginia Institute of Marine Science, special thanks go to Mr. Charles Alston, Mr. Kevin Kiley, and Ms. Carolyn Sutton, who contributed to data reduction and model simulations, and Ms. Cynthia Gaskins and Ms. Beth Marshall who typed the many drafts.

TABLE OF CONTENTS

	Page
ABSTRACT	ii
ACKNOWLEDGMENTS	iii
FIGURES	vi
TABLES	x
INTRODUCTION	1
METHODS AND MATERIALS	5
I. Introduction	5
II. The Virginian Sea Wave Climate Model	5
A. Wave Refraction Model	5
B. The VSWCM Grid	8
C. Deviation of Great Circle Lines from Spherical Geometry	12
D. Wave Ray Plotting	12
III. SAR Image Data Extraction	16
A. Processing	16
B. Geometric Characteristics	16
C. Sampling Locations and Areas	16
D. Slant Range Scale Distortion	19
1. Introduction	19
2. Error in Range	19
3. Error in Wavelength and Direction	24
4. Errors from Curvature of Rays Within a Sampling Subimage	24
E. Techniques for Measuring Wavelength and Direction	24
1. Crest Counting Along an Orthogonal	28
2. Optical Fourier Transform (OFT) Method	28
3. Zoom Transfer Scope (ZTS) Method	30
4. Accuracy and Precision of OFT and ZTS Measurements	32
a. Data Sets for OFT Intercalibration and Method Intercomparison	34
b. Classification and Comparison of Data Sets	34
c. Intercalibration of OFT Measurements	36
d. Comparison of ZTS with OFT Measurements	42
e. Precision of ZTS Measurements	49
f. Summary	49

	Page
F. Plotting SAR Data on the VSWCM Grid	51
G. Generation of Rays by Interpolation	52
H. Analysis of Sampling Density	52
1. Introduction	52
2. Field Uniformity Test	55
3. Test of the 1/16 Grid	63
4. Cluster Analysis	63
5. Summary	63
IV. Geometric Errors from Superimposing SAR Imagery onto VSWCM Ray Diagrams	63
RESULTS AND DISCUSSION	69
I. Cape Hatteras	69
A. ZTS Measurements and Interpolated Wave Rays	69
B. Wave Field Simulated by the VSWCM	69
1. VSWCM Runs Initialized with SAR Deep Water Measurements	69
C. Comparison of SAR Observed Field with VSWCM Simulated Field	83
1. Superposed SAR Vectors and VSWCM Rays	83
2. Caustics	102
3. Superposition of SAR Interpolated Ray Diagram and VSWCM Ray Diagram	103
4. Wavelength Versus Ray Distance Plots	116
5. Shoreline Ray Density	116
D. General Summary for the Cape Hatteras Region	125
II. Long Island	125
A. Pass Selection	125
B. Pass 1404, Long Island	126
C. Pass 974, Long Island	131
CONCLUSION	143
COMMENTS ON FURTHER ANALYSIS	144
REFERENCES	147
APPENDICES	149
A. Calculating ground range at any point on image	151
B. Calculating errors for measured values of wavelength and direction	153
C. VSWCM ray diagrams simulating conditions at Cape Hatteras, 3 September 1978	155
D. Wavelength versus ray distance plots	173
E. Abstracts of previous reports under this project	185

FIGURES

	Page
1. Typical Optical Fourier Transforms from pass 974, Cape Hatteras	7
2. Wave spectrum at CERC pier concurrent with pass 974	9
3. Thermal IR image from HCCM satellite for 24 August 1978	11
4. Bathymetry near Cape Hatteras	13
5. Computer-contoured bathymetry near Cape Hatteras	15
6. Seasat SAR imagery of Cape Hatteras	17
7. Estimate of location error from mapping the SAR ground swath onto the Mercator projection	18
8. Sampling grid of data extraction points for pass 974, Cape Hatteras	21
9. Variation of inverse range scale factor for SAR subswaths (optically correlated imagery)	23
10. Optical diagram for OFT production	29
11. SAR film overlay with matrix of tangent circles	31
12. Azimuthal grid with Ronchi ruling pattern	33
13. OFT intercalibration results. VIMS OFT vs. CERC OFT. Wavelength	43
14. OFT intercalibration results. VIMS OFT vs. CERC OFT. Direction	44
15. ZTS-OFT intercalibration results. VIMS ZTS vs. CERC OFT. Wavelength	45
16. Comparison of deviations in direction values from different methods, VIMS and CERC data	46
17. Internal VIMS comparison for wavelength data, ZTS vs. OFT. CERC stations	47
18. Internal VIMS comparison for direction data, ZTS vs. OFT. CERC stations	48

	Page
19. Histogram of standard deviation of the mean for ZTS measurements	50
20. Flow chart for interpolating rays of the direction field measured from the SAR imagery	53
21. Impact of the interpolation factor F on ray diagrams	54
22. Hypothetical convergence of interpolated values to measured value for increasing measurement-grid densities ...	56
23. Subset of 30 points chosen for grid density analysis	57
24. Deviations of interpolated direction vs. inverse grid density	60
25. Deviations of interpolated wavelength vs. inverse grid density	61
26. Average deviations of interpolated wavelength and direction vs. inverse grid density	62
27. Distribution of absolute deviations (interpolated vs. measured values) which fail the 60% confidence interval	64
28. Best fit of SAR and VSWCM maps of landforms	66
29. SAR wavelength "vectors" measured with ZTS for Cape Hatteras	71
30. SAR wave ray diagram interpolated from measurements in Figure 29	73
31. Wavelength vectors measured by CERC with OFTs. 11 mm circles	75
32. Wavelength vectors measured by CERC with OFTs. 38 mm circles	77
33. Wavelength vectors measured by ERIM with OFTs. 5 mm squares	79
34. Nominal VSWCM run with initial conditions interpolated from deep water SAR measurements	81
35. Cape Hatteras area divided into zones to facilitate analysis	85
36. Overlay of SAR vectors and VSWCM predicted rays	87
37. Orthogonals from grid stations and extra stations	91

	Page
38. Tracing made with the ZTS of thermal boundaries on HCMM images	93
39. Ocean Frontal Analysis map for September 5, 1978	95
40. Variation of SAR vector directions for offshore stations ...	96
41. Variation of SAR vector wavelengths for offshore stations...	98
42. Histogram of direction deviations (SAR vs. VSWCM) for the area of study	100
43. Contour map of direction deviations (SAR vs. VSWCM) for the area of study	101
44. Orthogonals from additional ZTS measurements in the region of caustics predicted by the VSWCM	105
45. Histogram of orthogonals seaward of the predicted caustic C in Figure 44	107
46. Histogram of orthogonals shoreward of the predicted caustic C in Figure 44	107
47. Overlay of VSWCM predicted rays onto SAR interpolated rays ..	109
48. Collation of best-fit rays from all VSWCM runs	113
49. VSWCM and SAR wavelength values along ray #18	117
50. Artificial shoreline constructed for ray density analysis...	121
51. A composite of ray density at the artificial shoreline for various SAR and VSWCM ray diagrams	123
52. SAR wavelength vectors measured with the ZTS for Long Island, pass 1404	127
53. Histogram of standard deviation of the mean for ZTS measurements	128
54. Histogram of SAR vector directions for offshore stations, Long Island, pass 1404	129
55. VSWCM run with initial conditions obtained from offshore SAR measurements, Long Island, pass 1404	130
56. Histogram of direction deviations (SAR vs. VSWCM) for Long Island, pass 1404	132

	Page
57. Histogram of wavelength deviations (SAR vs. VSWCM) for Long Island, pass 1404	132
58. SAR wavelength vectors measured with the ZTS for Long Island, pass 974	135
59. Histogram of standard deviation of the mean for ZTS measurements, Long Island, pass 974	137
60. VSWCM run with initial conditions obtained from offshore SAR measurements, Long Island, pass 974	139
61. Histogram of direction deviations (SAR vs. VSWCM) for Long Island, pass 974	141
62. Histogram of wavelength deviations (SAR vs. VSWCM) for Long Island, pass 974	142

TABLES

	Page
1. Location errors due to slant range distortion	25
2. Worst case errors in wavelength and direction attributable to slant range distortion	26
3. Typical errors in wavelength and direction attributable to slant range distortion	27
4. Data sets used for method comparison	35
5. Correlation between OFT and ZTS results for partitioned data sets. Partition method: standard deviation of the mean for four replicate ZTS measurements of propagation direction ...	37
a. Pooled VIMS + ERIM subimage locations	37
b. CERC subimage locations	37
c. ERIM subimage locations	38
6. Correlation between OFT and ZTS results for partitioned data sets. Partition method: Qualitative evaluation of OFT signal clarity	39
a. Pooled VIMS + ERIM subimage locations	39
b. CERC subimage locations	39
c. ERIM subimage locations	40
7. Correlation coefficients among ZTS and OFT data sets	41
8. Distance weighting factor F for various grid densities	59
9. Error factors and resultant maximum errors	67
10. Comparison of Best-fit VSWCM Runs for Ray Collinearity and Shoreline Ray Density	115

INTRODUCTION

The Seasat Synthetic Aperture Radar (SAR), despite a short life, has provided the first comprehensive imagery of ocean swell for oceanographic analysis. It produced imagery of ocean swell for the area adjacent to Cape Hatteras, North Carolina, extending from deep water across the continental shelf to the shoreline. In the work described here, measurements of the imaged wave field are compared to wave ray diagrams generated by a computerized wave refraction program originally written by Dobson (1967) and later adapted to the Mid-Atlantic Bight by Goldsmith *et al.* (1974). The later version is called the Virginian Sea Wave Climate Model (VSWCM).

Shuchman *et al.* (1979) compared measurements of wavelength and direction obtained from optically correlated SAR imagery (pass 974, Cape Hatteras) to predicted values from a wave ray diagram constructed by graphical techniques. Bathymetry was taken from a National Ocean Survey nautical chart, which shows minimum values for depths, being primarily a navigational aid. Measured values of wavelength and direction from OFT techniques were in general agreement with predictions, correlation being better for wavelength ($r=0.76$) than for direction ($r=0.55$). Recommendations by Shuchman *et al.* for further analyses included use of more accurate bathymetric data, and accounting for refraction due to ocean currents. A subsequent report from the same ERIM group (Kasischke *et al.*, 1981) addressed these issues and obtained estimates of the Gulf Stream velocity profile using pass 974 SAR data.

For the VSWCM bathymetric grid used in the present study, depths were interpolated at 0.5 nautical mile intervals from National Ocean Survey Hydrographic Sounding sheets (number 8808, 1963, and number 9104, 1970). Also, in the present study, effects of currents have been considered within limits of available data. There were no current measurements available as surface information, nor was there a suitably close Seasat altimeter pass which would have permitted current calculations from orbital data. The altimeter was not operating during the period August 28 to September 6, 1978. Finally, a comprehensive wave ray field is developed from the Seasat data for the area involved. This field is compared to an extensive set of ray diagrams generated using the VSWCM, a set which encompasses all combinations of wavelength and direction values allowed as input from the SAR data, taking into account possible ranges of error in such values.

In performing a comparison of a simulated wave field to the SAR imaged field, a key assumption has been made. That is, the wave field present on the SAR image is an accurate image of nature, and the optical Fourier transforms (OFTs) made from SAR imagery are equivalent to spatial energy spectra:

$$\underline{\Psi}(\underline{k}) = \int \underline{X}(\underline{k}, n) dn \quad (1)$$

where $\underline{\psi}(\underline{k})$ = spatial spectrum, $\underline{x}(\underline{k}, n)$ = spectral energy density, k = spatial wave number, and n = temporal angular frequency of the wave component; see Beal (1981) and Phillips (1981) for further descriptions of spatial energy spectra. This assumption is presently being examined in the literature, and involves the following considerations:

1) There is an incomplete understanding of the effects of both surface winds and orientation of flight line with direction of swell propagation, on the ability of the Seasat SAR to resolve ocean swell (Shuchman et al., 1979; Beal, 1981; Phillips, 1981; Vesecky and Stewart, 1982). SAR is sensitive only to ocean features comparable in size to the wavelength of the emitted beam; that is, for Seasat on the order of 23 cm. Wavelets of this length are classified as small gravity waves. Swell is resolved by the Seasat SAR because these wavelets are modulated in amplitude by underlying swell. However, a variety of other phenomena can influence 23 cm wavelets, such as surface winds and shearing currents.

2) The image transfer function of the SAR is unknown due to the lack of a controlled instrument calibration study. Optical Fourier transforms of SAR imagery have generally been treated as wave energy spectra (Gonzales, 1979; Shuchman et al., 1979; Beal, 1981; Vesecky and Stewart, 1982), based on the assumption that optical density of striping on the imagery corresponding to ocean swell is proportional to wave height. Phillips (1981) has suggested that OFTs are wave slope spectra rather than energy density spectra. If this is true, waves of 100 to 200 meters may be artificially enhanced when OFTs are viewed as energy spectra (Beal, 1981).

3) There is uncertainty in the ability of SAR to produce focused images of waves traveling in the azimuth direction, again due to the lack of a controlled calibration study. The SAR was initially designed to image stationary objects in the azimuth dimension by a Doppler shift mechanism. Motion of ocean swell during the one-second period of aperture synthesis has a defocusing effect on the imaging mechanism (see Raney, 1980). The magnitude of this defocusing is as yet unknown.

4) There is uncertainty in the range of wavelengths for which the Seasat SAR can image ocean swell. This is related to factors discussed in (1) above. Beal (1981) found that an 80 metre component, appearing in spectra from an airborne laser profilometer, failed to appear in digital Fourier transforms of the same area.

Nevertheless, there is evidence that the Seasat SAR has produced accurate images of swell. In a preliminary analysis of data from the GOASEX experiment (Gonzales et al., 1981), OFTs from optically correlated imagery had spectral peaks that were corroborated by: (1) one-dimensional spectra from an accelerometer aboard an NDBO buoy, accurate to ± 15 per cent in wavelength; (2) two-dimensional spectra from a pitch roll buoy, accurate to ± 10 degrees in direction and ± 20 per cent in wavelength; and (3) two-dimensional spectra from an aircraft SAR, accurate to ± 10 degrees for direction and ± 10 metres in wavelength. Likewise, in the DUCK-X experiment (Beal, 1981), OFT analysis of optically correlated imagery produced wavelength and

direction measurements comparable to those from one-dimensional spectra generated by instrumentation at the CERC pier and an aircraft laser profilometer. The CERC pier instruments included two Baylor gauges, two wave rider buoys, and a capacitance wave staff.

In the sections which follow, emphasis will be placed on comparison of the SAR imaged wave field from Cape Hatteras (pass 974) to the predicted field from VSWCM wave ray diagrams. Also discussed are efforts to perform a similar comparison for Long Island, passes 974 and 1404.

The methods used during these comparisons have been developed from the viewpoint that satellites and wave climate models may eventually be combined in a system to predict shoreline wave climate. Verification of predicted wave refraction in this and other studies could lead to deployment of a network of satellites carrying microwave sensors. Data from such satellites would often be collected from offshore environments, and could thereupon be used to initiate wave climate models for prediction of the wave climate as the wave field progressed toward shallow water environments. As the satellites and models would be used over extensive areas, our approach here has been to utilize mapping methods appropriate to extension over large areas. In so doing, we have put more than the usual effort into methods, comparisons and error analyses encompassing the full range of wave data derived from the SAR.

In broad terms, the output of the VSWCM has been closely verified by the Seasat SAR data. In the Cape Hatteras area, some anomalies are found, which may be due to bathymetric irregularities or complex current fields. In the Long Island area, where SAR detection of the wave field was less uniform, VSWCM output is still verified to a reasonable degree. With respect to the possibility of a satellite/model system for predicting wave climate, careful consideration will have to be given to the data reduction component in order to minimize prediction errors due to multiple wave trains and uncertainty in the measured wave spectrum and its dominant features.

METHODS AND MATERIALS

I. Introduction

To measure length and direction of waves on SAR pass 974, Cape Hatteras, a method was devised whereby a subimage was enlarged and rotated until it matched a standard Ronchi ruling. This method was eventually chosen for principal use in data extraction, and most data shown in map form in this report were obtained using this method. However, two other methods were tested for data extraction, namely crest-counting and optical Fourier Transforms (OFTs). In the first, wavelength was measured by counting crests along an orthogonal on an enlarged subimage. In the second, wavelength and direction were measured on film copies of optical Fourier transforms produced with a laser apparatus. A comparison has been performed between the crest-counting, OFT, and Ronchi ruling methods.

In measuring length and direction of waves from SAR imagery, there are several problems. First, the ocean itself has complex spectral qualities, frustrating the choice of a dominant wavelength and direction. Regardless of method used, qualitative observation of OFTs shows that even for highly peaked spectra, the wavenumber spectrum is sufficiently broad and irregular to produce uncertainty in the neighborhood of ± 5 -10 per cent in wavelength and ± 2 degrees in propagation direction (Figure 1). Often, OFT spectra are less peaked, and uncertainties are correspondingly greater. Second, SAR imagery examined here was uncorrected for both slant range scale distortion and range walk. Investigation showed that slant range distortion did not significantly affect our results, and therefore no corrections were applied. Third, the SAR imagery used for zoom transfer scope measurements was a second generation image copied from the "master positive" produced by the Jet Propulsion Laboratory (JPL, Pasadena, California), and of lesser quality. Fourth, the optically correlated imagery examined here varied noticeably in contrast over the range dimension from the near to the far edge of the film. Finally, establishing boundaries of good wave visibility was difficult. Being able to identify and set aside areas whose waves are marginally visible or unmeasurable is an asset, as it saves time on fruitless attempts of data extraction.

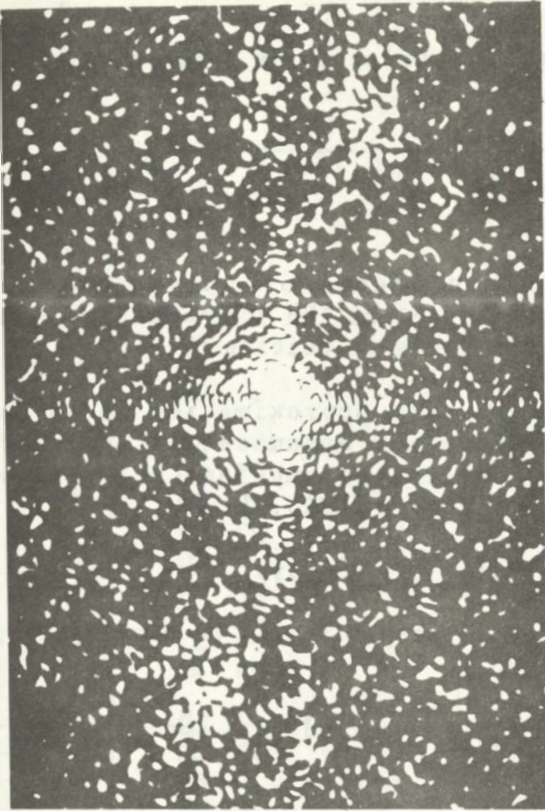
In the sections which follow, SAR imagery and its inherent geometrical distortions are discussed. Then measurement techniques and their precision are treated. Finally, an investigation of ideal spatial sampling density and field uniformity is presented.

II. The Virginian Sea Wave Climate Model

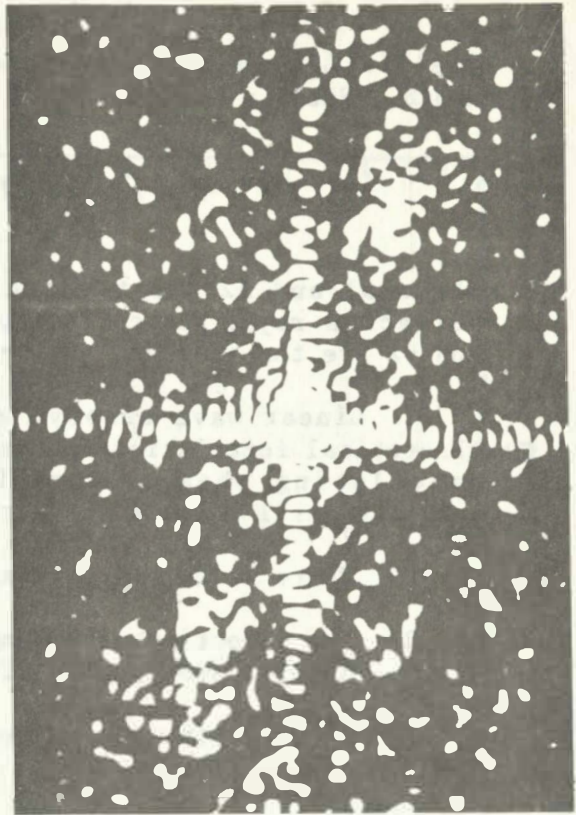
A. Wave Refraction Model

The wave refraction model used in the VSWCM is essentially the same as the program described by Dobson (1967), and is fully described by Goldsmith *et al.* (1974). Wave rays are refracted according to

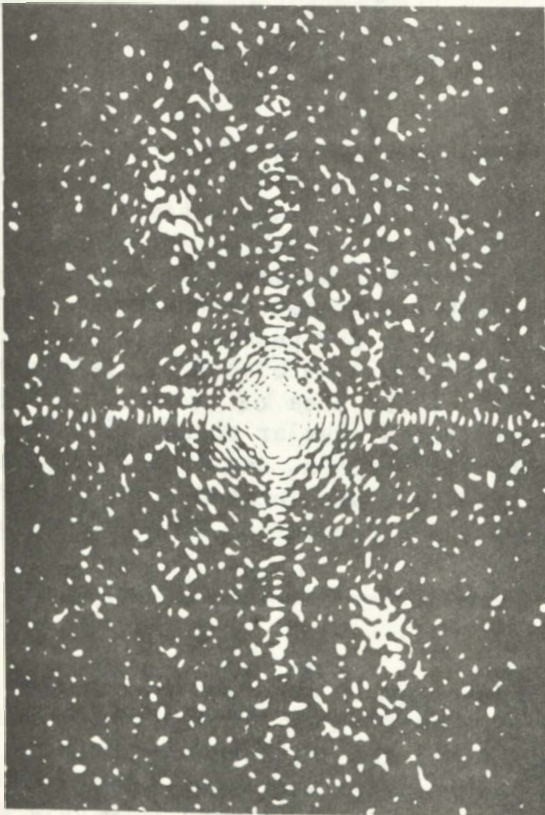
Figure 1. Typical Optical Fourier Transforms from pass 974, Cape Hatteras. Note breadth of spectral peaks. Enlarged from 35 mm film OFTs from SAR imagery of scale 1:500,000. Object plane apertures as shown.



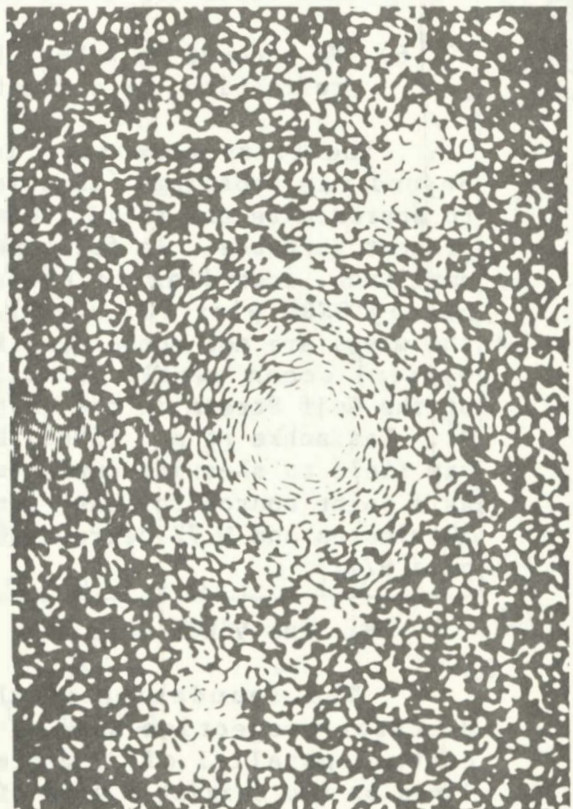
11 mm square



5 mm square



11 mm square



11 mm circle

Snell's Law in which the propagation velocity is a function of ocean depth. Snell's Law is

$$\sin a_1 / \sin a_2 = v_1 / v_2 , \quad (2)$$

where a_1 and a_2 are the angles of incidence of the incident and refracted rays, respectively, with respect to the local isobath, and v_1 and v_2 are the incident and refracted phase velocities.

Linear wave theory, a first order approximation to an exact theoretical formulation for wave propagation dynamics, is employed in calculating phase velocities. Several assumptions are made when applying Snell's Law with linear wave theory (CERC, 1977):

- 1) There is no energy transfer from ray to ray.
- 2) The direction of propagation is perpendicular to wave crests, i.e., there is no diffraction.
- 3) The celerity for a wave of a given period is a function of depth only.
- 4) The bathymetry is smooth; there are no abrupt changes in depth.
- 5) The waves are ideal monochromatic waves of low amplitude.
- 6) No account is taken of local winds, current-induced refraction, or reflection.

The first condition is met in this application except at and beyond ray crossings (caustics). At caustics, linear wave theory fails to approximate the field. Conditions 2, 3, and 4 are satisfied for the present purposes. As for condition 5, the waves are of sufficiently low amplitude, according to the one-dimensional spectra measured at the nearby CERC pier (Figure 2). The CERC measurements show that although the waves are not monochromatic, the spectra are peaked in the manner of typical ocean swell. Finally, condition 6 is violated by the presence of the Gulf Stream in the eastern part of the area of interest (Figure 3). Kasischke et al. (1981) have attributed angular changes in the wave ray field to shearing currents of the Gulf Stream, and to Hurricane Ella as a point source for wave generation. Ella was located at N 32 degrees 30 minutes and W 72 degrees 30 minutes on September 3, 1978, the date of pass 974.

B. The VSWCM Grid

The foundation of the VSWCM mapping domain is a transverse Mercator projection with a central meridian of 75 degrees W and a central parallel of 37 degrees N. Using the intersection of these two lines as the origin, a grid of two-inch squares was drawn. Next, lines of latitude and longitude were superimposed at 10-minute intervals at a

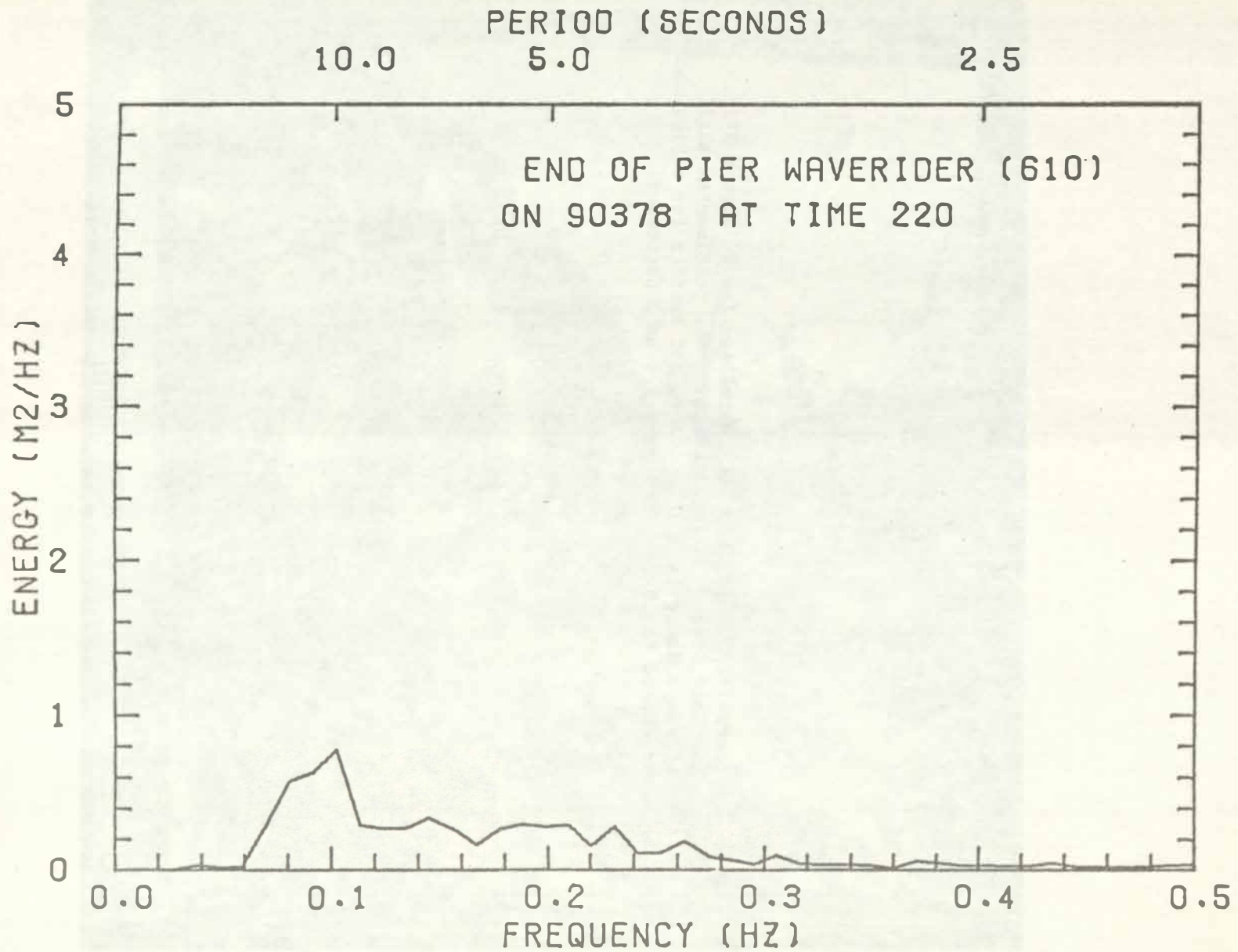
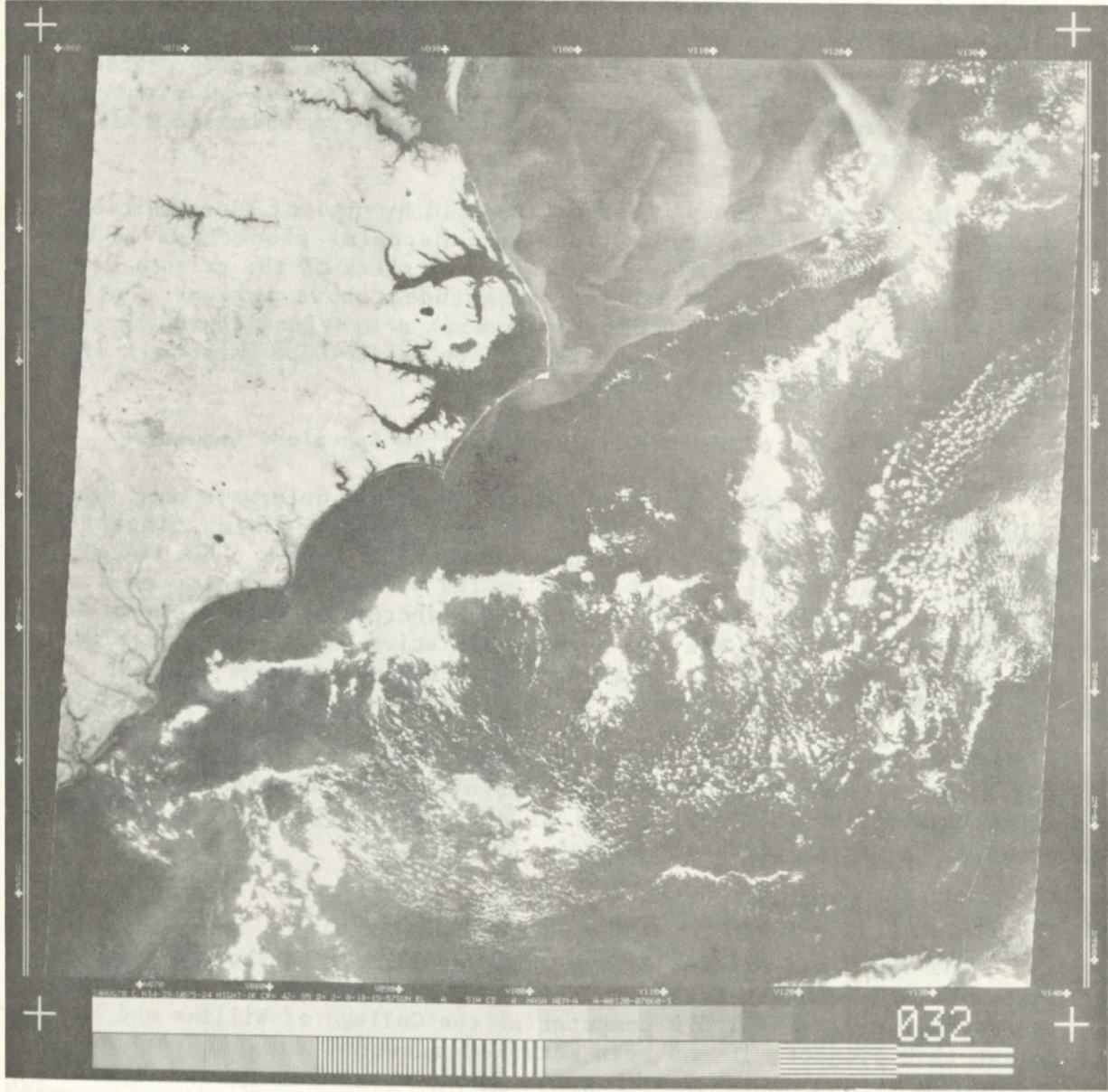


Figure 2. Wave spectrum at CERC pier concurrent with pass 974 (Lichy, pers. comm.).

Figure 3. Thermal IR image from HCCM satellite for 24 August 1978. The Gulf Stream is shown skirting the continental shelf off Cape Hatteras. This image, and another for 9 September, bracketed the Seasat SAR pass 974 on 3 September.

...the ... of
... ..
... ..

The
... ..
... ..
... ..
... ..



... ..
... ..
... ..

scale for the origin of 1:482,000. The x, y coordinates of the latitude/longitude intersections were calculated by a computer program (Goldsmith et al., 1974).

The Dobson program requires that bathymetry be entered as a two-dimensional array with elements corresponding to depths from a square grid pattern. For this study, the array of bathymetric depths previously assembled for the Virginian Sea (Goldsmith et al., 1974), was extended from just north of Cape Hatteras to 40 km south of Cape Hatteras. The additional data were assembled by interpolating depths from National Ocean Survey sounding sheets 8808 and 9104 (with dates of 1963 and 1970, respectively) onto a 0.5 nautical mile square grid extending from approximately 34 degrees 50 minutes N to 36 degrees 10 minutes N, and 75 degrees 50 minutes W to 74 degrees 50 minutes W. Figures 4 and 5 show bathymetric contour maps which include the additional data.

The shoreline was plotted on the grid by optical superposition of meridians and parallels from a transverse Mercator projection of Cape Hatteras (Manteo, 1:250,000). A subsequent check of the orientation of landforms, with respect to lines of longitude, shows agreement within one degree, according to comparison with a nautical chart (Mercator projection, 1:416,944 at 37 degrees N, Cape May to Cape Hatteras) via a Bausch and Lomb Zoom Transfer Scope.

C. Deviation of Great Circle Lines from Spherical Geometry

Lines of latitude and longitude at 10-minute intervals were mapped onto this square grid from a transverse Mercator projection tangent at the 75 degrees W meridian (Goldsmith et al., 1974). The deviation between a great circle and its image on the projection (a curved line) is maximum in the North-South orientation, increasing with distance from the central meridian. Maximum angular deviation is less than one degree for the portion of the map between Cape Henlopen and Cape Hatteras. At the Cape Hatteras area examined in this study, wave crests are oriented approximately west-northwest, with virtually all data extraction points falling within 30 minutes of the 75 degree W meridian. Therefore, wave ray maps produced for the Cape Hatteras area should have angular deviations well within one degree of corresponding diagrams produced using a spherical coordinate system.

D. Wave Ray Plotting

The VSWCM was originally developed in 1972-74 on the CDC computing system at NASA Langley Research Center. Subsequently, it was modified to run on the IBM model 370 computer at the College of William and Mary. During this project, it has been modified a second time to run on the Prime 750 computer at the Virginia Institute of Marine Science. A Tektronix plotter terminal model 4015-1 and a Houston Instruments Complot drum plotter (22-inch) are used for preliminary and final plotting of ray diagrams.



Figure 4. Bathymetry near Cape Hatteras. Contours in feet drawn manually with reference to original NOS data.

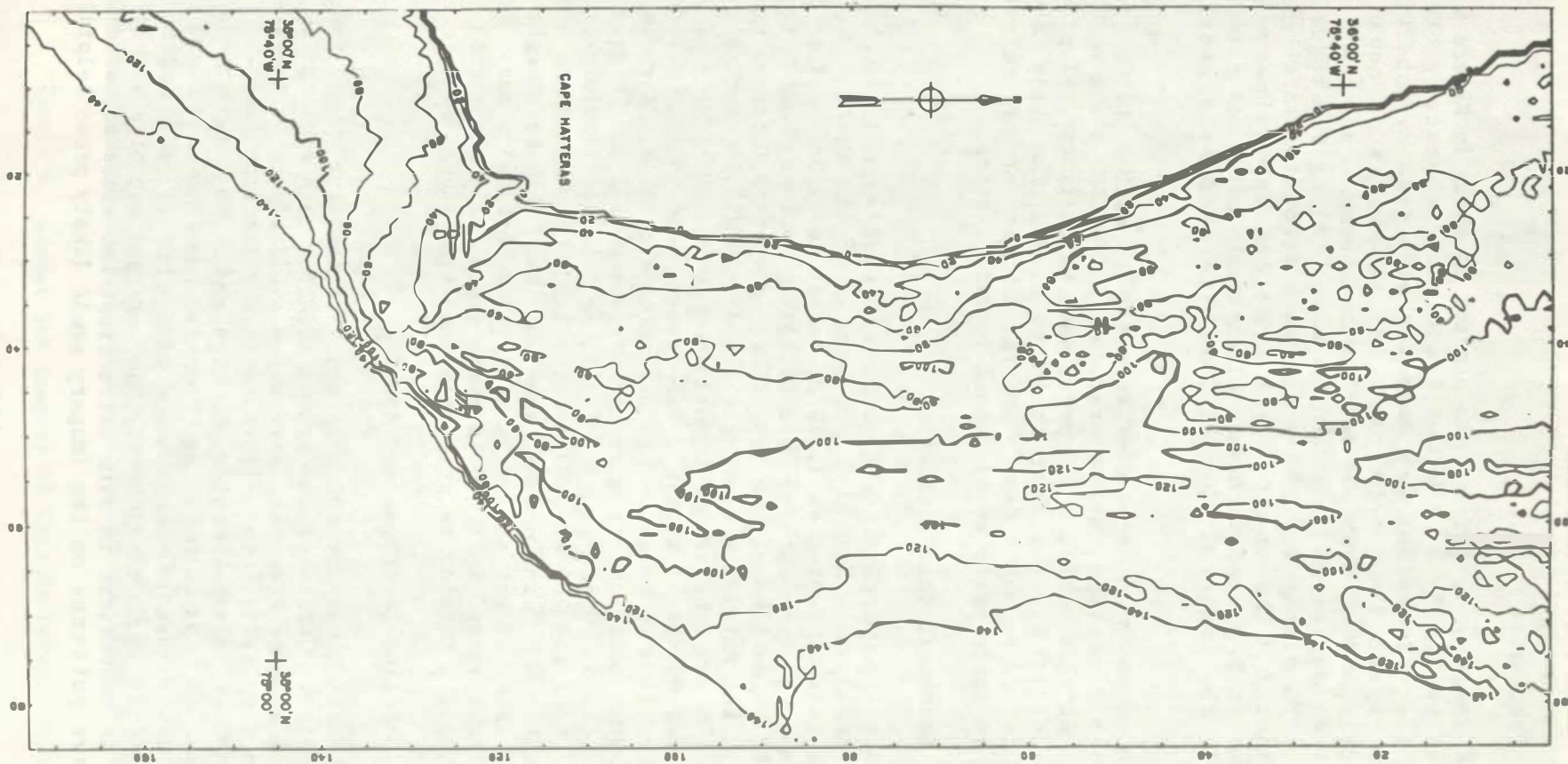


Figure 5. Computer-contoured bathymetry near Cape Hatteras. Contours in feet computer-drawn from VSWCM bathymetric grid data.

III. SAR Image Data Extraction

A. Processing

SAR imagery used for this project is shown in Figure 6. It was correlated optically by the Jet Propulsion Laboratory (Pasadena, California). Processing was done for each pass by subdividing the satellite swath into four parallel subswaths of equal width, approximately 30 km. When the overlapping subswaths are combined into a mosaic, they depict an area 100 km wide. Along the edges of each subswath, JPL placed tic marks for each second of satellite travel, spaced about 6.6 km apart. JPL provided approximate location coordinates at 30-second intervals along-track, but since a landform was present in the imagery, the landform was used as a geographical reference.

Each subswath was processed separately, with a uniform scale in the azimuth dimension, and a scale of 1:500,000 in the center of the subswath. At this scale, a 120-metre wave which is typical of waves in this project is 0.24 mm from crest to crest. The scale in the range dimension varied ± 4 per cent from far to near range, respectively. Variation in range scale is discussed in detail below.

B. Geometric Characteristics

During each orbit, all polar orbiting satellites describe an S-shaped curve on a Mercator projection of the earth. During the descending pass of September 3, 1978, Seasat described a slightly curved swath extending from south of Cape Hatteras northward to Nova Scotia. For the 200 km portion of the pass centered on Cape Hatteras examined in this study, the satellite bearing changed from 205.65 degrees to 205.11 degrees. During the image-formation process, the arc-shaped ground swath was mapped onto a straight line image, and ultimately data were transferred to the Mercator projection of the VSWCM. A rough estimate of the maximum location error in this process is 2 km (Figure 7) (see Carpenter, in Goldsmith *et al.*, 1974), or 1 km for landform-matching at the midpoint of the 200 km. Neglecting both the curvature errors and slant range scale distortion, the SAR image can be thought of as an oblique cylindrical projection tangent at the orbital plane. Because of the small area imaged in a 100 km swath width, this projection is nearly conformal, *i.e.*, angular relationships and true shapes are preserved.

C. Sampling Locations and Areas

When making measurements, appropriate sampling areas (subimages) must be chosen. Choice of an optimum size for each subimage is a trade-off between a large area with more waves available to be averaged, and a small area displaying more uniformity in a refracting field. From these considerations, 5 mm diameter circles and 5 mm length squares were chosen as an optimum size for routine measurements. Some intercalibration measurements were done with 11 mm circles to match subimage areas used elsewhere. The routine use of a single size for subimages is convenient in data extraction, but sizes adjusted according to the wave patterns on the imagery would likely prove helpful. Faint

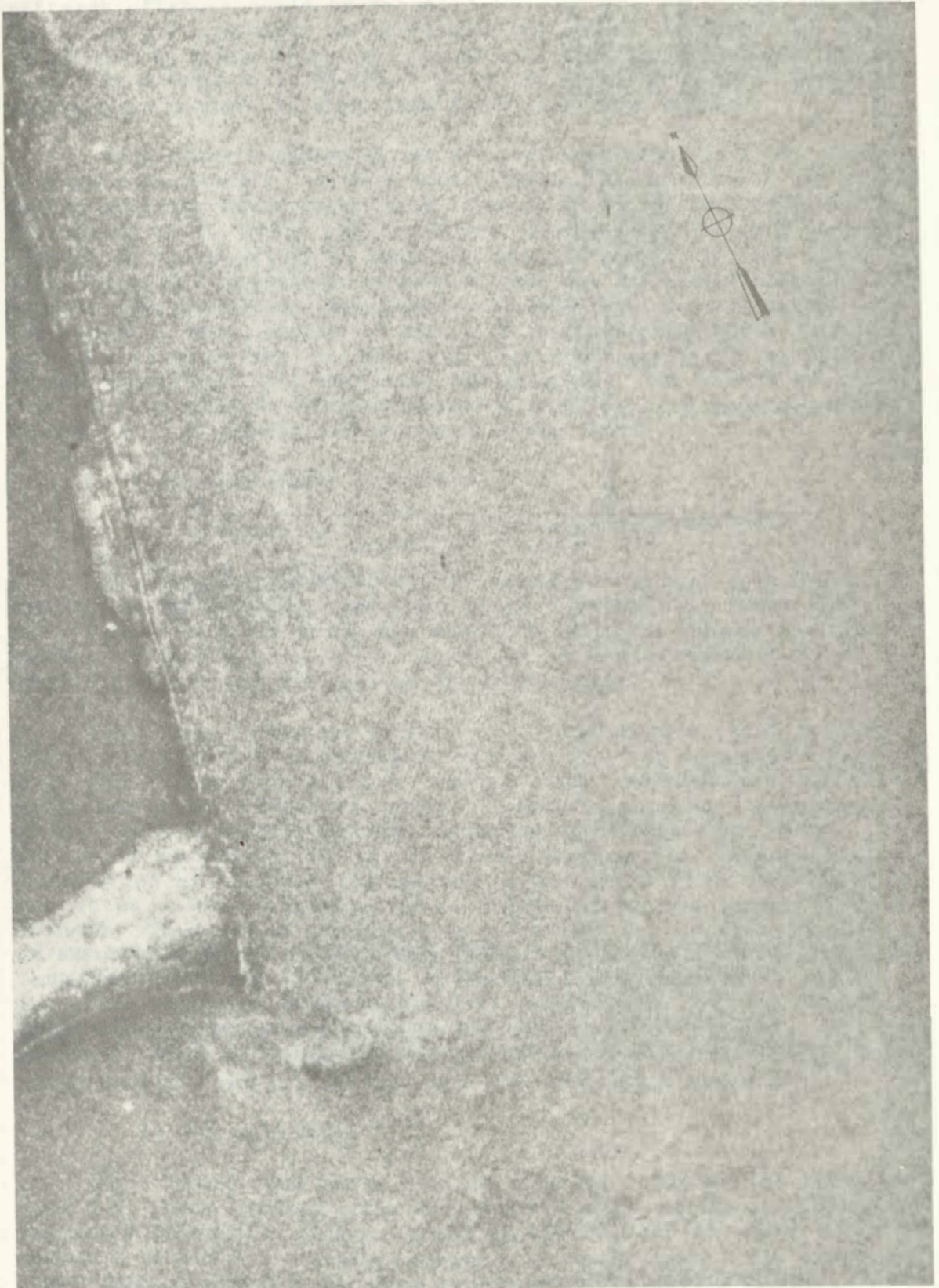


Figure 6. Seasat SAR imagery of Cape Hatteras. Enlargement.

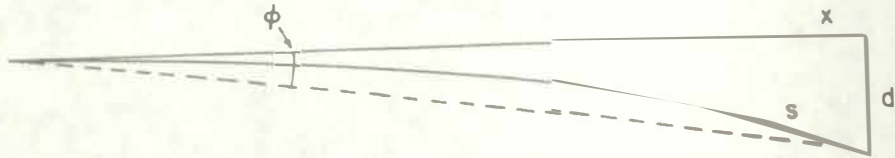


Figure 7. Estimate of location error from mapping the SAR ground swath onto the Mercator projection. Symbols: s--curved track on Mercator projection. x--track according to image. d--displacement. Phi--change in clock angle perpendicular along 200 km. $\text{Phi} = 0.6 \text{ degree}$, $d = 200 * \sin(\text{phi}) = 2 \text{ km}$.

patterns offshore could be enhanced by the use of larger sizes. Nearshore patterns where the wavelength has become shortened also would be enhanced by larger sizes, but the details of refraction would then be lost. At a scale of 1:500,000, 5 mm on the image corresponds to 2.5 km on the ocean surface, or about twenty 120 metre wave crests.

To designate subimages, an array of tangent circles was plotted on transparent acetate. In deep water, where the wave field was most nearly uniform, measurements were taken at 12 km spacing, while on the continental shelf, where the depth was intermediate or shallow with respect to the wavelength, sampling was at every 7 km (see sampling grid, Figure 8). A constant density of sampling was deemed necessary to produce data permitting interpolation of wave rays, for comparison with VSWCM output. Also, economy of effort in data reduction would require a protocol using arrays in the event that construction of ray diagrams becomes operational in a satellite SAR program. The use of an array here was intended to uncover possible problems and considerations relevant to planning for such a system in the future.

D. Slant Range Scale Distortion

1. Introduction

The imagery produced by JPL using an optical correlator is uncorrected for range walk and slant range distortion. Range walk is due to earth rotation during the satellite overpass, causing the ground swath to curve slightly. Such distortion is small compared to slant range distortion, and will not be discussed further.

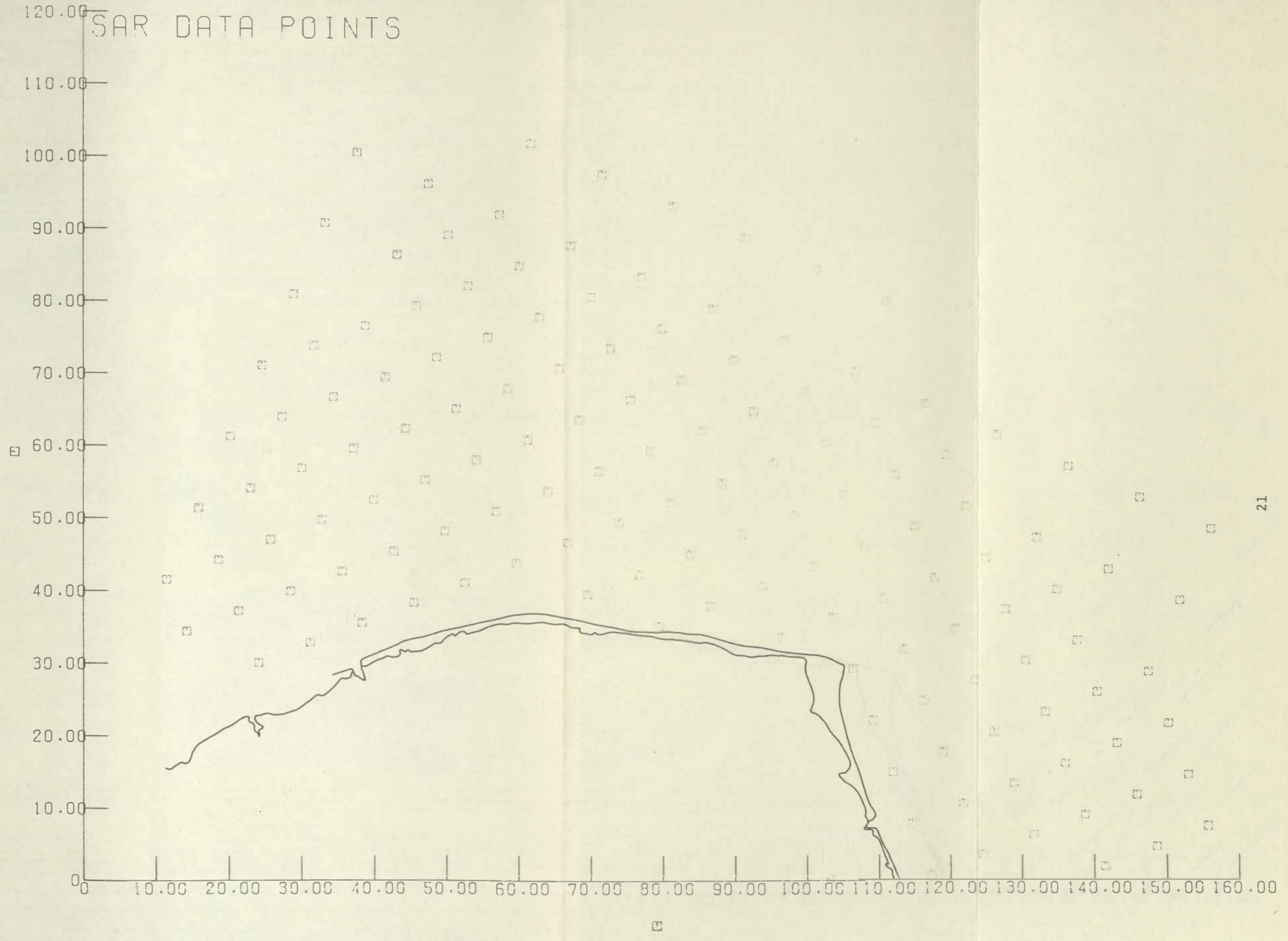
Slant range distortion exists in all uncorrected radar imagery, and is manifested by a systematic increase in scale rangeward from the near edge of the ground swath. Range scale inhomogeneity affects measurements of 1) ground range; 2) wave propagation direction; and 3) wavelength in varying amounts, depending on distance from nadir. JPL partially corrected for slant range distortion during optical correlation by dividing the ground swath into four overlapping subswaths, with scale adjusted to 1:500,000 at the center of each subswath. This partial correction is sufficient for present purposes, as shown by analysis which follows below. Measurements at all subimage locations were therefore made as if the scale were uniformly 1:500,000. The error in ground range under this presumption will be discussed first. Next, effects on wavelength and direction measurements will be examined. Lastly, image distortion is examined quantitatively, both within a single sampling subimage and over the entire subswath.

2. Error in Range

Variation of range scale over the width of a subswath is shown in Figure 9. Here, inverse scale is plotted at each centimetre across the subswath. Subswath 1, closest to the satellite, has the most extreme variation in scale; conversely, subswath 4 has the least. The errors in range location, which result from an assumption of uniform scale, were determined in a straightforward fashion (for detail, see Appendix 1). First, ground range from the nadir was calculated using equation (7) of

Figure 8. Sampling grid of data extraction points for pass 974, Cape Hatteras.

SAR DATA POINTS



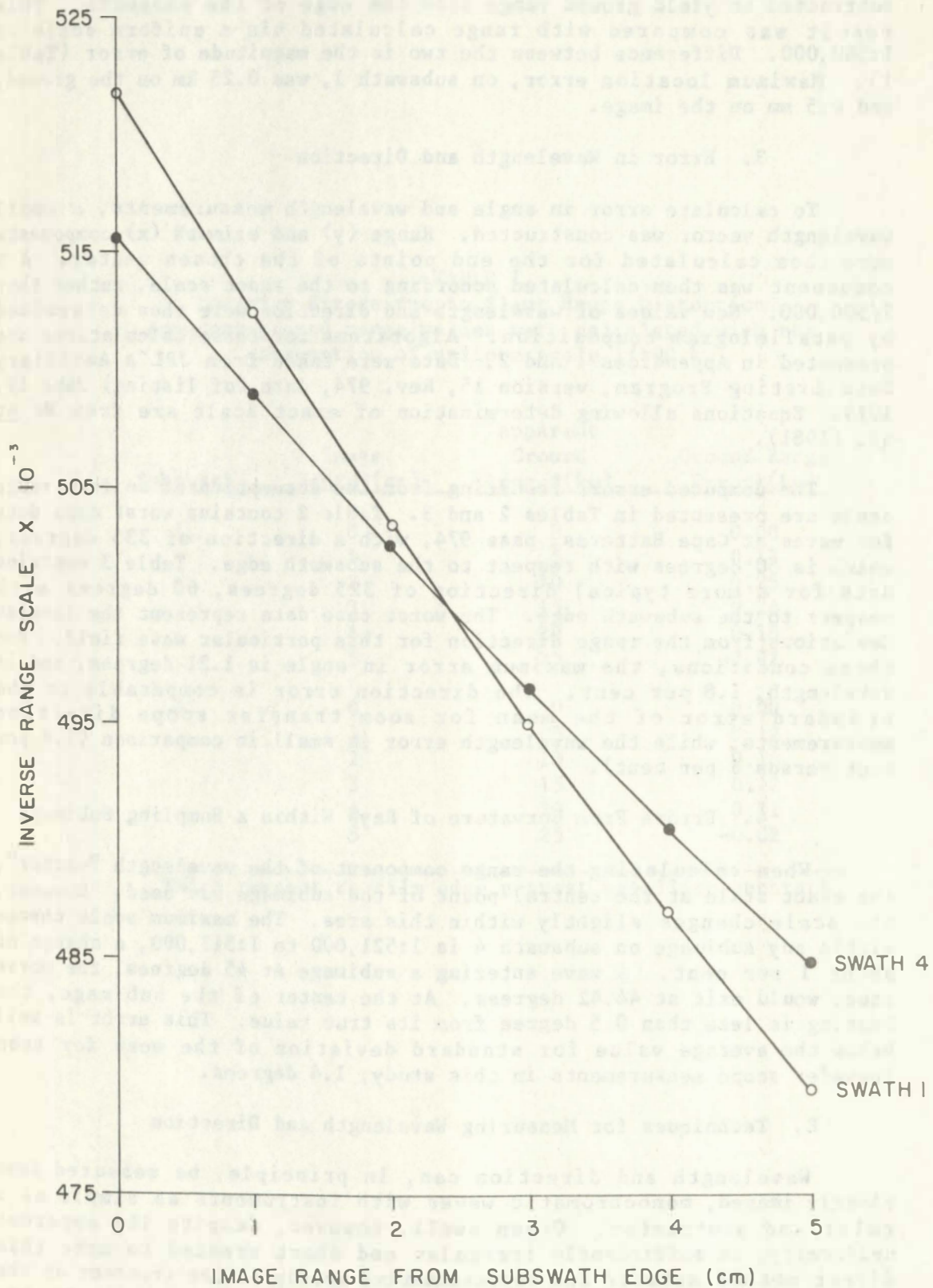


Figure 9. Variation of inverse range scale factor for SAR subswaths (optically correlated imagery).

Wu et al. (1981). Then ground range from the subswath edge was subtracted to yield ground range from the edge of the subswath. This result was compared with range calculated via a uniform scale of 1:500,000. Difference between the two is the magnitude of error (Table 1). Maximum location error, on subswath 1, was 0.25 km on the ground, and 0.5 mm on the image.

3. Error in Wavelength and Direction

To calculate error in angle and wavelength measurements, a small wavelength vector was constructed. Range (y) and azimuth (x) components were then calculated for the end points of the chosen vector. A y component was then calculated according to the exact scale, rather than 1/500,000. New values of wavelength and direction were then determined by parallelogram composition. Algorithms for these calculations are presented in Appendices 1 and 2. Data were taken from JPL's Auxiliary Data Listing Program, version 15, Rev. 974, date (of listing) June 19, 1979. Equations allowing determination of exact scale are from Wu et al. (1981).

The computed errors resulting from the assumption of uniform range scale are presented in Tables 2 and 3. Table 2 contains worst case data for waves at Cape Hatteras, pass 974, with a direction of 335 degrees, which is 50 degrees with respect to the subswath edge. Table 3 contains data for a more typical direction of 325 degrees, 60 degrees with respect to the subswath edge. The worst case data represent the largest deviations from the range direction for this particular wave field. For these conditions, the maximum error in angle is 1.21 degrees, and in wavelength, 1.8 per cent. The direction error is comparable to the standard error of the mean for zoom transfer scope direction measurements, while the wavelength error is small in comparison (1.8 per cent versus 6 per cent).

4. Errors From Curvature of Rays Within a Sampling Subimage

When calculating the range component of the wavelength "vector", the exact scale at the central point of the subimage was used. However, the scale changes slightly within this area. The maximum scale change within any subimage on subswath 4 is 1:521,000 to 1:517,000, a change of about 1 per cent. A wave entering a subimage at 45 degrees, the worst case, would exit at 44.42 degrees. At the center of the subimage, the bearing is less than 0.5 degree from its true value. This error is well below the average value for standard deviation of the mean for zoom transfer scope measurements in this study, 1.4 degrees.

E. Techniques for Measuring Wavelength and Direction

Wavelength and direction can, in principle, be measured from clearly imaged, monochromatic waves with instruments as simple as a ruler and protractor. Ocean swell, however, despite its apparent uniformity, is sufficiently irregular and short crested to make this direct method awkward and representative merely of the transect at the ruler's edge. To better describe the two-dimensional wave field, measurement over a unit area is preferable. A well-known method which

TABLE 1

Location Errors due to Slant Range Distortion.
 Apparent ground range values were calculated with the
 assumption of uniform scale 1/500 k.

Subswath	Image Range*(cm)	Apparent Ground Range*(km)	Ground Range Error*(km)
1	0	0	0.00
	1	5	0.17
	2	10	0.25
	3	15	0.24
	4	20	0.15
	5	25	-0.02
4	0	0	0.00
	1	5	0.12
	2	10	0.18
	3	15	0.17
	4	20	0.11
	5	25	-0.02

*With respect to film edge nearest satellite subtrack.

TABLE 2
 Worst Case Errors in Wavelength and Direction Attributable
 to Slant Range Distortion. Rev 974, Cape Hatteras. Wave ray
 direction = 335° (50° with respect to azimuth).

Subswath	Ground Range*(km)	Error	
		Direction (degrees)	Wavelength (percent)
1	0	-1.21	1.8
	1	-0.69	1.1
	2	-0.19	0.3
	3	0.29	0.5
	4	0.76	1.2
	5	1.20	1.8
4	0	-0.87	1.3
	1	-0.50	0.8
	2	-0.14	0.2
	3	0.21	0.3
	4	0.55	0.8
	5	0.87	1.3

*With respect to film edge.

TABLE 3
Typical Errors in Wavelength and Direction Attributable
to Slant Range Distortion. Rev 974, Cape Hatteras. Wave ray
direction = 325° (60° with respect to azimuth).

Subswath	Ground Range*(km)	Error	
		Direction (degrees)	Wavelength (percent)
1	0	-1.07	1.1
	1	-0.62	0.7
	2	-0.17	0.2
	3	0.26	0.3
	4	0.68	0.7
	5	1.06	1.1
4	0	-0.76	0.8
	1	-0.44	0.5
	2	-0.12	0.1
	3	0.19	0.2
	4	0.49	0.5
	5	0.77	0.8

*With respect to film edge.

employs a unit area is the optical Fourier transform, which produces a two-dimensional wavenumber spectrum. A third method has been developed during this project, and is based on comparison of wave imagery to Ronchi rulings using variable magnification optics. All three methods are described below.

1. Crest Counting Along An Orthogonal

For a small set of subimages, wavelength was measured by counting crests along orthogonal lines drawn onto a projection enlargement of the SAR image. Using a Recordak microfiche reader, the image was magnified by a factor of 18. Where a prominent wave train appeared, a straight line orthogonal to the crests was drawn onto the screen with a felt tipped pen. Crests were marked along the line, the number of crests recorded, and the line measured. From one to three lines were drawn and measured for each subimage by different observers. Difficulties were encountered in identifying crests, particularly in marginal areas where crests gradually became unresolvable. In many instances, there were fine striations which appeared to be crests, but which were ignored, because the number of crests was small and no regular pattern of striations could be discerned over a large enough area. A brief quantitative comparison was made between crest-counting and the other wavelength-measurement methods, and it showed that crest-counting produces relatively irregular results. Because of these drawbacks and a preference for an areal measurement, crest-counting was discarded in favor of the OFT method and the zoom transfer scope method.

2. Optical Fourier Transform (OFT) Method

An interesting attribute of two-dimensional wave imagery is that a directional wavenumber spectrum can be produced using rather simple optical apparatus (Egbert et al., 1974). For this study, the beam from a 0.5 milliwatt He-Ne laser was diverged by a 10X microscope ocular, projected through the object transparency (SAR subimage), then converged onto photographic film (Figure 10). The diffraction pattern formed is a spatial, two-dimensional Fourier transform, termed an optical Fourier Transform (OFT). It is widely accepted as a spectral analysis method for images of ocean waves (Barber, 1949, Stilwell, 1969, Kasevitch et al., 1971, Shuchman et al., 1979, Gonzales et al., 1979, Beal, 1980, and Kasischke et al., 1981). Separation of first order maxima is inversely proportional to wavelength; azimuthal orientation defines the wave propagation direction (except for a 180 degree ambiguity). A square transform aperture may be used in order to produce a diffraction pattern with a cross-shaped artifact in the center; the cross provides a convenient frame of reference from which to measure direction, Figure 1.

Some 200 OFTs were imaged at VIMS during this project. In some cases, to minimize error during identification of spectral peaks, the peaks were located using an International Imaging Systems (I2S) 5-bit density analyzer with color-coded television display, and read for azimuth and peak spacing under enlargement using the Zoom Transfer Scope (ZTS). Direction of propagation was measured on the ZTS by projection of an enlarged image onto an azimuthal grid. Separation of diametrically-opposed spectral peaks was measured on the optical

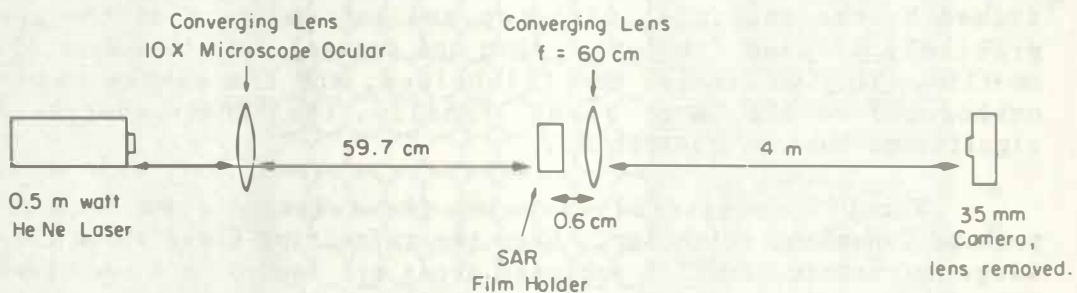


Figure 10. Optical diagram for OFT production. Film: Kodak Tri-X panchromatic. Typical exposure: 1/16 sec.

enlargement with a millimetre rule. To convert separation into wavenumber, transforms were made from glass Ronchi rulings (Edmund Scientific) of spacing 50, 80, 100, and 133 lines per inch, used as calibration standards.

The OFT method reveals spectral features, bringing some order to the confusion of a complex wave image. The method is advantageous in that it reveals the range in wavelength and direction present in a SAR subimage.

One disadvantage of the OFT method is that it involves the use of still another photographic step (the OFT image) for the measurements (this would not be the case if an image tube were used for read-out of spectral details, or if digital Fourier transforms were computed from tape data; see Egbert *et al.*, 1974 and Shuchman *et al.*, 1979). Errors during imaging must be minimized by means of several precautions. Film must be carefully placed into the filmholder so that the desired area is framed by the aperture, with top and bottom edges of the aperture precisely aligned (to better than one degree) with the edges of the 70 mm film. The two lenses, the filmholder, and the camera must all be orthogonal to the laser beam. Finally, the lenses must be free of significant optical aberration.

The OFT necessarily samples the selected area with uniform, perhaps Gaussian, weighting. When the refracting field shows relatively large curvature, smaller subimage areas are needed, and measurements on OFTs from the nominal-size subimage will smooth the spatial detail.

A source of error in the OFT method is that a point corresponding to the spectral peak must be identified for data extraction. Identification is simple for highly peaked spectra, but not for those which are diffuse and/or have peaks offset from the energy-averaged center of gravity. There were many cases where the tallest of multiple peaks in a localized pattern on the OFT could not be distinguished, or conversely, where the summit was sufficiently flat that a central point had to be arbitrarily chosen. The resulting uncertainty in location varied with the spectrum, but for flat elongated patterns was on the order of ± 10 percent of measured radius. Because patterns were elongated primarily in the radial direction, there was much less uncertainty introduced in the azimuth (wave direction) readings. Consequently, there were differences in uncertainty for wavelength and direction measurements, as reflected in the intercalibration results discussed below, where wavelength measurements are less precise and less accurate than direction measurements.

We note that others such as Beal (1980, 1981) have apparently encountered such problems in OFT data, because considerable smoothing has been employed before comparing Fourier transform data from different locations.

3. Zoom Transfer Scope (ZTS) Method

A simple method of measuring the wavenumber vector was devised involving the optical superposition of Ronchi rulings on wave images.

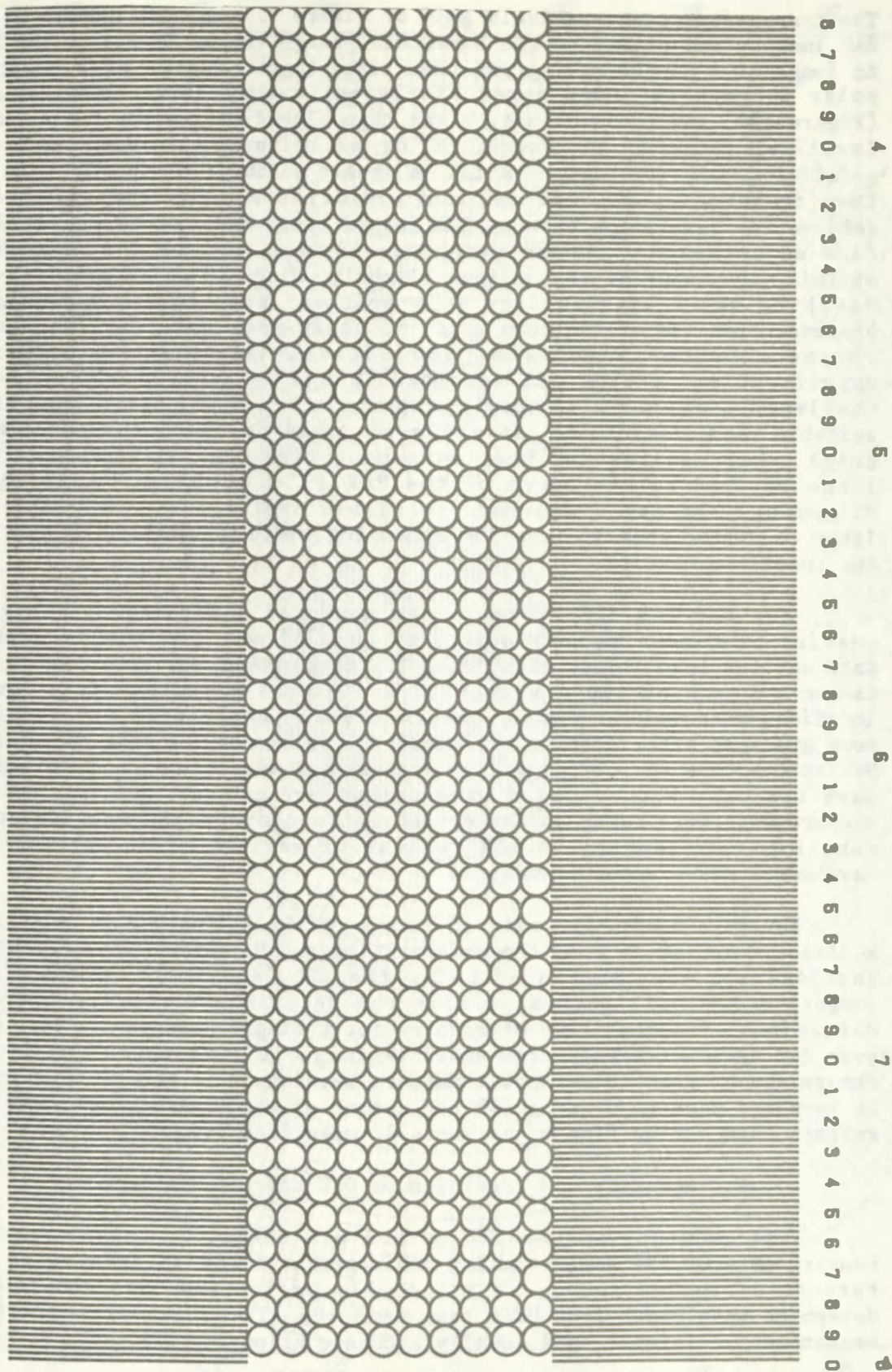


Figure 11. SAR film overlay with matrix of tangent circles. Rows of rulings on near and far edges of film were used to determine angle of wave propagation.

The transparent tangent-circle grid of Figure 11 was superimposed on the SAR imagery and placed on the horizontal stage (upper level) of the ZTS. An image of a Ronchi ruling was then fixed to the center of a sheet of polar coordinate graph paper displaying a one-degree azimuthal grid (Figure 12), and the combination was then placed on the map table (lower level) of the ZTS. The Ronchi ruling was oriented such that lines were parallel to the zero-degree axis. A masked subimage of the SAR film was then centered in the optics, and optically rotated and enlarged to achieve the best match between SAR imaged waves and the Ronchi ruling. Fine adjustments in phase were made in both horizontal dimensions by shifting the image of the rulings slightly using ZTS adjustment screws. Matching waves with rulings is a critical step in the measurement process. Because of the complexity of ocean wave patterns, obtaining correspondence is somewhat subjective. At this step, the zoom magnification setting was recorded, and subsequently converted to wavelength, as it is inversely proportional to wavelength. Next, after suitable zoom adjustments, an angle was read on the polar coordinate graph paper manifesting best agreement with the pattern of parallel lines affixed to the edges of the SAR film overlay. After best alignment, the angle was read to within one degree. This angle was later converted to ray direction by adding the appropriate offset for the satellite heading.

For the 140 ZTS image points measured according to the grid overlay of Figure 8, and roughly another 150 made for intercalibration data and the Long Island grid, each ZTS measurement was made four times, twice by each of two observers. Additional measurements at other locations were made as single observations. Repetitive observations were averaged after editing of occasional values having wide deviations. Deviations were due to subjective measurement variations, and to crossed wave trains. When crossed wave trains were noticed, multiple sets of measurements were taken as appropriate. To convert ZTS magnification data into wavelength, Ronchi rulings of various sizes were used as wavelength measurement standards.

For this study, the main advantage of the ZTS method is that it is a direct measurement from the original image. Direction measurement is particularly easy and rapid using the ZTS, and small regions of the imagery a few millimetres in size can be examined readily for wave direction. Repeatability of results for a single observer is very good even for data extraction from small regions. Direction can easily be determined by the ZTS method. However, wavelength is more difficult, as it requires care to distinguish the amount of matching between waves and rulings when making fine adjustments in magnification.

4. Accuracy and Precision of OFT and ZTS Measurements

The accuracy of the ZTS method was tested by comparison with measurements of the same sampling subimages with OFTs. Because of the reasons discussed above, it is usually easier and more accurate to determine wavelength from OFTs than from the ZTS. However, direction measurement is simple, and equally accurate using the ZTS.

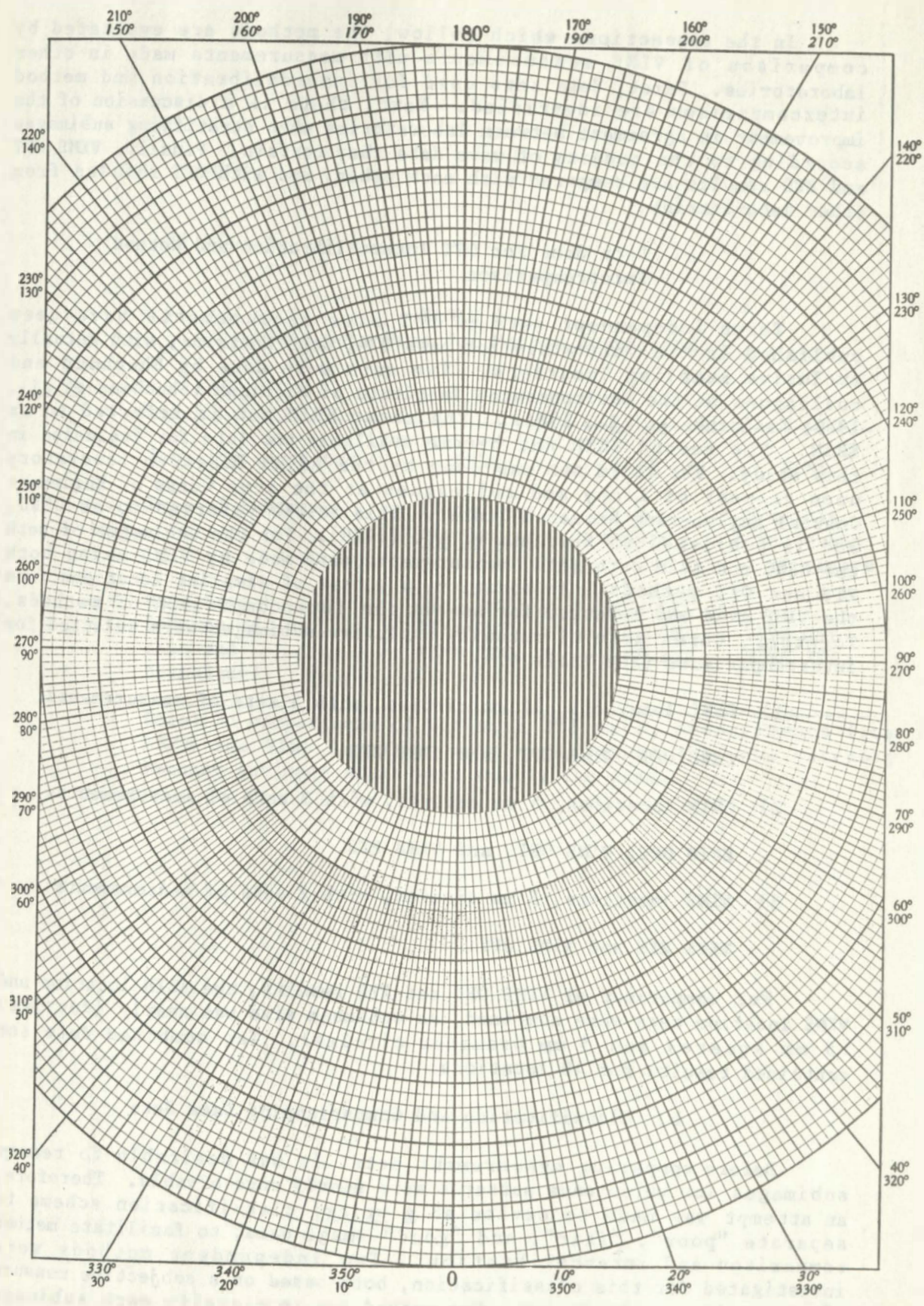


Figure 12. Azimuthal grid with Ronchi ruling pattern aligned with 360 degrees. This grid was placed on the ZTS map table for direction measurement.

In the subsections which follow, the methods are evaluated by comparison of VIMS measurements with measurements made in other laboratories. First, data sets used for intercalibration and method intercomparison are identified. Next, there is a discussion of the improvement in agreement between laboratories when stratifying subimages according to the quality of wave data they contain. Finally, VIMS OFT and ZTS results are compared with each other, and with OFT results from other laboratories.

a. Data Sets For OFT Intercalibration and Method Intercomparison

Three independent sets of OFT wave measurements have been published in the literature for pass 974, Cape Hatteras, with mutually exclusive sampling locations. Two sets were done by Shuchman and colleagues at the Environmental Institute of Michigan (Shuchman *et al.*, 1979; Kasischke *et al.*, 1981). The first ERIM set is referred to as ERIM. The second ERIM set became available too late for inclusion in this study. The third set was done by the Naval Research Laboratory upon request of Lichy and colleagues at the Army Corps of Engineers Coastal Engineering Research Center. This set is referred to as CERC, and is published in Shuchman *et al.* (1979). For the subimages of both the CERC and ERIM data sets, measurements were made by VIMS using both ZTS and OFT methods. In addition, a subset of sampling locations from the VIMS grid was selected for use in the intercomparison of methods. Together, three sets of mutually exclusive subimages were selected for intercomparisons (see Table 4):

- 1) CERC locations, 11 mm circles, with 3 sets of measurements:
CERC OFT, VIMS OFT, and VIMS ZTS.
- 2) ERIM locations, 5 mm squares, with 3 sets of measurements:
ERIM OFT, VIMS OFT, and VIMS ZTS.
- 3) VIMS locations, 5 mm circles, with 2 sets of measurements:
VIMS ZTS and VIMS OFT.

For comparison of VIMS OFT and ZTS results, the ERIM location and VIMS location sets were combined, as subimage size was nearly identical (5 mm squares and 5 mm diameter circles). The combined data set contained results for 48 locations.

b. Classification and Comparison of Data Sets

Before comparing measurement sets, it was desirable to remove subimages for which wave patterns were nearly unresolvable. Therefore, an attempt was made to devise an *a priori* classification scheme to separate "poor", "fair", and "good" image data, to facilitate method comparison and intercalibration. Two independent methods were investigated for this classification, both based on a subjective measure of expected wave resolution. One method was to classify each subimage

TABLE 4
Data Sets Used for Method Comparisons.

Sampling Locations	CERC	ERIM	VIMS
Type of Subimage	11 mm dia. circle	5 mm square	5 mm dia. circle and 5 mm square
Data Sets (source of data and technique)	CERC OFT VIMS OFT VIMS ZTS	ERIM OFT VIMS OFT VIMS ZTS	VIMS OFT VIMS ZTS

Note: In comparisons of OFT with ZTS data, measurements from ERIM and VIMS location sets were lumped into one category because subimage areas were nearly the same.

according to standard deviation of the mean (Sd) of the four replicate ZTS direction measurements. This method was based on the presumption that Sd should increase as clarity decreases. Another method was visual inspection of OFTs and their subjective classification as good, fair, or poor in terms of narrowness and contrast of spectral peaks. For either classification scheme to be useful, the correlation coefficient obtained when comparing data obtained by the different methods should improve with wave clarity.

Stratification by Sd for ZTS replicate measurements showed little correlation between clarity class and correlation coefficient for comparing results of OFT and ZTS methods, as can be seen in Table 5. The r values for direction data are very low due to four deviant points which fall outside the normal ranges of values (as determined from histograms). These points were from "poor" spectra (as evaluated visually), and their removal caused the r values to increase substantially. The results suggest that noise in the ZTS measurements was not strongly dependent on wave clarity, except for "poor" spectra. The Sd classification scheme was not pursued further.

In the test of classification by OFT quality, the largest set of observations, 48 VIMS + ERIM locations, showed a positive correlation between r value and clarity class, as shown in Table 6 comparing OFT and ZTS methods. A similar trend was observed for the ERIM set. A different trend was observed, however, for the CERC set (not shown), where the class "fair" had the highest correlation coefficients. It should be noted that both the CERC and ERIM sets were small in comparison to the VIMS + ERIM set, and each had only 2 to 6 observations in the "poor" class.

Since the 3-tier OFT classification scheme produced nonuniform trends, the top 2 tiers were combined and the comparisons repeated. In this arrangement, both the ERIM and VIMS + ERIM location sets had higher correlation of r value and image clarity class (Table 7). The CERC location set produced less distinct trends. However, because nearly all the data were stratified successfully, this 2-tier stratification scheme was implemented for intercomparisons that follow, in that data from "poor" OFT spectra were set aside and not included in the intercomparisons.

The finding that spectral quality impacts methods comparisons is to be expected and has significance beyond this study. With respect to a potential satellite/model system for prediction of shoreline wave climate, the data reduction algorithm will have to be designed to discriminate against poor spectra. This can be accomplished by means of the signal to noise ratio over the two dimensions of the OFT or digitally calculated spectrum.

c. Intercalibration of OFT Measurements

Although there were two sets of OFT measurements (ERIM and CERC) from outside laboratories available for intercalibration, there was no set having subimages measured by both CERC and ERIM. Consequently, there is no way to determine the amount of agreement between the

TABLE 5

Correlation between OFT and ZTS Results for Partitioned Data Sets.
 Partition method: standard deviation of the mean for four replicate
 ZTS measurements of direction.

a. VIMS + ERIM Subimage Locations. 48 Samples.

Variable	Quality	Correlation Coefficient	# Samples
Direction			
VIMS OFT	vs. VIMS ZTS		
	good	0.13	19
	fair	0.00*	20
	poor	0.80	9
	good+fair	-0.03	39
Wavelength			
VIMS OFT	vs. VIMS ZTS		
	good	0.75	19
	fair	0.65	20
	poor	0.91	9
	good+fair	0.68	39

*Removal of four points with visually poor OFTs
 yields $r = 0.90$.

b. CERC Subimage Locations. 31 Samples.

Variable	Quality	Correlation Coefficient	# Samples
Direction			
VIMS OFT	vs. CERC OFT		
	good	0.92	8
	fair	0.49	11
	poor	0.87	12
VIMS OFT	vs. VIMS ZTS		
	good	0.92	8
	fair	0.57	11
	poor	0.95	12
CERC OFT	vs. VIMS ZTS		
	good	0.95	8
	fair	0.90	11
	poor	0.87	12

Wavelength			
VIMS OFT	<u>vs.</u>	CERC OFT	
		good	0.95 8
		fair	0.22 11
		poor	0.76 12
VIMS OFT	<u>vs.</u>	VIMS ZTS	
		good	0.48 8
		fair	0.83 11
		poor	0.76 12
CERC OFT	<u>vs.</u>	VIMS ZTS	
		good	0.53 8
		fair	0.32 11
		poor	0.66 12

c. ERIM Subimage Locations. 18 Samples.

Variable	Quality	Correlation Coefficient	# Samples
Direction			
VIMS OFT	<u>vs.</u>	ERIM OFT	
		good	0.71 8
		fair	0.74 6
		poor	-- 2
VIMS OFT	<u>vs.</u>	VIMS ZTS	
		good	0.88 7
		fair	0.94 6
		poor	- 2
ERIM OFT	<u>vs.</u>	VIMS ZTS	
		good	0.86 8
		fair	-0.04 7
		poor	0.85 3
Wavelength			
VIMS OFT	<u>vs.</u>	ERIM OFT	
		good	0.72 8
		fair	0.33 5
		poor	-- 2
VIMS OFT	<u>vs.</u>	VIMS ZTS	
		good	0.75 7
		fair	0.88 6
		poor	- 2
ERIM OFT	<u>vs.</u>	VIMS ZTS	
		good	0.72 8
		fair	0.03 6
		poor	0.88 3

TABLE 6

Correlation Between OFT and ZTS Results for Partitioned Data Sets.
 Partition Method: Qualitative Evaluation of OFT Signal Clarity.

a. VIMS + ERIM Subimage Locations. 48 Samples.

Variable	Quality	Correlation Coefficient	# Samples
Direction			
VIMS OFT	<u>vs.</u> VIMS ZTS		
	good	0.94	21
	fair	0.68	13
	poor	-0.32	14
	good+fair	0.80	34
Wavelength			
VIMS OFT	<u>vs.</u> VIMS ZTS		
	good	0.88	21
	fair	0.71	13
	poor	0.12	14
	good+fair	0.79	34

b. CERC Subimage Locations. 31 Samples.

Variable	Quality	Correlation Coefficient	# Samples
Direction			
VIMS OFT	<u>vs.</u> CERC OFT		
	good	0.60	11
	fair	0.91	15
	poor	0.68	5
VIMS OFT	<u>vs.</u> VIMS ZTS		
	good	0.84	11
	fair	0.96	15
	poor	0.63	5
CERC OFT	<u>vs.</u> VIMS ZTS		
	good	0.78	11
	fair	0.91	15
	poor	0.94	5
Wavelength			
VIMS OFT	<u>vs.</u> CERC OFT		
	good	0.63	11
	fair	0.77	15
	poor	0.52	5

VIMS OFT <u>vs.</u> VIMS ZTS			
	good	0.79	11
	fair	0.75	15
	poor	0.53	5
CERC OFT <u>vs.</u> VIMS ZTS			
	good	0.46	11
	fair	0.64	15
	poor	0.62	5

c. ERIM Subimage Locations. 18 Samples.

Variable	Quality	Correlation Coefficient	# Samples
Direction			
VIMS OFT <u>vs.</u> ERIM OFT			
	good	0.97	6
	fair	0.64	7
	poor	0.54	3
VIMS OFT <u>vs.</u> VIMS ZTS			
	good	0.98	6
	fair	0.91	7
	poor	-	2
ERIM OFT <u>vs.</u> VIMS ZTS			
	good	0.96	6
	fair	0.88	8
	poor	0.67	4
Wavelength			
VIMS OFT <u>vs.</u> ERIM OFT			
	good	0.88	6
	fair	0.63	6
	poor	0.79	3
VIMS OFT <u>vs.</u> VIMS ZTS			
	good	0.95	6
	fair	0.81	7
	poor	-	2
ERIM OFT <u>vs.</u> VIMS ZTS			
	good	0.90	6
	fair	0.50	7
	poor	0.52	4

TABLE 7
Correlation Coefficients for Combinations of ZTS and OFT Data Sets.
With and Without Poor OFT data.

Measurement Sources	Subimage Locations	Variable	Combined Data Set		Omit Poor OFT Data	
			# Samples	r	# Samples	r
OFT vs. OFT						
VIMS OFT vs. CERC OFT	CERC	Direction	31	0.82	26	0.85
		Wavelength		0.67		0.67
VIMS OFT vs. ERIM OFT	ERIM	Direction	16	0.67	13	0.72
		Wavelength		0.71		0.74
ZTS vs. OFT						
VIMS ZTS vs. CERC OFT	CERC	Direction	32	0.90	26	0.88
		Wavelength		0.56		0.54
VIMS ZTS vs. ERIM OFT	ERIM	Direction	18	0.74	14	0.89
		Wavelength	17	0.55	13	0.64
VIMS ZTS vs. VIMS OFT	VIMS+ ERIM	Direction	48	0.03	34	0.80
		Wavelength		0.71		0.79
VIMS ZTS vs. VIMS OFT	CERC	Direction	31	0.88	26	0.95
		Wavelength		0.74		0.78

measurements made in the outside laboratories. The intercomparison presented here, then, is for VIMS OFT vs. ERIM OFT, and VIMS OFT vs. CERC OFT.

Several scatterplots for comparisons in both wavelength and direction, using data for the CERC stations as examples, are presented in Figures 13-18. Correlation coefficients for all the data are in Table 7. From Figure 13, and other data not shown, it is evident that wavelength values measured by VIMS OFTs are slightly higher than those measured by both external laboratories, despite the use of Ronchi rulings as calibration standards. The bias is usually about 6%, with occasional wide deviations. Careful re-examination of all VIMS OFTs from the CERC stations showed that many contained multimodal spectra. The published CERC data contained only single wavelength and direction pairs for each station. It is believed that some of the deviations are the result of selection for measurement of different wavetrains in crossed seas.

For direction, virtually all direction values agree to within ± 5 degrees (see for example Figure 14). The comparison of VIMS OFT vs. CERC OFT produced slightly higher correlation values than the VIMS OFT vs. ERIM OFT comparison. A plausible reason for this result is that the CERC set involved the larger OFT aperture (11 mm vs. 5 mm for the ERIM OFTs).

The data in Table 7 show that OFT direction measurements from different laboratories have higher correlations ($r = 0.85$ and 0.72) than OFT wavelength measurements ($r = 0.67$ and 0.72).

d. Comparison of ZTS with OFT Measurements

The comparison of ZTS with OFT measurements provides a measure of the ZTS method against the widely-used OFT. Data for the CERC stations are again used for illustration, but all the correlation results are presented in Table 7 (see the right-hand column). For wavelength, ZTS and CERC OFT data are compared in Figure 15. Somewhat greater scatter is found here, with the ZTS, than in Figure 13 with the VIMS OFT. Between ZTS and external laboratory data, the r values for wavelength for ERIM and CERC stations disagree by 0.10. There is negligible difference, however, between the direction correlation coefficients. These on average are much higher than for wavelength (0.88 vs. 0.59). Some of the same data are illustrated differently in Figure 16, which compares the direction differences between methods taken in pairs. Agreement is largely within ± 5 degrees.

The internal comparison of VIMS ZTS vs. VIMS OFT wavelength data, in Figure 17, shows again a scatter of wavelength deviations whose mean is roughly 6%. There is no apparent bias here; thus, VIMS wavelength values are internally self-consistent. The r values for the ERIM and CERC stations are nearly identical (0.79 and 0.78).

For the direction measurements, however, there is a significant difference between correlation coefficients. For the set of 11 mm circles (CERC locations), $r=0.95$, while for the set of 5 mm squares

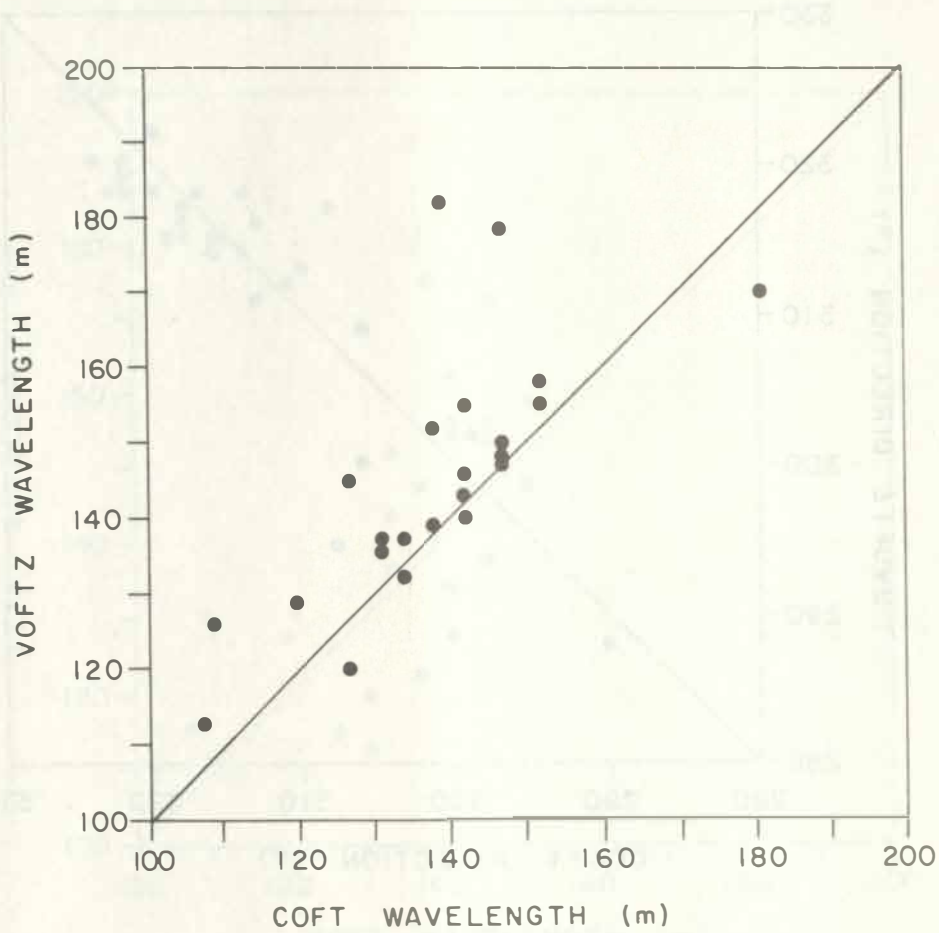


Figure 13. OFT intercalibration results. VIMS OFT vs. CERC OFT. Wavelength. For Figures 13-18, the labels on the axes indicate the laboratory and method of data extraction, e.g. DCOFT = direction measurement (D) from CERC (C) OFTs (OFT).

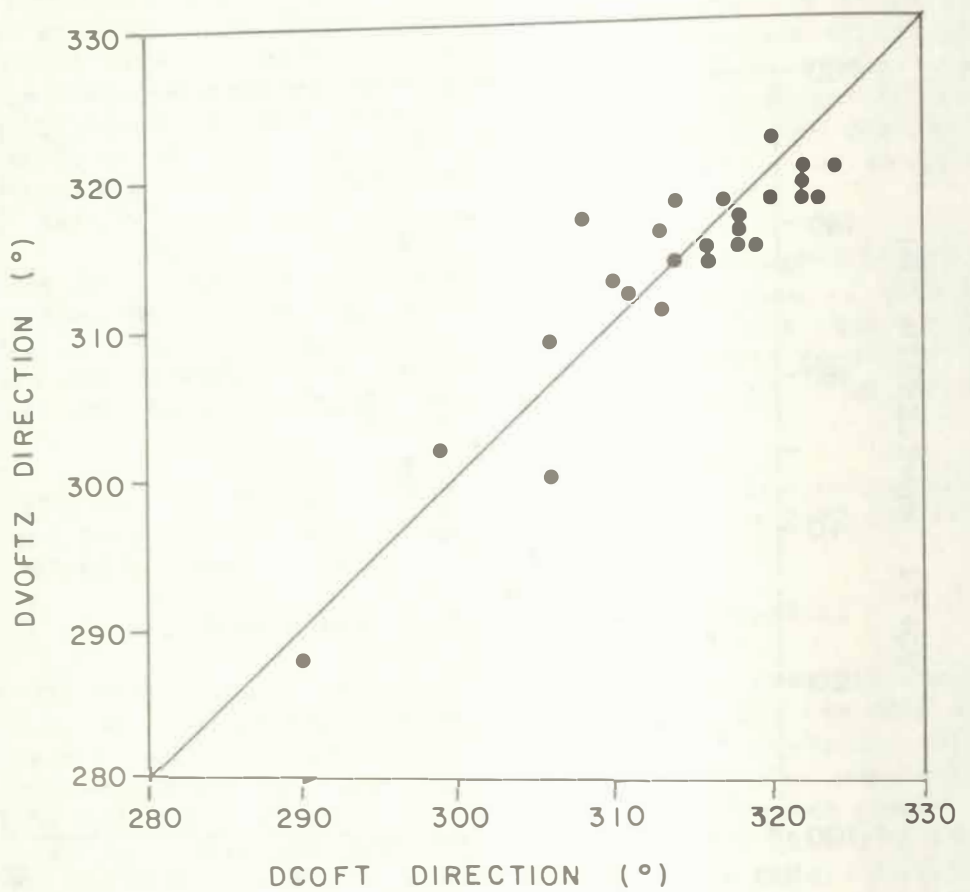


Figure 14. OFT intercalibration results. VIMS OFT vs. CERC OFT. Direction. See legend for Figure 13.

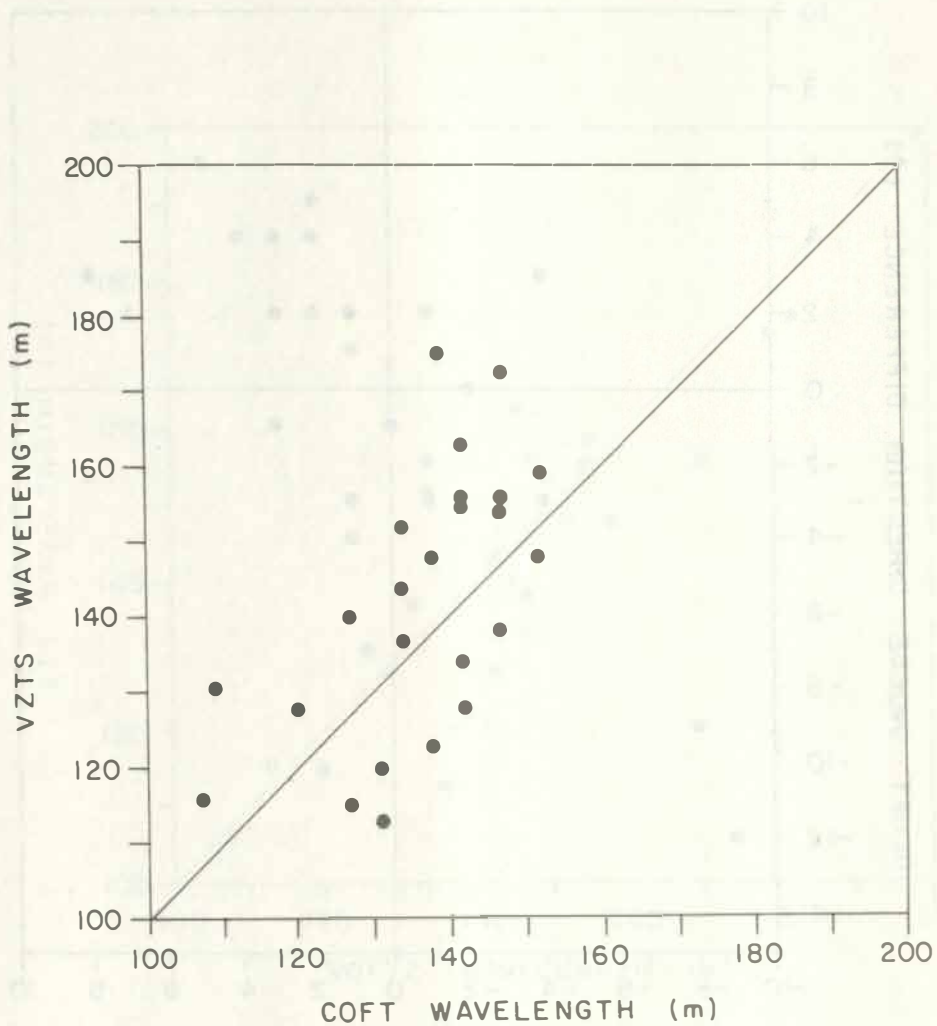


Figure 15. ZTS-OFT intercalibration results. VIMS ZTS vs. CERC OFT. Wavelength. See legend for Figure 13.

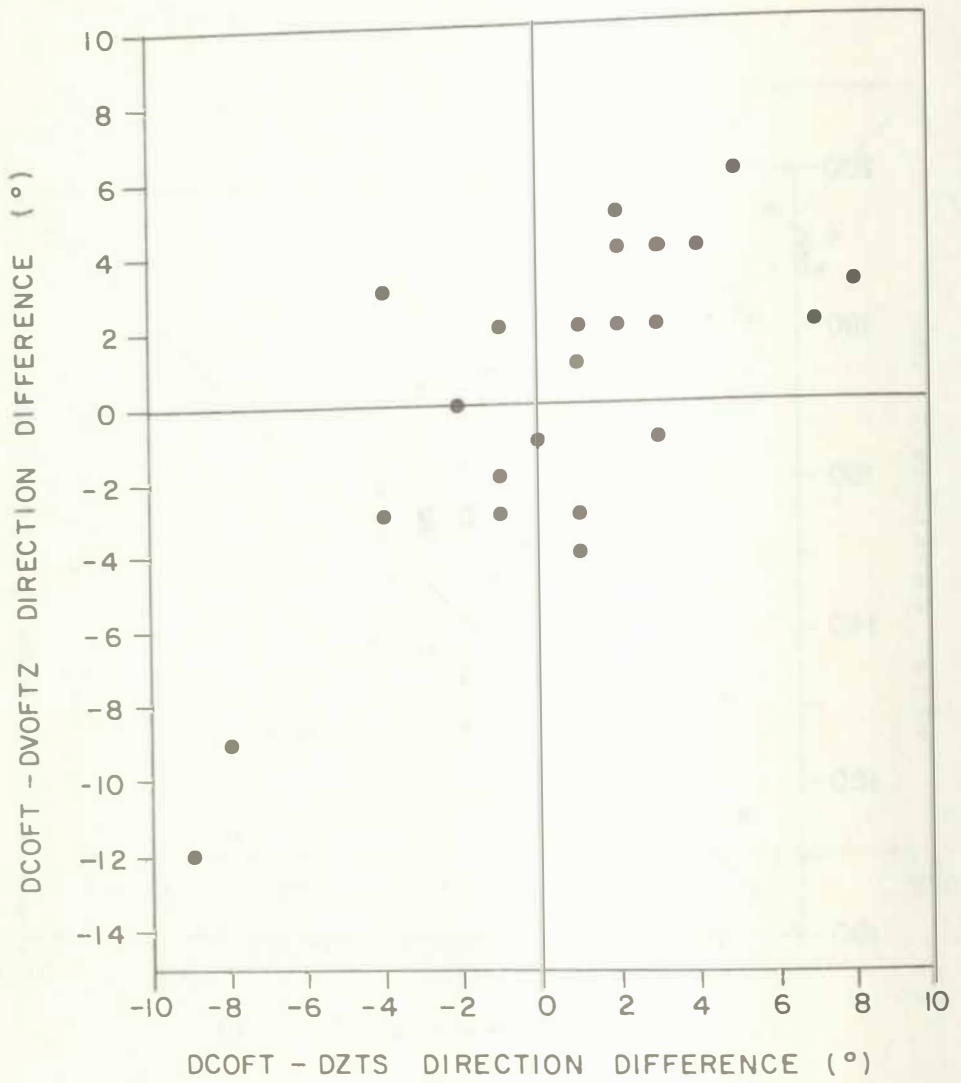


Figure 16. Comparison of deviations in direction values from different methods, VIMS and CERC data. See legend for Figure 13.

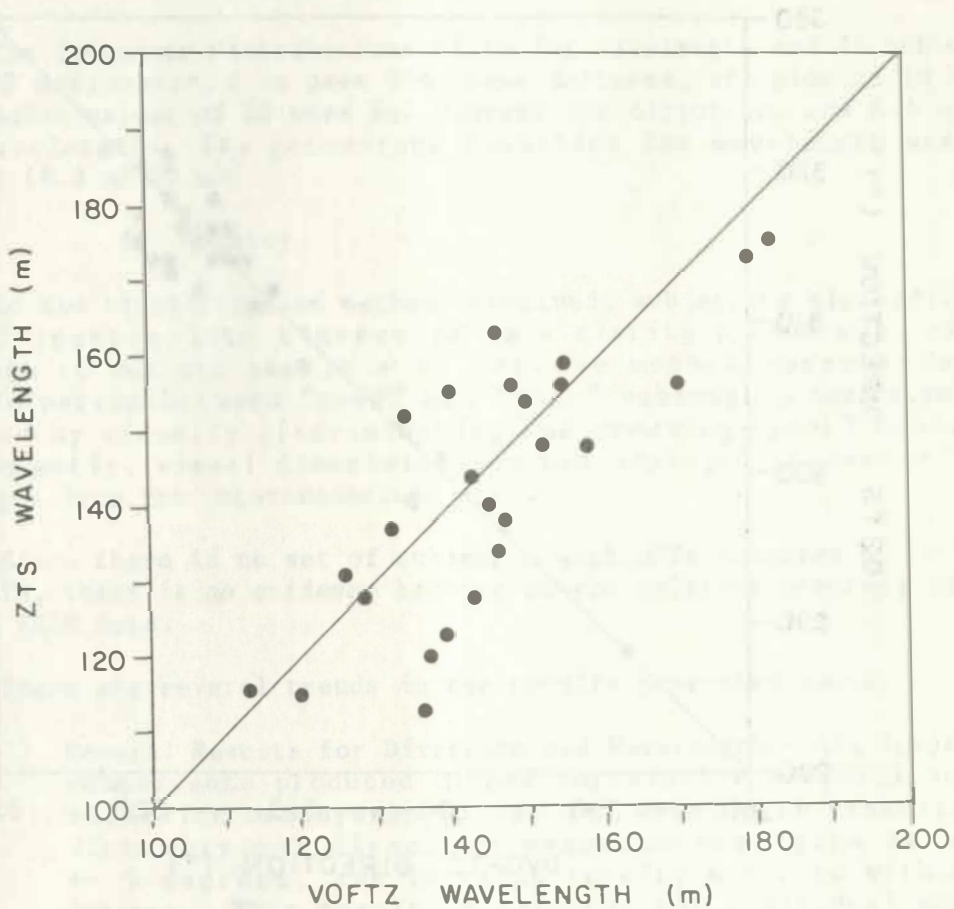


Figure 17. Internal VIMS comparison for wavelength data, ZTS vs. OFT. CERC stations. See legend for Figure 13.

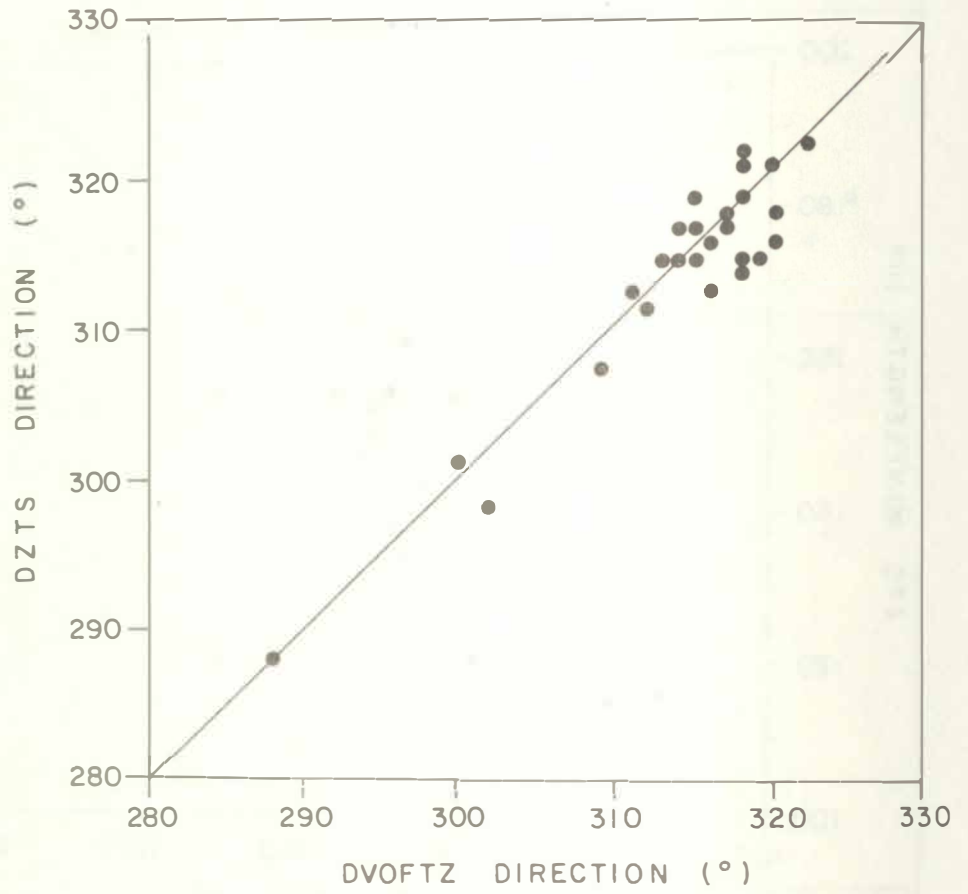


Figure 18. Internal VIMS comparison for direction data, ZTS vs. OFT. CERC stations. See legend for Figure 13.

(VIMS + ERIM locations), $r=0.80$. Again, this is evidence that a larger OFT aperture size improves the measurement of direction.

The internal comparison of direction measurements is illustrated in Figure 18. The figure shows that virtually all individual direction measurements at VIMS agree to within 2 degrees. This very high agreement is in part a consequence of careful selection of wave trains in crossed seas.

e. Precision of ZTS measurements

The frequency distributions of Sd for wavelength and direction for 140 ZTS measurements on pass 974, Cape Hatteras, are plotted in Figure 19. Median values of Sd were 1.2 degrees for direction, and 8.8 metres for wavelength. The percentage deviation for wavelength was ± 6 percent (8.8 m/150 m).

f. Summary

Of two stratification methods examined, subjective classification of OFT spectra into classes of wave clarity proved most useful. Although it was not possible to improve method correlations by discriminating between "good" and "fair" subimages, improvement was achieved by visually discriminating and removing "poor" subimages. Consequently, visual discrimination was employed to remove "poor" subimages from the intercomparison sets.

Since there is no set of subimages with OFTs measured by both CERC and ERIM, there is no evidence bearing on the relative accuracy of CERC versus ERIM data.

There are several trends in the results presented above:

- 1) General Results for Direction and Wavelength-- All intermethod comparisons produced higher correlation coefficients for direction measurements than for wavelength measurements. Virtually all direction measurements agree to within ± 5 degrees, and intralab results agree to within ± 2 degrees. This result is obtained for individual absolute deviations, not composite statistical measures. Wavelength deviations are usually within 6%, but there are occasional wide deviations.
- 2) Subimage Size-- Regardless of method, direction measurements from 11 mm circular subimages produced higher correlation coefficients than measurements made from 5 mm squares or circles. Therefore, larger subimages improve measurement precision.
- 3) ZTS Precision for Direction and Wavelength-- Precision of ZTS measurements was high. For four replicate measurements taken from 140 subimages at Cape Hatteras, the median Sd for wavelength was 8.8 metres, and Sd for direction was 1.2 degrees.

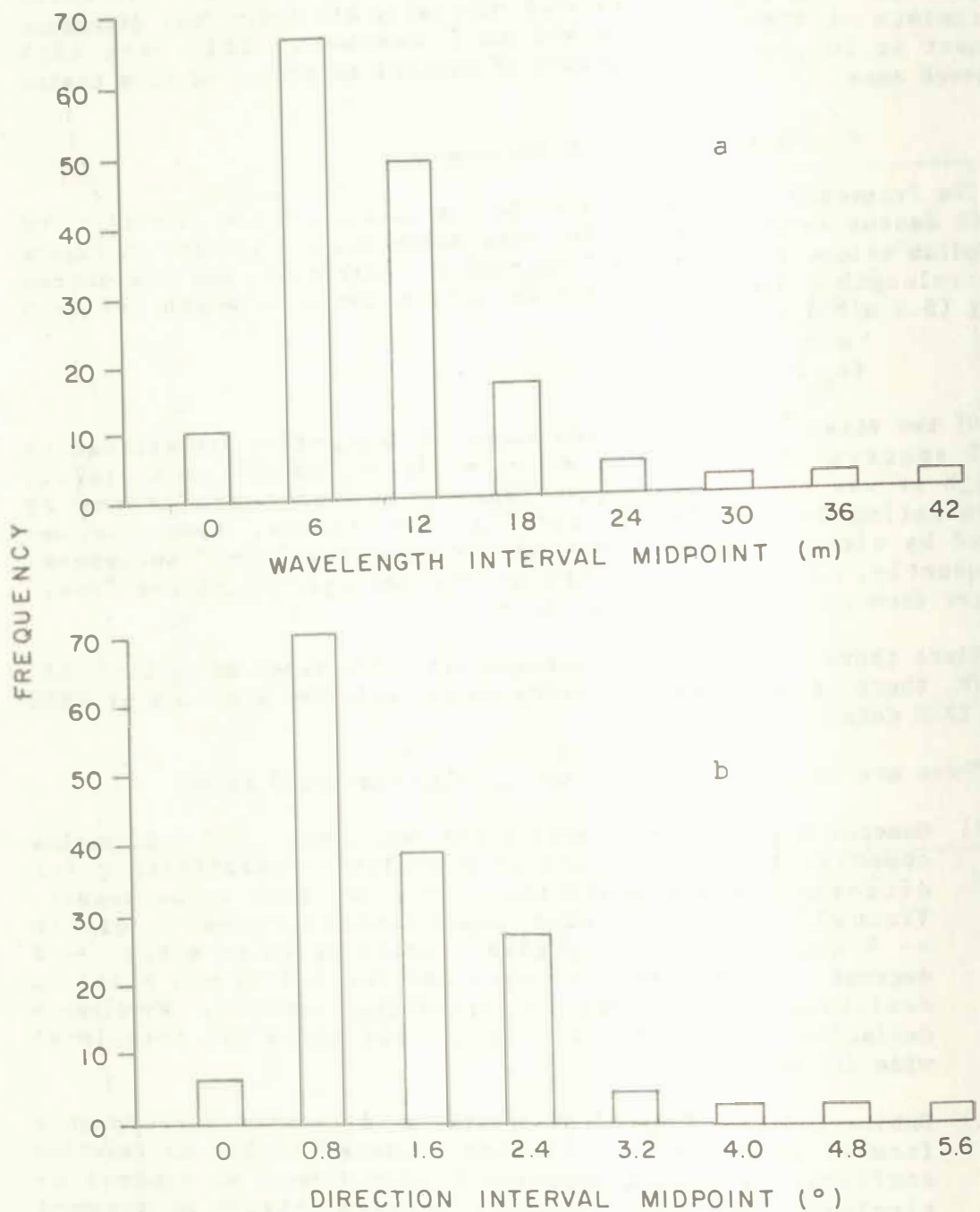


Figure 19. Histogram of standard deviation of the mean for ZTS measurements. Four measurements per point.
 a. wavelength.
 b. direction.

- 4) ZTS Accuracy for Direction-- There are no independent direction data available to test absolute accuracy. Intercomparisons indicate that the absolute accuracy of direction measurements is between 1 and 2 degrees. On the basis of the better-than 2-degree accuracy in direction measurements using the ZTS, and the obvious curvature in the Cape Hatteras wave field of 20 to 30 degrees, the ZTS method is sufficiently accurate for testing the VSWCM.
- 5) ZTS Accuracy for Wavelength-- Again, there are no independent data to test absolute accuracy. ZTS wavelength values have acceptable precision, and are consistent with VIMS OFT measurements, but the correlation with measurements from external lab OFTs was smaller than would be satisfying. The ZTS/OFT correlations were lower than the OFT/OFT correlations, but the internal VIMS ZTS/OFT correlations were the highest. Due to this inconsistency, the absolute accuracy of wavelength measured by the ZTS is uncertain. The results suggest that the mean absolute accuracy is around 6%.
- 6) OFT Accuracy for Wavelength-- Values from VIMS OFTs were biased high (perhaps 6%) compared to other OFT data. However, ZTS and VIMS OFT wavelength values were generally consistent. Again, no independent data from the field are available to test absolute accuracy.

It will be seen in the results which follow that the maps obtained from the SAR data suggest the absence of noise in ZTS direction measurements. The smooth patterns which are revealed on the wave ray vector maps and ray diagrams (before and after interpolation) indicate entirely satisfactory representation of wave fields. Also, ZTS data have been confirmed by checking against OFT data for all important features of the analyses.

Finally, the levels of agreement for sets of wavelength and direction measurements are most reasonable, considering the inherent ranges in the two parameters as seen on hundreds of OFTs from VIMS, CERC, and ERIM.

F. Plotting SAR Data on the VSWCM Grid

To convert points from the SAR grid to corresponding points on the VSWCM grid, an algorithm had to be developed. A linear transformation is appropriate, as both grids are linear. A simple multiple regression was used, based on an affine transformation (Kirby and Steiner, 1977):

$$\begin{aligned} x &= Ax' + By' + C \\ y &= Dx' + Ey' + F \end{aligned} \quad (3)$$

To calculate the constants, a series of common x', y' points (on the SAR grid) and x, y points (on the VSWCM grid) was generated by

optical superposition of land forms from SAR imagery onto land forms previously traced on the VSWCM grid. SAR points were transferred onto the VSWCM grid, and x', y' readings were made with a Numonics electronic planimeter. A multiple linear regression was used to calculate the constants above. The resulting transformation scales, rotates, and translates points from one grid to the other. Because only a small area could be used as a training area (approximately an 80 x 25 km area), location errors probably increase with distance as the transformation is extrapolated away from the training area.

G. Generation of Rays by Interpolation

A computer program was written to interpolate wave rays using the grid measurements from the Seasat imagery. Figure 20 shows a flow chart for the program, henceforth referred to as the SAR ray interpolation program. Initial points for computing interpolated rays were the series of subimages forming the eastern boundary of the array. Each ray was constructed by successive interpolation of the direction field, using an increment length of one-quarter of the grid spacing. The program interpolated wavelength and direction using the four nearest grid points. The weighting scheme is an exponentially-weighted average according to

$$X = \frac{\sum_{i=1}^4 X_i e^{-(r_i/F)^2}}{\sum_{i=1}^4 e^{-(r_i/F)^2}} \quad (4)$$

where X = interpolated direction or wavelength, X_i = direction or wavelength measured at station i , r_i = distance in km from point i to the ray point, and F = weighting coefficient. The option of setting the value of F to the appropriate level allows the programmer to vary the relative weighting of the nearby points. F controls the "pinching" of the Gaussian weighting expression in Equation (4). The impact of different F values was examined for the hypothetical situation shown in Figure 21a. An array was constructed with a lattice spacing of 10 arbitrary units, and with a region of more dense spacing produced via interstitial points in the upper center. Directions of vectors were established as shown; the orthogonality of vectors in the pattern established an extreme condition. The use of different F values in Equation 4 produced the results shown in Figure 21 b,c,d. The ratios of F to nominal grid spacing for these results are 0.5, 1.0, and 2.0 respectively. From the above testing, an F value of 5 km was chosen for the SAR grid which had a spacing of 7 km. This represents a ratio of 0.71.

H. Analysis of Sampling density

1. Introduction

When measuring a two dimensional field with point measurements, sampling density should be inversely proportional to field uniformity. Where the field is uniform, sampling density can be low, but where it

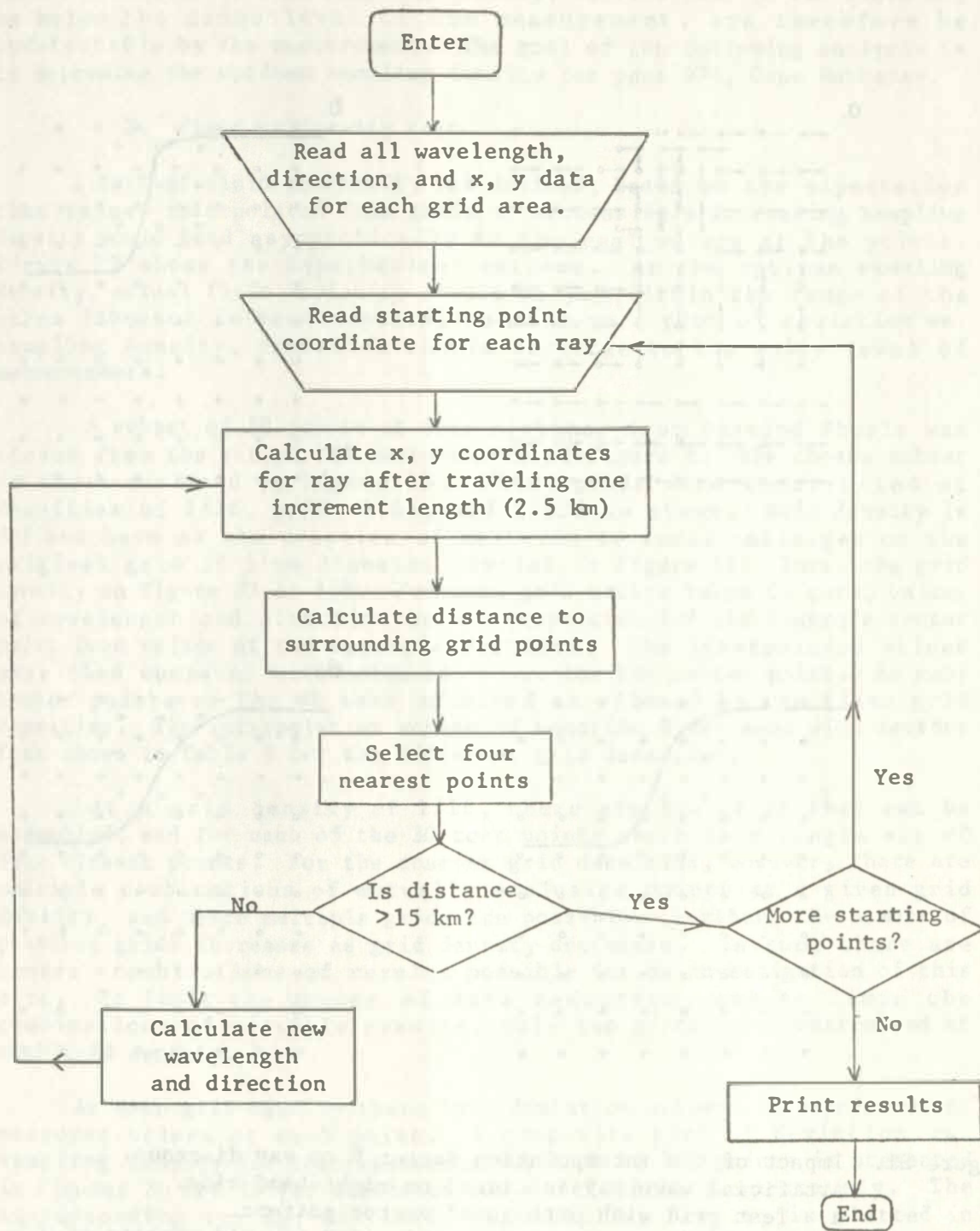


Figure 20. Flow chart for interpolating rays of the direction field measured from the SAR imagery.

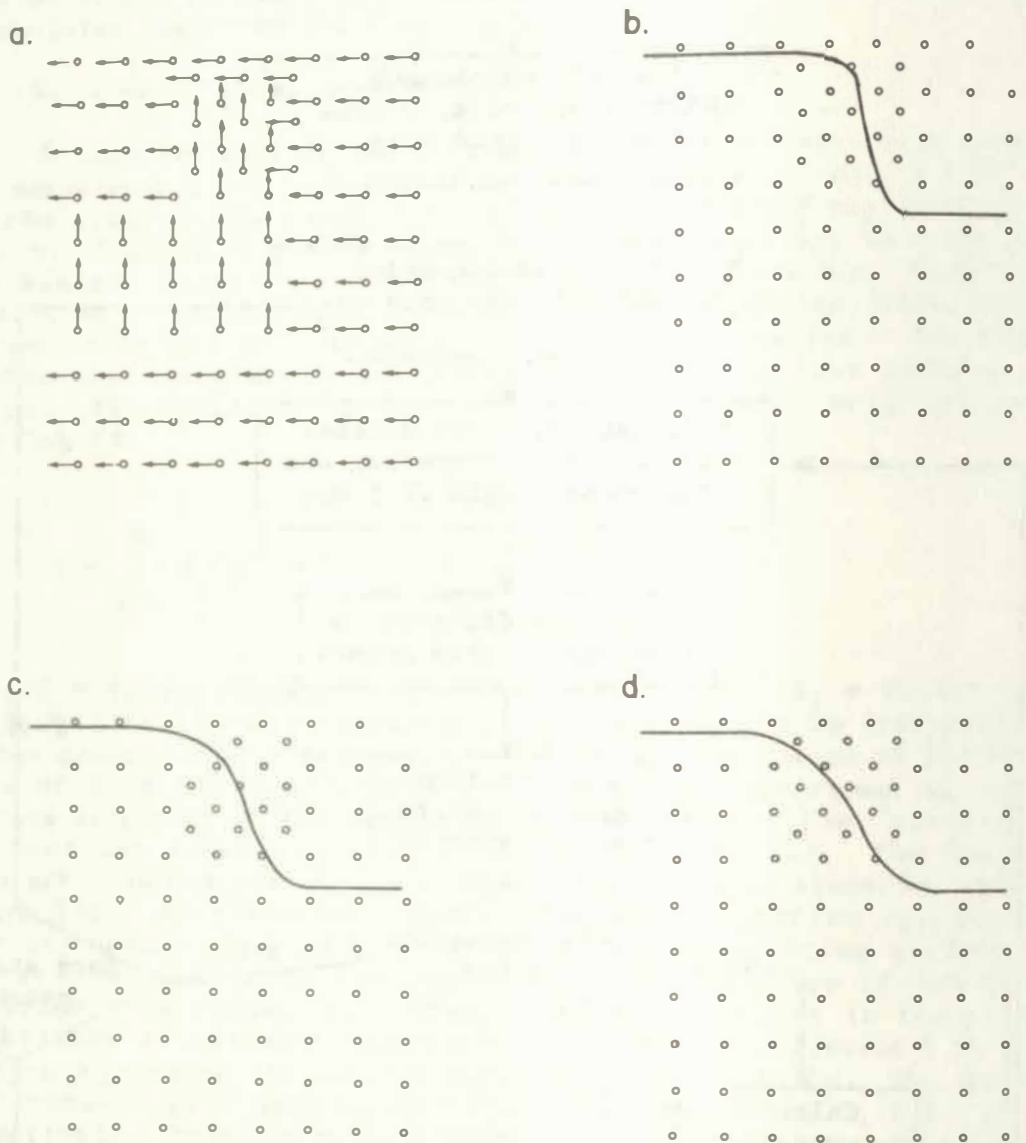


Figure 21. Impact of the interpolation factor F on ray diagrams. Artificial wave ray initiated on right-hand side.

- Test grid with orthogonal vector pattern.
- Artificial wave ray for ratio of F to grid spacing of 0.5.
- Artificial wave ray for ratio of F to grid spacing of 1.0.
- Artificial wave ray for ratio of F to grid spacing of 2.0.

exhibits significant fluctuations, sampling density must be sufficient to record the irregularities. Also, the level of detail obtained at each field point depends on the resolution of each measurement. Even with a sufficiently high sampling density, fluctuations in the field may be below the noise level of the measurement, and therefore be undetectable by the measurement. The goal of the following analysis is to determine the optimum sampling density for pass 974, Cape Hatteras.

2. Field uniformity test

A test of field uniformity was devised, based on the expectation that values interpolated from grids at successively increasing sampling density would tend asymptotically to the real values at the points. Figure 22 shows the hypothetical outcome. At the optimum sampling density, actual field variation should be just within the range of the error inherent in measurements, so that on a plot of deviation vs. sampling density, deviation should converge to the noise level of measurements.

A subset of 30 points at some distance from Diamond Shoals was chosen from the set of ZTS measurements of Figure 8. The chosen subset is shown enclosed on Figure 23. Then, grids were constructed at densities of 1/16, 1/32, 1/64, and 1/128 as shown. Grid density is defined here as the fraction of measured to total subimages on the original grid of 5 mm diameter circles in Figure 11. Thus, the grid density on Figure 23 is 1/8. For each grid square taken in turn, values of wavelength and direction were interpolated for the square's center point from values at the square's vertices. The interpolated values were then compared with measured values for the center point. As many center points of the 30 were examined as allowed by the given grid densities. The interpolation scheme of Equation 4 was used with factors F as shown in Table 8 for the different grid densities.

At a grid density of 1/16, there are two grids that can be assembled, and for each of the 30 test points there is a single set of four closest points. For the coarser grid densities, however, there are multiple combinations of mutually exclusive points at a given grid density, and hence multiple grids are possible. Further, the number of possible grids increases as grid density decreases. In sum, there are several combinations of results possible for an investigation of this sort. To limit the amount of data reduction, and to limit the combinations of possible results, only two grids were constructed at each grid density.

At each grid density there is a deviation between interpolated and measured values at each point. A composite plot of deviation vs. sampling density for ten representative (out of 30) points is presented in Figures 24 and 25 for direction and wavelength, respectively. The corresponding average deviation vs. sampling density is plotted in Figure 26. For the 30 points used in Figures 24 to 26, the Sd for the original measurements of wavelength and direction averaged 9.64 m and 1.05 degrees, respectively. Figure 26 shows that for wavelength, the field is sufficiently uniform that the deviation of interpolated values from measurement (roughly 10 to 12 m) at each grid density is

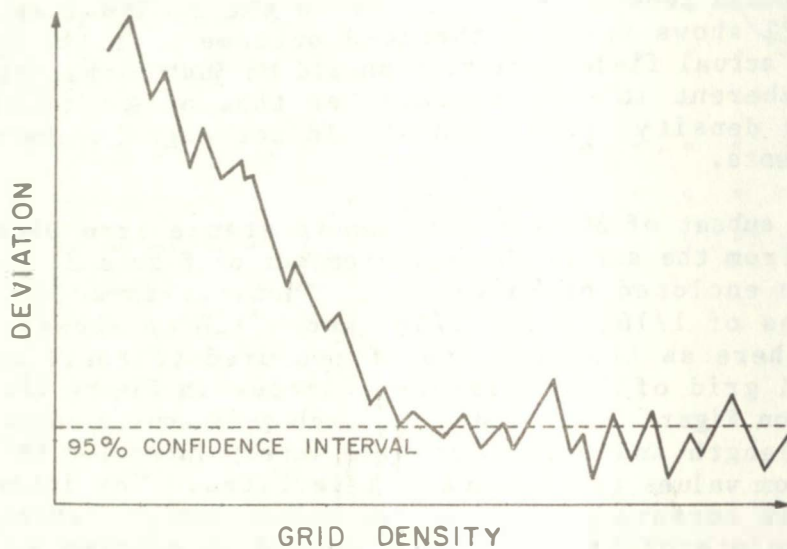


Figure 22. Hypothetical convergence of interpolated values to measured value for increasing measurement-grid densities.

SAR DATA POINTS

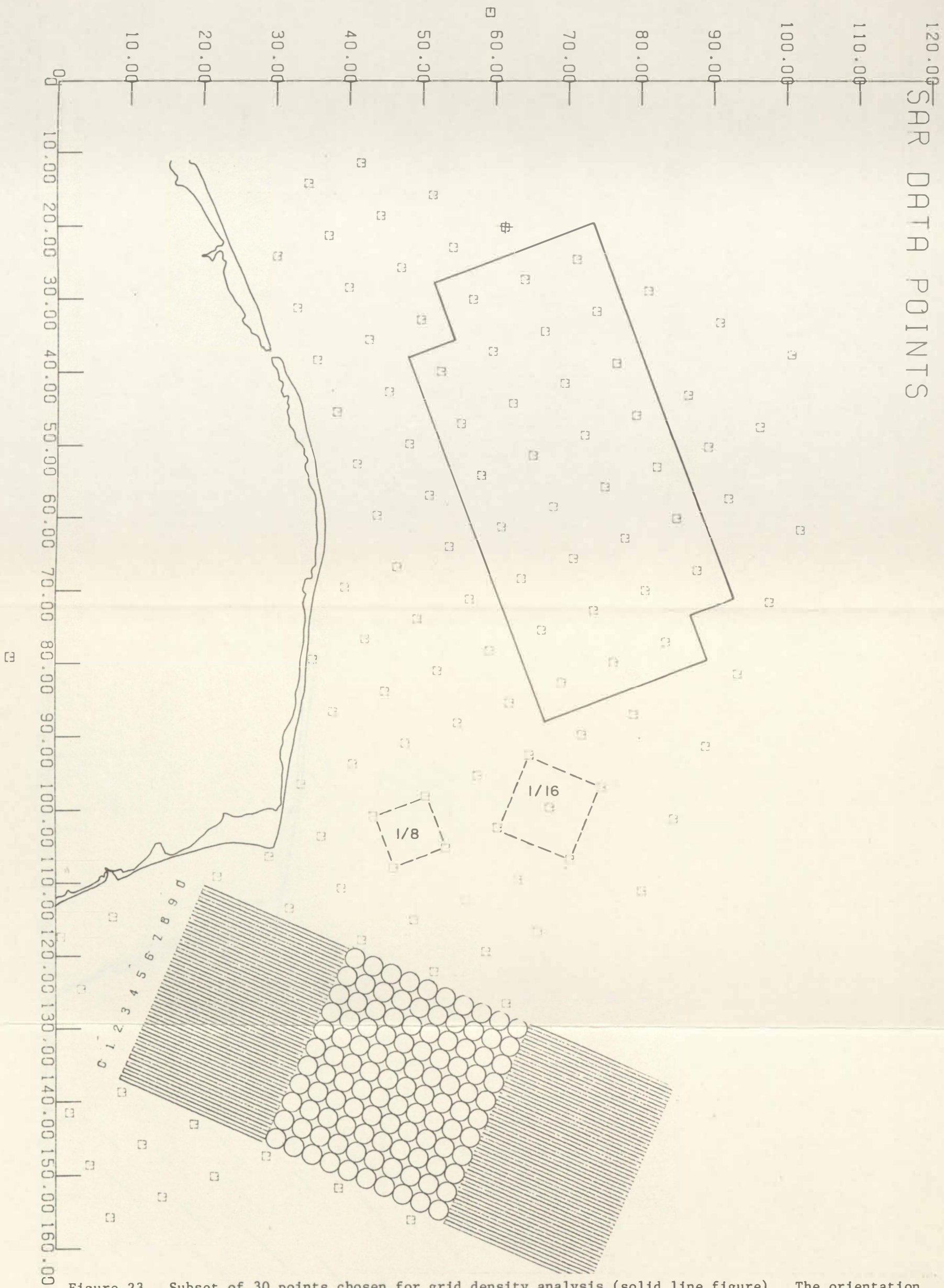


Figure 23. Subset of 30 points chosen for grid density analysis (solid line figure). The orientation of the sampling grid overlay from Figure 11 is shown at the bottom. Representative grid densities are shown in the middle as dotted lines.

TABLE 8
 Distance Weighting Factor F for Various Grid Densities.
 Weighted by $\exp(-(r_i/F)^2)$.

Grid Density	Minimum Interstitial Distance (km)	F Value (km)
1/ 8	7.07	5.00
1/ 16	10.00	7.07
1/ 32	14.14	10.00
1/ 64	20.00	14.14
1/128	28.28	20.00

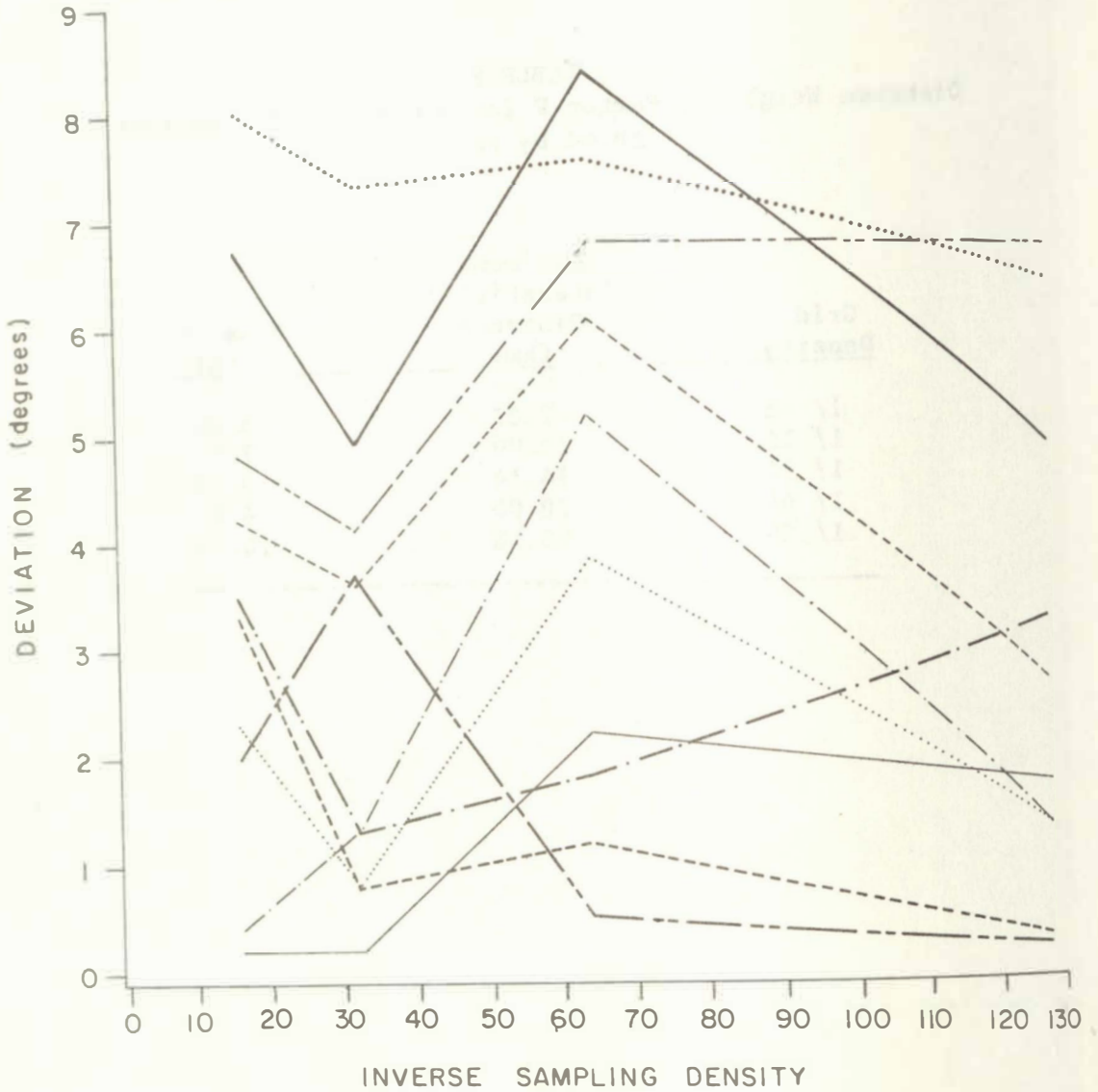


Figure 24. Deviations of interpolated direction vs. inverse grid density. Typical results.

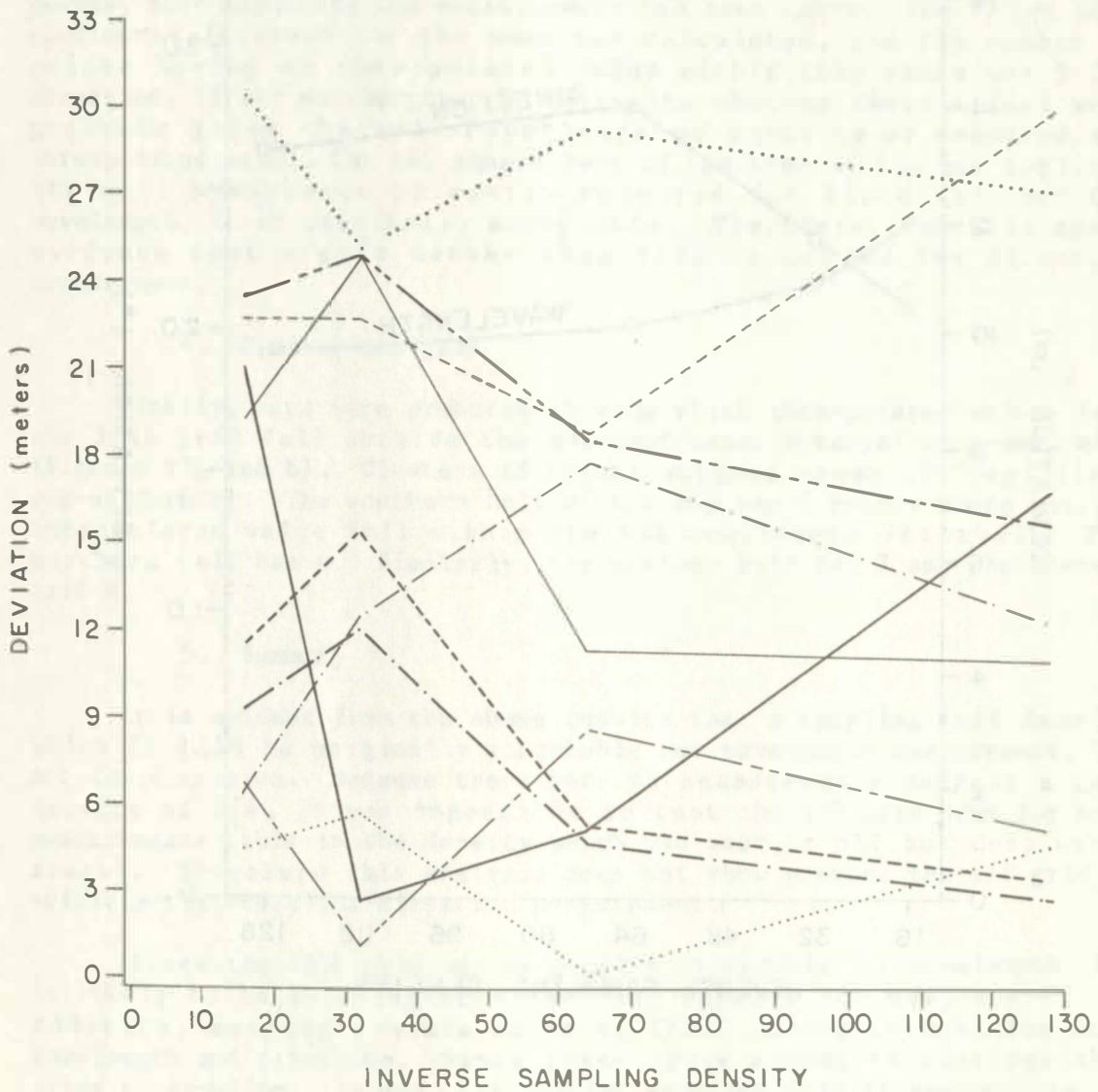


Figure 25. Deviations of interpolated wavelength vs. inverse grid density. Typical results.

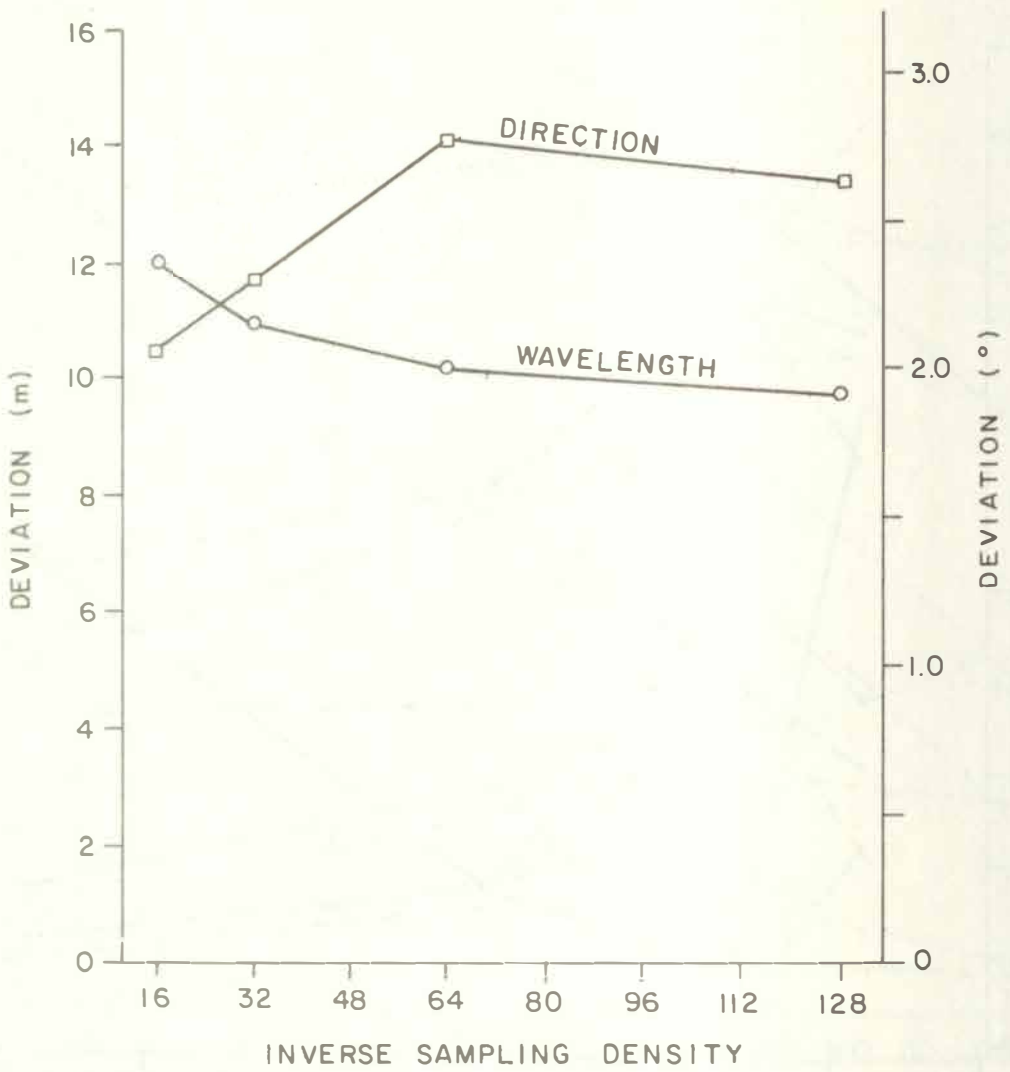


Figure 26. Average deviations of interpolated wavelength and direction vs. inverse grid density. $n = 30$.

approximately equal to S_d . For direction, however, the average deviation of interpolated values from measurement (roughly 2 degrees), is almost twice as large as S_d , and the optimum grid density has not been reached.

3. Test of the 1/16 Grid

Since the individual deviation values were widely dispersed, as can be seen in Figures 24 and 25, a more specific test of conformity was applied to the second densest grid, 1/16. For each of the 30 test points, four replicate ZTS measurements had been taken. The 60 per cent confidence interval for the mean was calculated, and the number of points having an interpolated value within this range was 9 for direction, 12 for wavelength. To determine whether these values were probable given the null hypothesis of equality of measured and interpolated value, the chi square test of goodness of fit was applied. The null hypothesis is easily rejected for direction, but for wavelength, it is marginally acceptable. Therefore, there is again evidence that a grid denser than 1/16 is needed for direction measurement.

4. Cluster analysis

Finally, maps were prepared showing which interpolated values from the 1/16 grid fell outside the 60% confidence interval of measurement (Figures 27a and b). Clusters of points suggest areas of local field non-uniformity. The southern half of the map has 7 points where neither interpolated value fell within the 60% confidence interval. The northern half has 4. Similarly, the western half has 7 and the eastern half 4.

5. Summary

It is evident from the above results that a sampling grid density which is 1/16 is marginally acceptable for wavelength measurement, but not for direction. Because there were no measurements made at a grid density of 1/4, it was impossible to test the 1/8 grid used for most measurements (this is the density which was used in all but deep water areas). Therefore this analysis does not show whether the 1/8 grid is sufficiently dense for direction measurement.

Since the 1/16 grid was marginally acceptable for wavelength, 1/8 is likely to be an acceptable sampling density for wavelength. In addition, mapping reveals areas of field non-uniformity for both wavelength and direction. Since these areas cannot be distinguished prior to sampling, the use of a regular sampling grid is appropriate.

IV. Geometric Errors from Superimposing SAR Imagery onto VSWCM Ray Diagrams

It was predicted earlier that angle and location errors from map generation might reach one degree and one kilometre. By superimposing landforms present on both SAR and VSWCM images, the magnitude of actual geometric errors in the SAR and VSWCM comparisons may be seen directly.

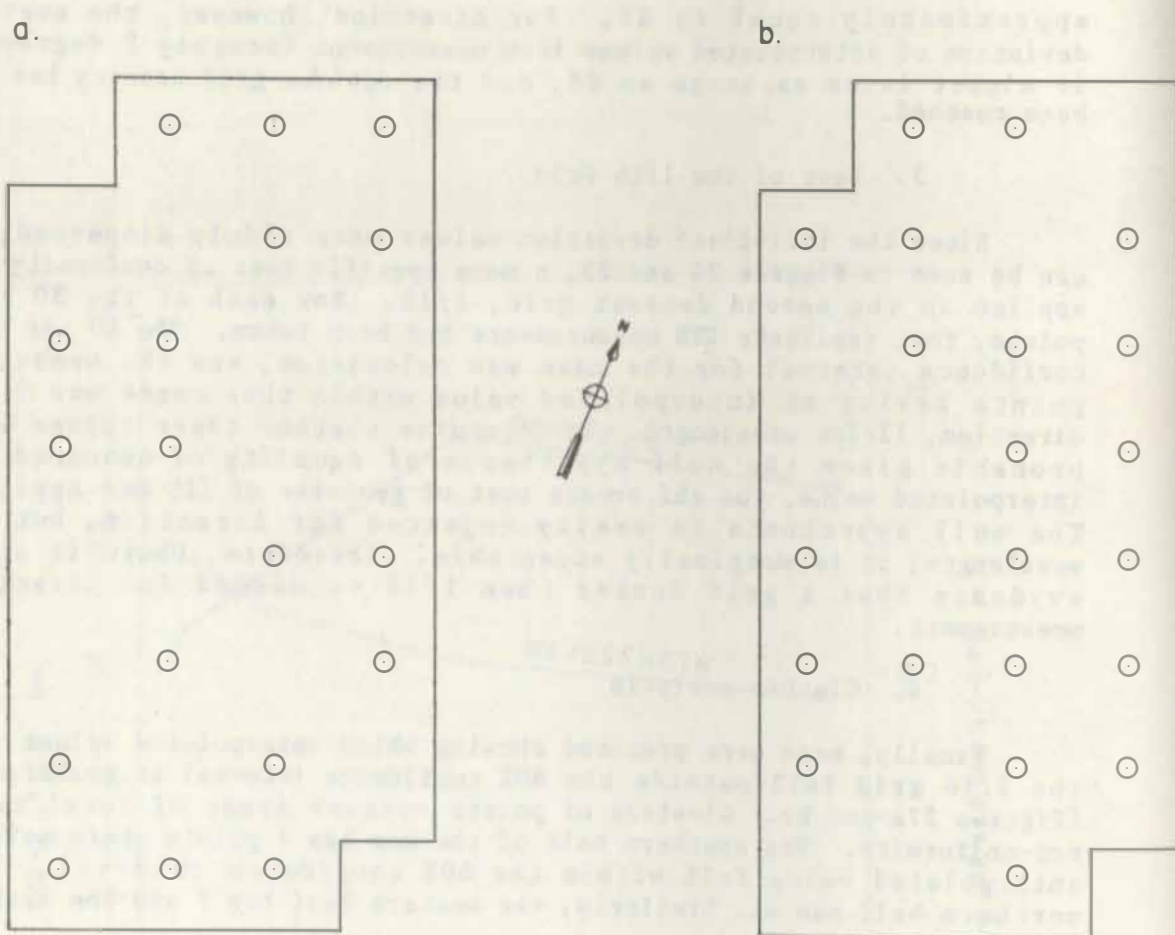


Figure 27. Distribution of absolute deviations (interpolated versus measured values) which fail the 60% confidence interval.
 a. wavelength.
 b. direction.

The landforms cannot be superimposed perfectly. If the best fit is made in either the southern or northern portion, there is a 3 mm (1.5 km) offset in the North-South direction (Figure 28), the VSWCM shoreline being slightly longer than that of the SAR. There is also a 2 degree angular difference between the northerly and southerly best-fit orientations. An intermediate orientation was used for measurements from the imagery, producing 1 degree and 0.75 km deviations at the extremes of the area studied.

According to the auxiliary data listing from JPL, the clock angle perpendicular for the satellite interpolated in the center of this region was 295.8 degrees. The satellite bearing is offset 90 degrees to the South, and is therefore 205.8 degrees. This differs slightly from the range orientation derived from superimposing landforms, which was 203.8 degrees. The discrepancy may be due in part to the method of entering the shoreline onto the VSWCM diagrams, namely, the use of the zoom transfer scope to trace the shoreline onto the VSWCM bathymetric grid (with a scale of 1:180,000) from a 1:250,000 topographic sheet (Manteo) with latitude and longitude tic marks serving as a reference frame. However, the VSWCM grid is established on a dimensionally-stable mylar sheet, which has been checked and examined repeatedly since its production, and the location of landforms appears to be accurate. With respect to other possible causes of geometric error, slant range distortion would produce only a maximum displacement of 0.5 mm in the range dimension. The suspected cause of geometric error is irregularity in the SAR film scale. Scale changes have been measured to be 2-10% in the azimuth dimension, and up to 17% in the range dimension (Gonzales et al., 1979).

Thus there are several sources of error encountered when superimposing VSWCM ray diagrams onto a plot of wave direction vectors measured from SAR imagery. The magnitudes of angular errors and location displacements derived from major sources are presented in Table 9. Total error is calculated by:

$$E_{\text{total}} = \left[\sum_i E_i^2 \right]^{1/2} \quad (5)$$

where E_i = error from source i .

For extreme conditions, the maximum total angular error is 1.69 degrees and the maximum total location error is 1.03 km.

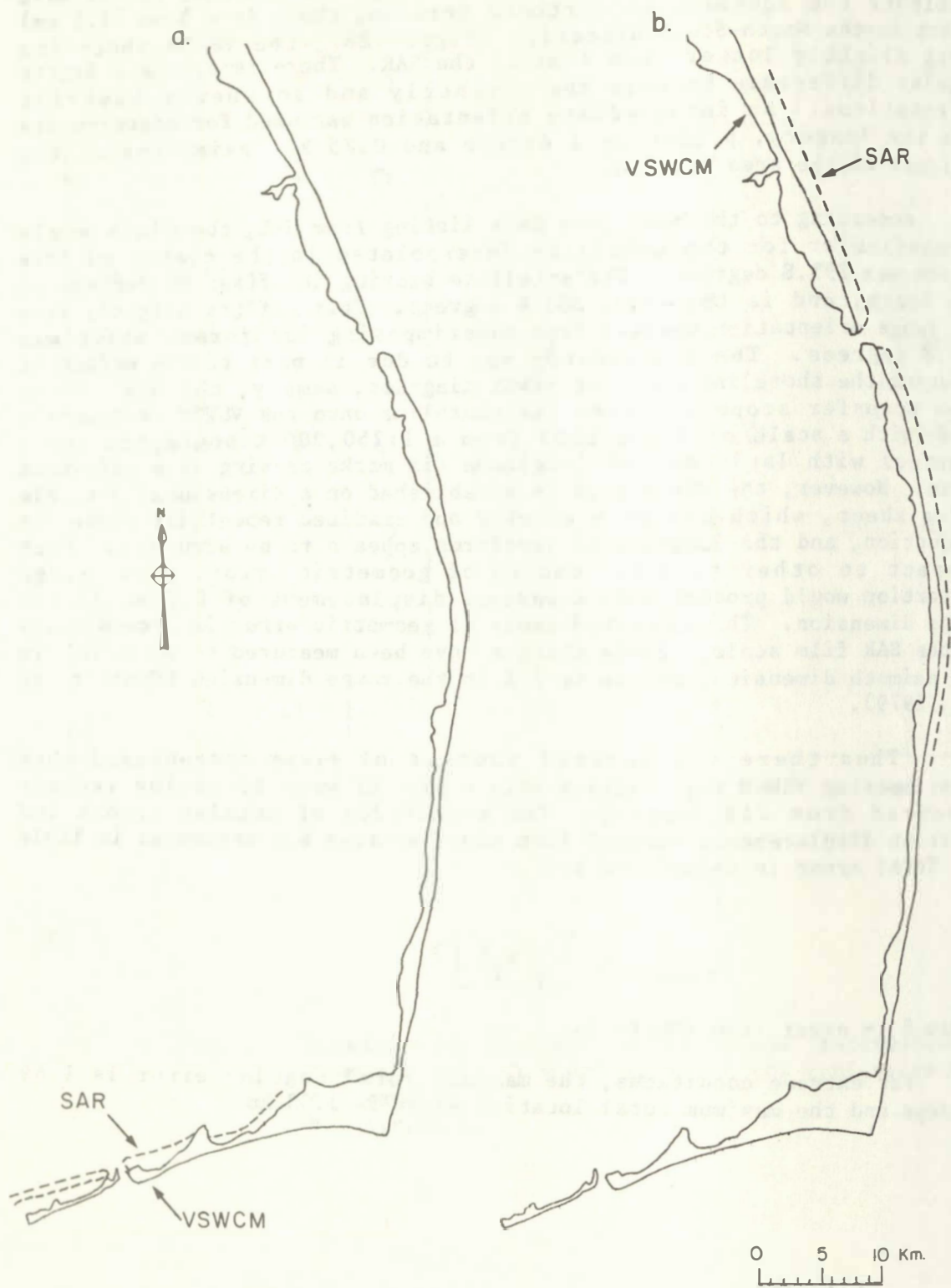


Figure 28. Best fit of SAR and VSWCM maps of landforms.
 a. Best fit in northern region.
 b. Best fit in southern region.

TABLE 9
Error Factors and Resultant Maximum Errors.

Source	Area Affected	Maximum Error
Angular Errors in Degrees:		
slant range scale distortion	within 2.5 cm circular subimage	0.2°
slant range scale distortion	across a subswath	-1.21°
range walk	along 200 km on image	0.60°
map projection	along 200 km on image	1.00°
		E max = 1.69°
Location Errors in Kilometres:		
slant range scale distortion	within a subswath	0.25 km
range walk	along 200 km on image	1.00 km
map projection	along 200 km on image	0.05 km
		E max = 1.03 km

RESULTS AND DISCUSSION

I. Cape Hatteras

A. ZTS Measurements and Interpolated Wave Rays

Using the ZTS technique, measurements were made of both wavelength and direction at the 140 grid locations shown in Figure 8. These measurements are plotted in Figure 29 as vectors proportional in length to measured wavelength, and oriented perpendicular to crests. The wave ray diagram in Figure 30 was constructed from these data by interpolating the direction field according to the exponential weighting algorithm of Equation (4), using a weighting factor of $F = 7.07$. For reference, wavelength vector data from CERC and ERIM are shown plotted at the same scale in Figures 31, 32, and 33.

There were four subimages on the data extraction grid at which conspicuous crossed seas were observed (discussed below). In the ray interpolation program, whenever one of these four points was encountered, the direction closest to the most recent direction was chosen. It should be noted that the SAR ray diagram of Figure 30 is subject to interpolation errors, and the subimage measurements in Figure 29 should be consulted when it is necessary to avoid interpolation error.

B. Wave Field Simulated by the VSWCM

1. VSWCM Runs Initialized with SAR Deep Water Measurements

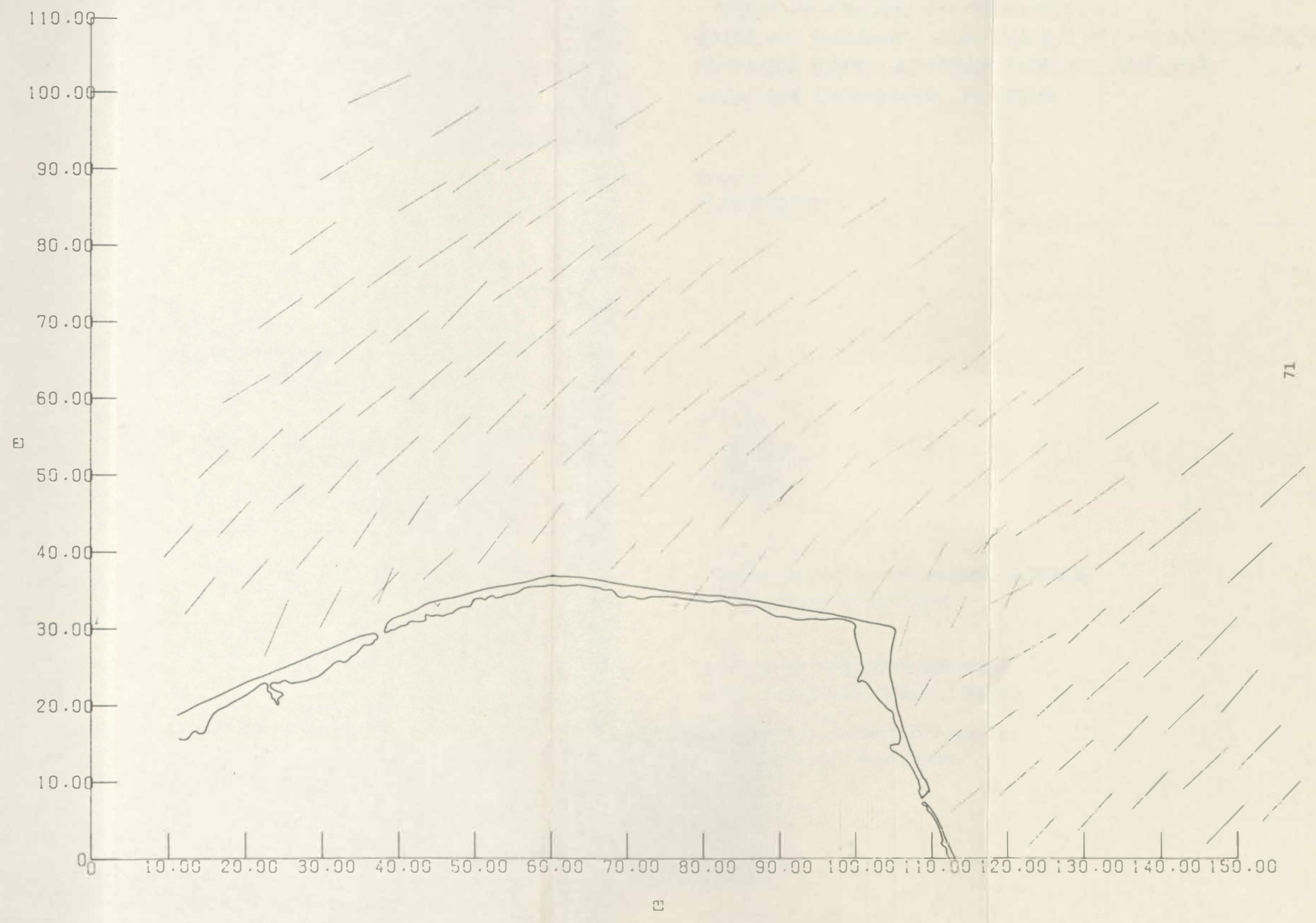
The wave field at Cape Hatteras on 3 September 1978 was simulated by running the VSWCM with initial wavelength and direction interpolated from SAR measurements in deep water. Each wave ray in the simulation had to be initiated with a particular measured vector (or an interpolated vector when the VSWCM initiation points fell between SAR measurement points on the previously described grid), due to the curvature in the deep water wave field. The result, a VSWCM prediction based on SAR-observed offshore conditions, is shown in Figure 34.

From the statistics of measurement errors, the most probable (+ and - one sigma) and inclusive (+ and - three sigma) ranges of SAR measurements of direction and wavelength were chosen and used to calculate bracketing values for initiating VSWCM runs. The chosen ranges in direction and wavelength were ± 2 degrees and 5 metres for 1 sigma, and ± 5 degrees and 20 metres for 3 sigma. A representative series of eight of the resulting diagrams is shown in Appendix 3.

The resulting simulations depict the wave fields attributable to different components of a polychromatic incident wave field with the given spectral range. However, an appropriate study of non-monochromaticity would require superpositions of sets of such simulations.

Figure 29. SAR wavelength "vectors" measured with ZTS for Cape Hatteras. The vector length is proportional to SAR-measured wavelength.

WAVELENGTH ARROWS.ZTS.CH



71

ZTS INTERPOLATED RAYS

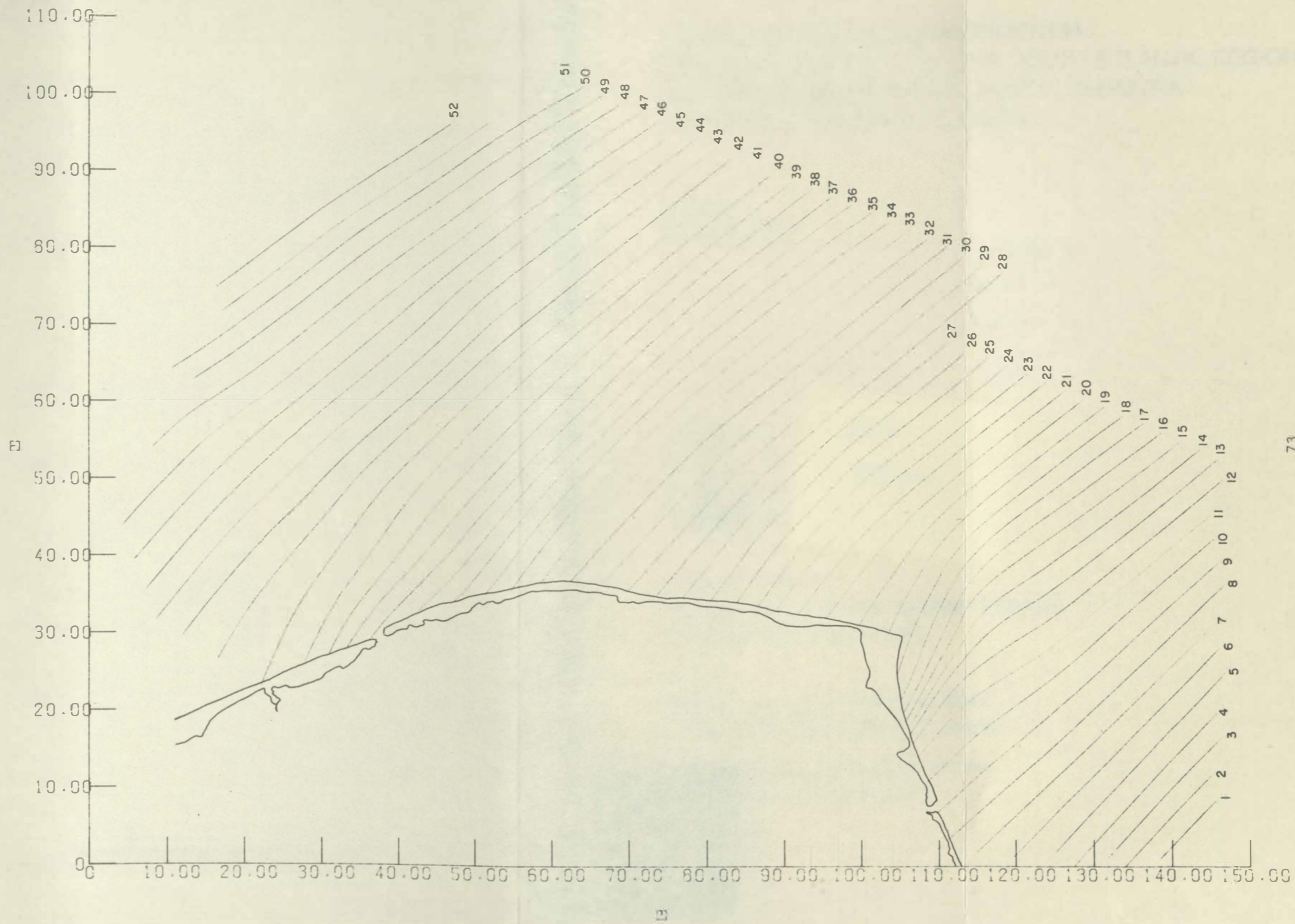


Figure 30. SAR wave ray diagram interpolated from measurements in Figure 29.

WAVELENGTH ARROWS.CERC. SG

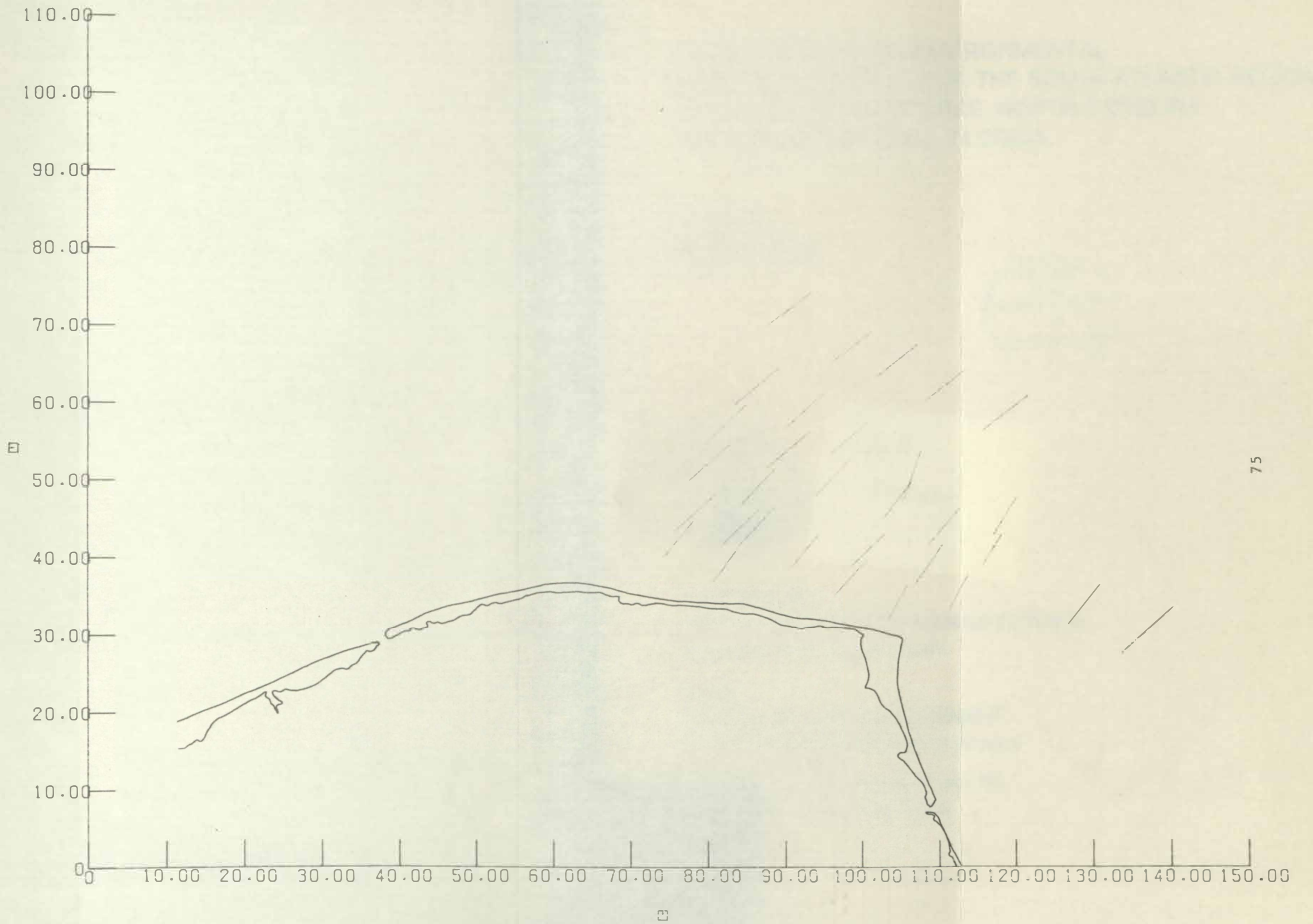


Figure 31. Wavelength vectors measured by CERC with OFTs.
11 mm diameter circles.

WAVELENGTH ARROWS, CERC, LG

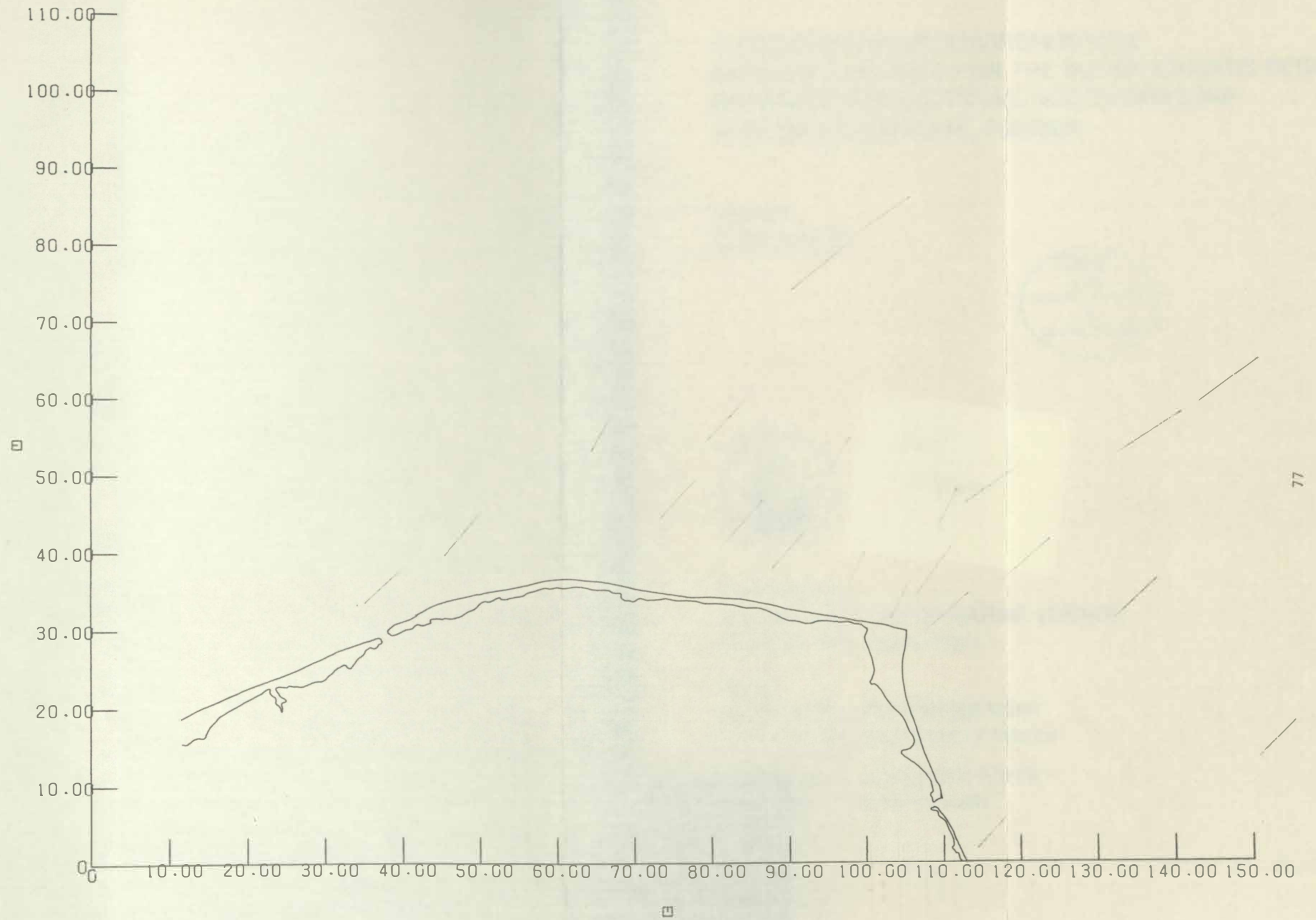


Figure 32. Wavelength vectors measured by CERC with OFTs.
38 mm diameter circles.

WAVELENGTH ARROWS.ERIM

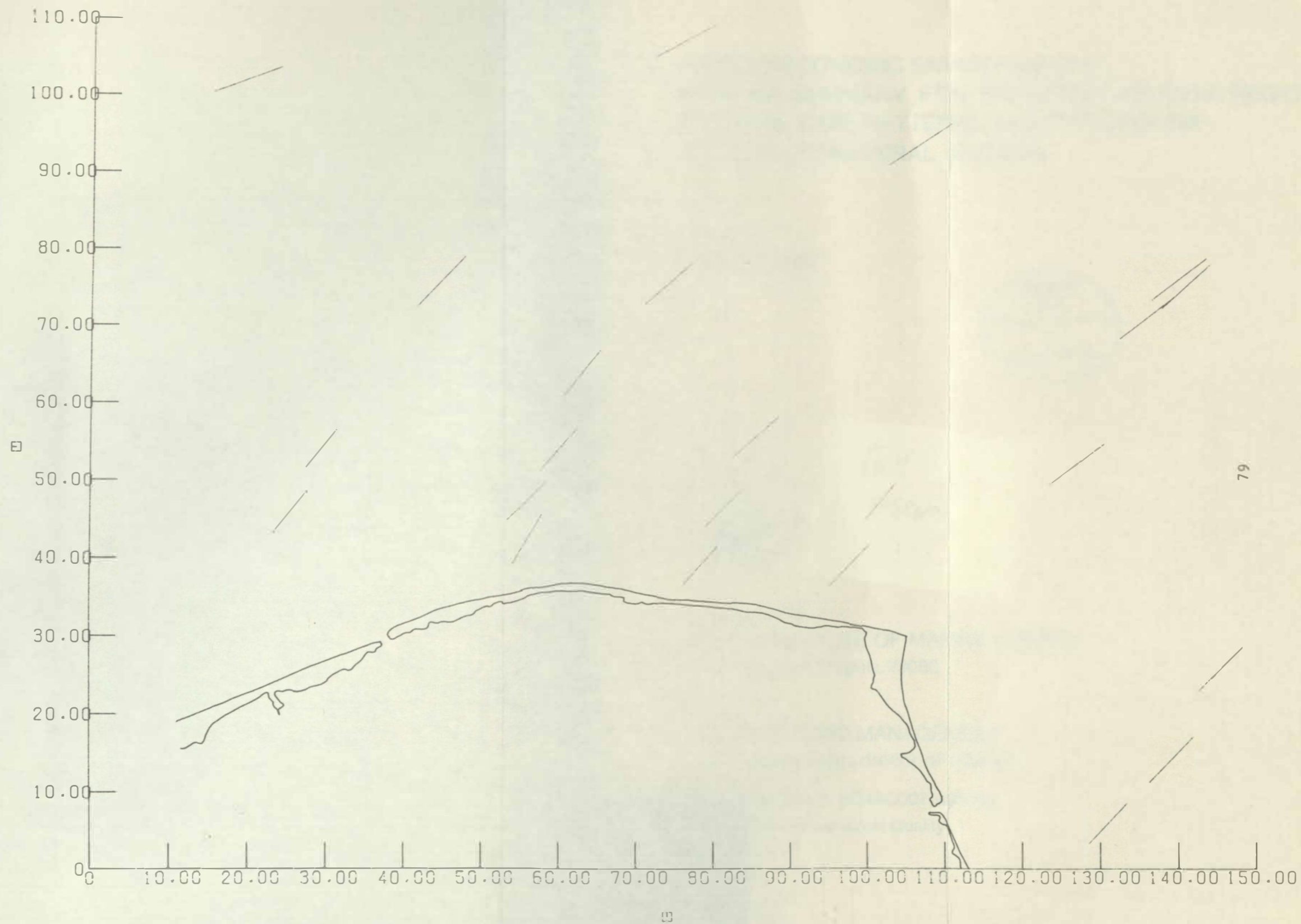


Figure 33. Wavelength vectors measured by ERIM with OFTs.
5 mm squares.

VSWCM WAVE RAY PLOT FOR CAPE HATTERAS

TIDE 1.8

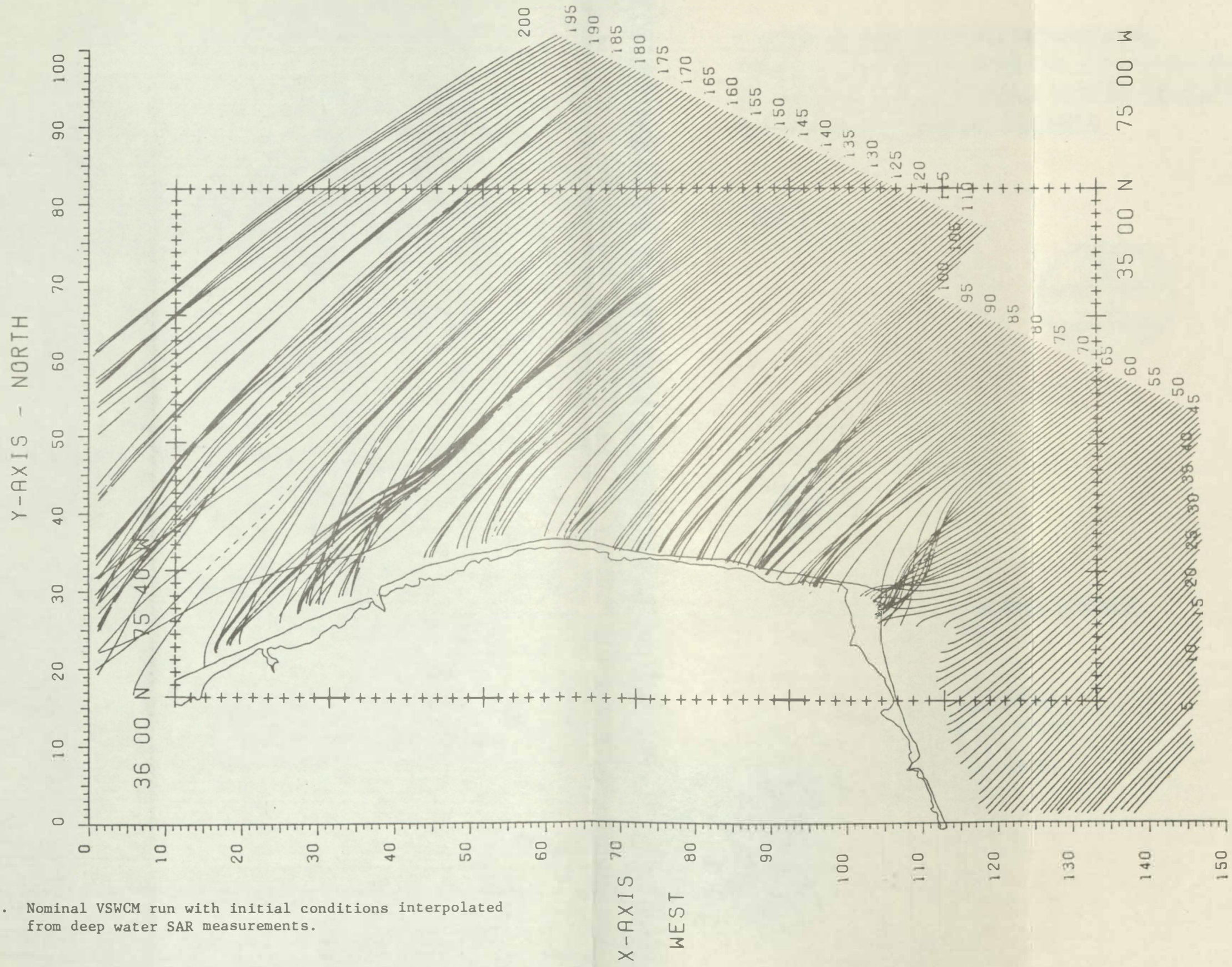


Figure 34. Nominal VSWCM run with initial conditions interpolated from deep water SAR measurements.

C. Comparison of SAR Observed Field with VSWCM Simulated Field

1. Superposed SAR Vectors and VSWCM Rays

The first comparison to be discussed is made between unsmoothed SAR (point) data and VSWCM rays. The SAR data are wavelength vectors from Figure 29, and the VSWCM rays, shown in Figure 34, are those produced using initial conditions interpolated from deep water SAR stations. This particular VSWCM run, because of its large number of rays, provides a detailed view of the predicted field. For the SAR data, the wavelength vector plot includes no interpolation error and is therefore preferred over the SAR interpolated ray diagram for the comparison. The vector plot is least likely to yield misleading interpretations, and the SAR ray diagram can subsequently be used as a supplementary map showing probable SAR wave ray tracks over the entire field.

To facilitate comparison, the area has been divided into six zones, as shown in Figure 35, numbered from south to north. Also, in Figure 36, the SAR vectors of Figure 29 are superimposed on the VSWCM ray field of Figure 34.

Zone I

Zone I is located in northern Raleigh Bay, a gently sloping and relatively uniform topographic area of the continental shelf. Measured wave directions correspond to VSWCM predictions easily within a few degrees, and rays are nearly straight. There are small discrepancies in which VSWCM rays refract southward more than SAR vectors.

Zone II

Zone II, located at the Cape, and including Diamond Shoals, gently slopes downward in the seaward direction out to a distance of 20 km (at the 60 foot isobath) where it drops off sharply. In deep water portions of this zone, beyond the 108 foot isobath, agreement between measurements and the model is very high, and directional spectra are unimodal at generally 320 degrees.

In contrast, over the shallower regions inside the 108 foot isobath, there are three ZTS grid stations with bimodal SAR wave spectra. The bimodal spectra can be seen in the original SAR image and associated OFTs. One component in these three spectra is at roughly 320 degrees, and is matched by the VSWCM predicted field. The other component is at roughly 295 degrees, but is not matched by the VSWCM at these stations. The validity of the 295 degree component is confirmed by limited CERC and ERIM data from nearby locations, and by VIMS OFTs from some of the same nearby locations.

Five additional VIMS ZTS grid stations further inshore in Zone II have unimodal directions at the same 295 degrees. Wave rays of 295 degrees are predicted by the VSWCM at four of these five inshore stations. In fact, the agreement is striking directly over Diamond Shoals, and one station is at 10 foot depth. The vectors from the grid

Figure 35. Cape Hatteras area divided into zones to facilitate analysis.

VSWCM WAVE RAY PLOT FOR CAPE HATTERAS

TIDE 1.8

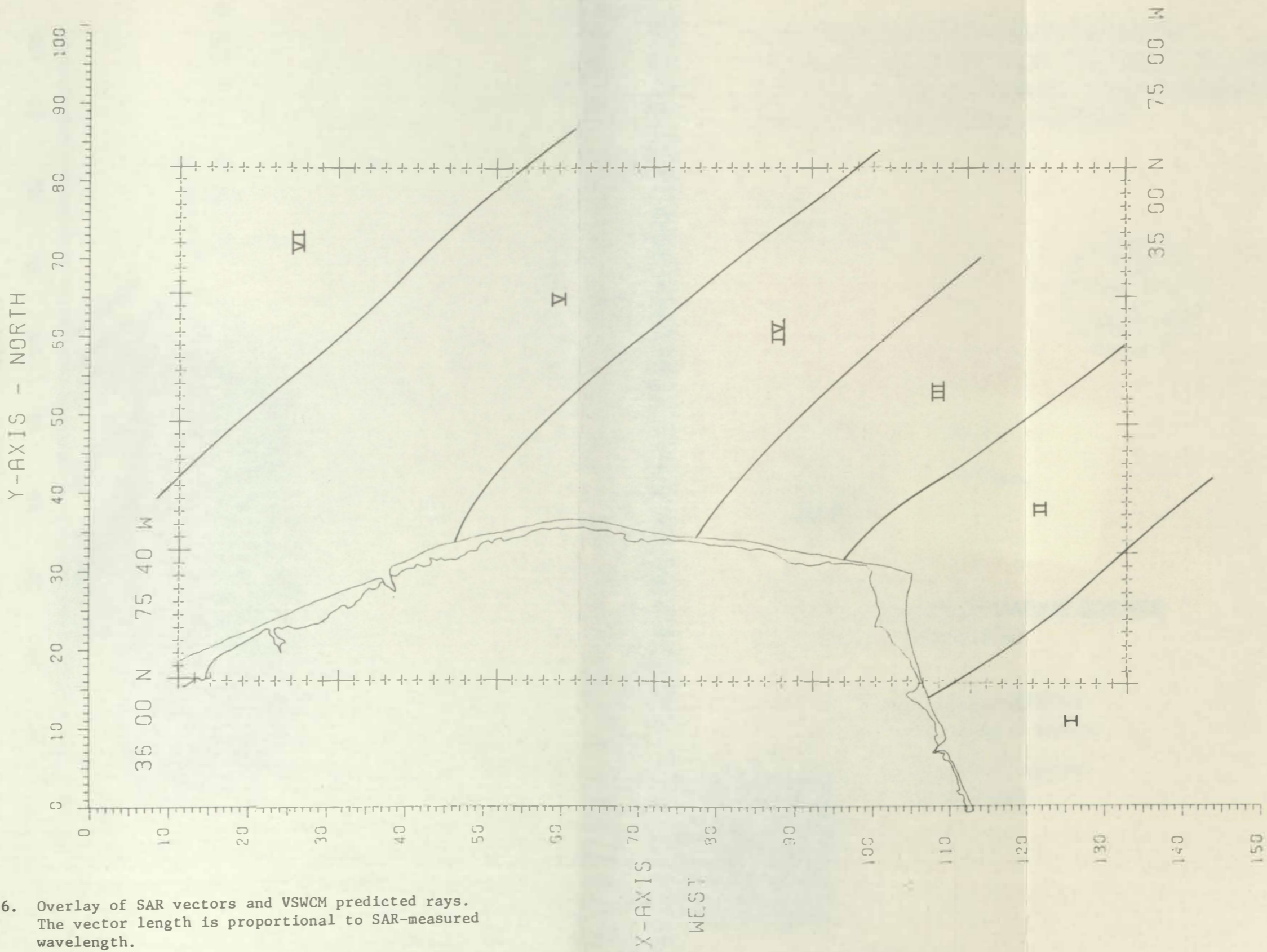
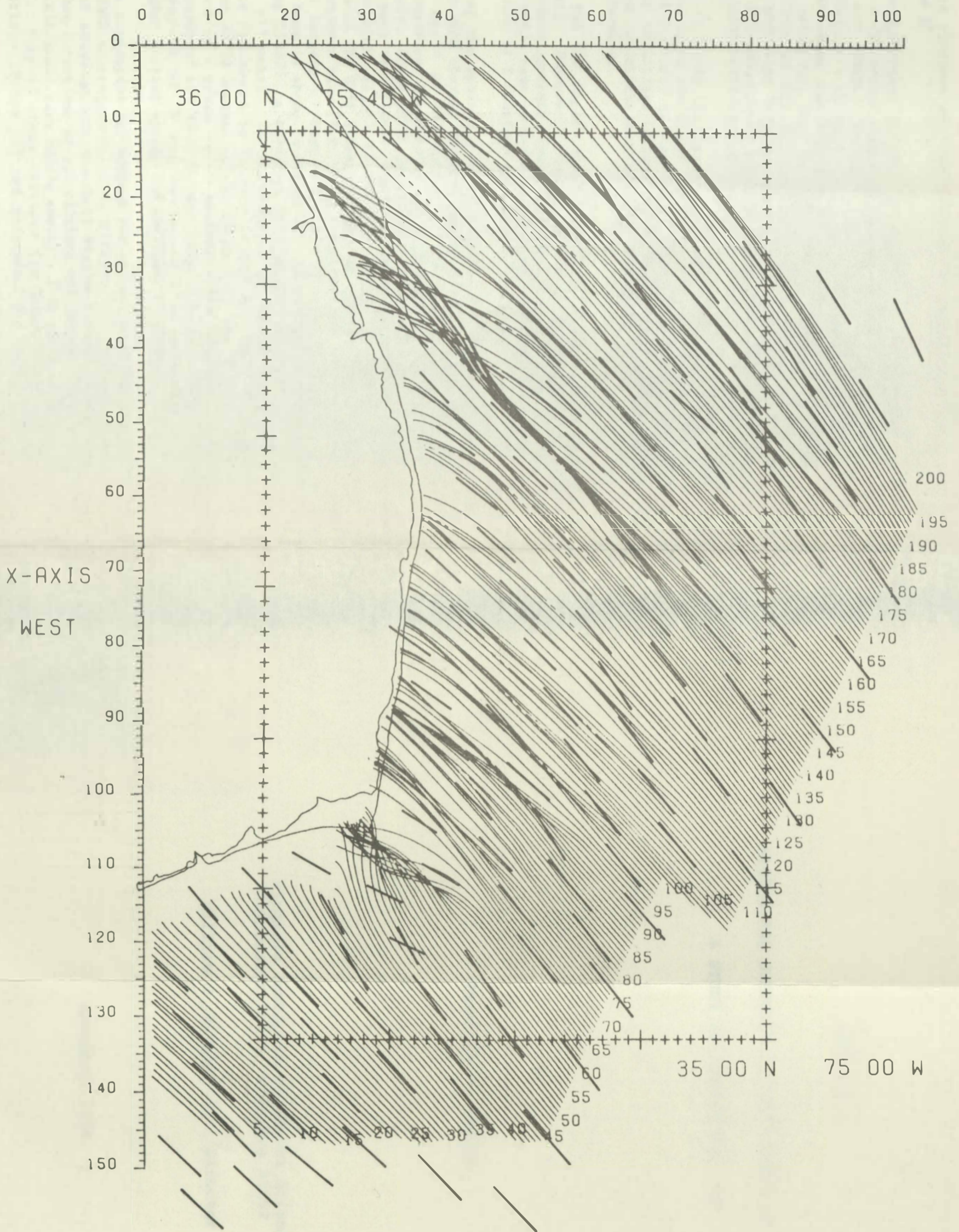


Figure 36. Overlay of SAR vectors and VSWCM predicted rays. The vector length is proportional to SAR-measured wavelength.

VSWCM WAVE RAY PLOT FOR CAPE HATTERAS

TIDE 1.8

Y-AXIS - NORTH



stations and extra stations where the 295 degrees component is present are shown in Figure 37.

Despite the agreement between the VSWCM and the SAR data at inshore locations, a 295 degree component is present offshore which is not predicted by the VSWCM. The question arises as to the source of this component. There are no rays of a similar orientation further offshore. The SAR image and OFTs for stations further offshore were visually inspected carefully; they show only unimodal spectra. If there are bimodal spectra at the offshore stations which have escaped detection visually and using 5-mm aperture OFTs from VIMS, then they should appear in the occasional 31-mm aperture OFTs from CERC, but (according to tabulated data) they do not.

The region is along the boundary between separate subswaths produced by JPL, and there are image photo-density variations across each subswath and from one to the next. These density variations introduce artificial variations in wave visibility. However, it is not believed that such variations have obscured any bimodal spectra in the region under consideration.

Therefore, the 295 degree waves must be produced by refraction from a local source. However, there is no feature of the charted bathymetry which would generate them. If an uncharted bathymetric rise is responsible, it would have to be possibly 10 km in diameter, to have produced parallel rays at 3 stations in a line 15 km long.

Refraction of the appropriate magnitude could be produced by current shear. In HCMM thermal infrared images of this area (Figure 3) on August 24 and again on September 9 (the Seasat pass was on September 3), the northwest boundary of the Gulf Stream appears to skirt the edge of the shelf. Other HCMM images closer to September 3 were cloud-covered or poor in quality. Figure 38 shows the position of the thermal boundaries with respect to the Cape. The locations are in general agreement with the Gulf Stream boundary at the 100 metre isobath on Ocean Frontal Analysis maps (U.S. Naval Oceanographic Office) based on NOAA-5 VHRR-IR imagery of August 25, 27, 31, and September 5. A composite of these maps is shown in Figure 39. According to equations derived by Johnson (1947), a shearing Gulf Stream current of 1 m/sec acting on waves of 175 metres, if incident at 63 degrees (much more shallow angles are indicated by Figures 20 and 25), would produce a southerly deflection of 20 degrees as the waves left the Gulf Stream. The current speed of 1 m/sec is an assumed value, typical of the observed current speeds of the Gulf Stream (see Stommel, 1965). The calculated deflection of 20 degrees could also be produced by combinations of higher current speeds and shallower incidence angles.

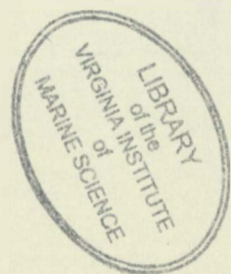
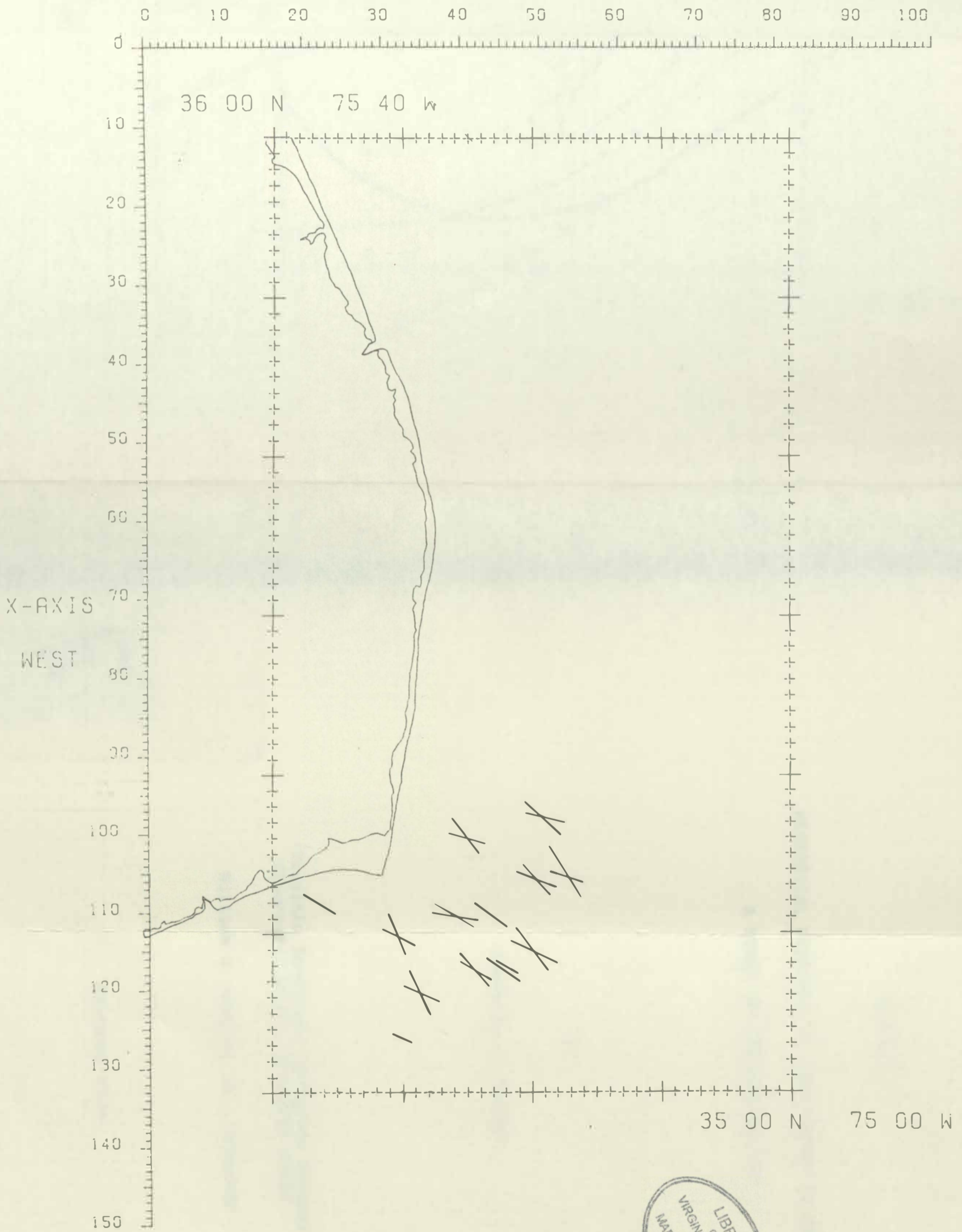
Despite the suggestive fit between the calculated deflection and the observed SAR-VSWCM discrepancy, it is difficult to reconcile the overall pattern of observations via Gulf Stream current shear. The first problem is that directions of all offshore SAR vectors (where the VSWCM runs were initiated) vary fairly smoothly from south to north as shown in Figure 40. Some of these stations (in Zones I and II) are eastward, while others (Zones III and following) are westward of the

Figure 37. Orthogonals from grid stations and extra stations where the 295 degree component is present.

VSWCM WAVE RAY PLOT FOR CAPE HATTERAS

TIDE 1.8

Y-AXIS - NORTH



VSWCM WAVE RAY PLOT FOR CAPE HATTERAS

TIDE 1.8

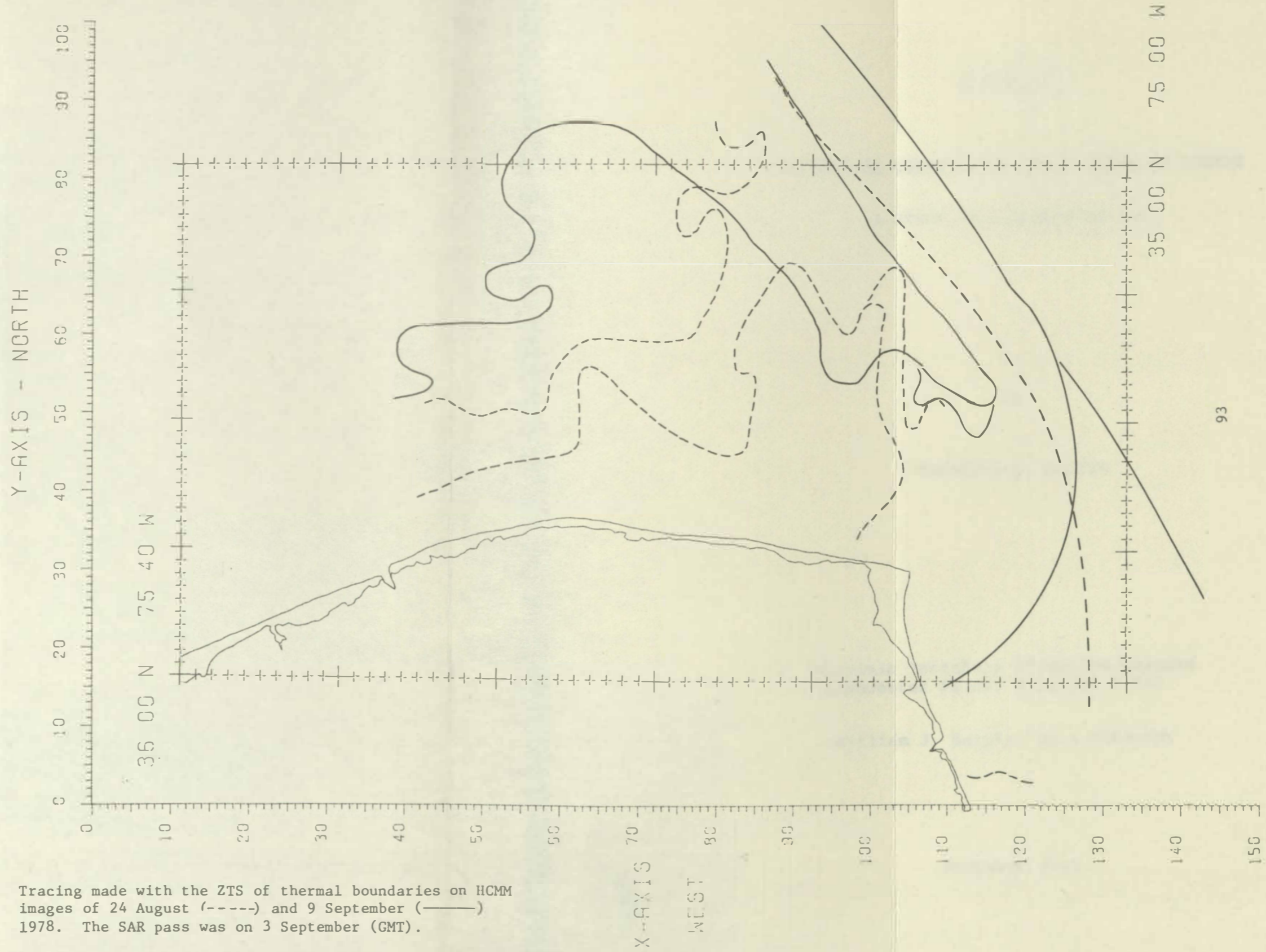


Figure 38. Tracing made with the ZTS of thermal boundaries on HCMM images of 24 August (-----) and 9 September (——) 1978. The SAR pass was on 3 September (GMT).

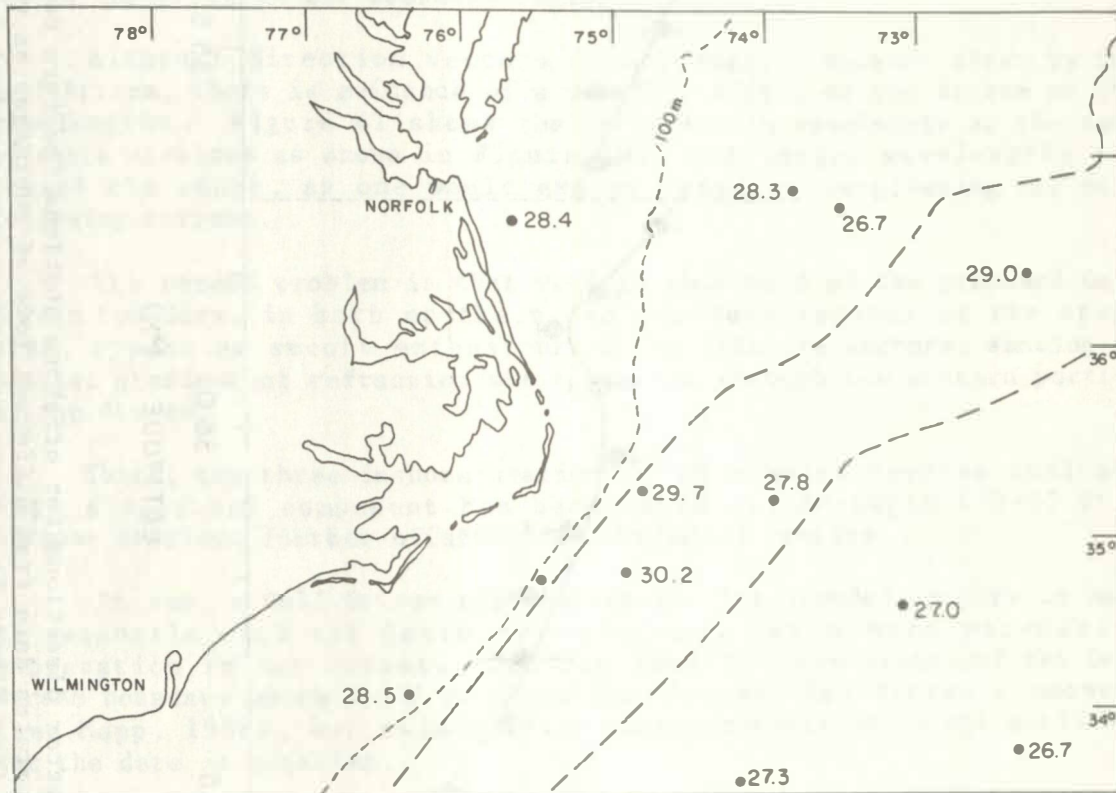


Figure 39. Ocean Frontal Analysis map for 5 September 1978. From U.S. Naval Oceanographic Office, based on NOAA-5 VHRR infrared imagery of 31 August and 5 September 1978. The boundaries of the Gulf Stream are shown as dashed lines. The SAR pass was on 3 September 1978. Temperatures (degrees Celsius) measured from ships.

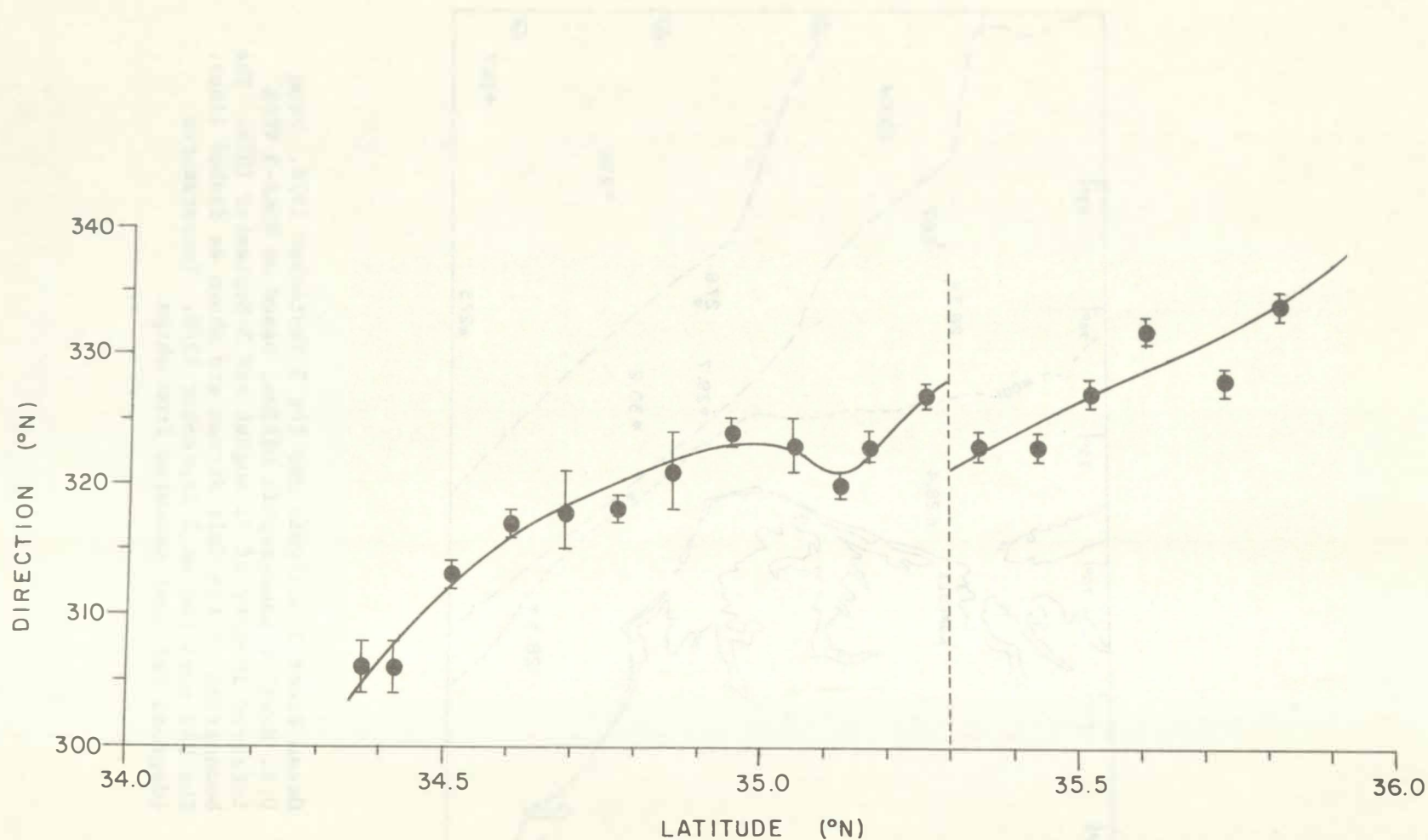


Figure 40. Variation of SAR vector directions for offshore stations (eastern boundary of Figure 8). The dotted line separates data from different rows of subimages on the seaward boundary of data extraction (see Figure 8). Error bars represent standard deviation of mean of raw data. The curve is hand-drawn.

HCMM thermal boundary. The Gulf Stream boundary, if located according to the HCMM thermal data, and stationary from September 3 to 9, should have caused refraction of vectors in the boundary region, particularly those in Zones I and II where the boundary crosses the ZTS measurement grid. This effect could be patchy depending on the velocity profile across the Stream. The Stream current usually consists of shearing layers (Stommel, 1965), while the thermal gradient is often quite sharp (Pickett, 1969). The only suggestion of current shear in Figure 40 is in the noisier direction data found north of latitude 35 degrees; this is contrary to the expectation that noisier data should be found as well toward the south in the boundary region.

Although direction vectors do not suggest current shear by the Gulf Stream, there is evidence of a possible effect of the Stream on the wavelengths. Figure 41 shows the variation in wavelength at the same offshore stations as shown in Figure 40. The longer wavelengths are toward the south, as one would expect based on lengthening due to a following current.

The second problem is that vectors shoreward of the presumed Gulf Stream boundary, in both northern and southern regions of the study area, appear as smooth extensions of the offshore vectors, showing no spatial gradient of refraction where passing through the western portion of the Stream.

Third, the three inshore stations with bimodal spectra indicate that a spectral component has been added at mid-depth (50-85 ft), because stations further offshore have unimodal spectra.

In sum, a Gulf Stream explanation for the bimodal spectra is hard to reconcile with all features observed, but a more persuasive explanation is not extant. One can imagine convolutions of the Gulf Stream boundary which would generate the observed 295 degree component (see Mapp, 1982), but evidence for such convolutions is not available for the date in question.

Just north of the Cape, wave energy is predicted by the VSWCM to be low, due to southerly refraction and a caustic along the northern boundary of Diamond Shoals. However, waves were easily detected on the SAR image in this region.

Zone III

Zone III is characterized by a hilly shelf edge, causing several SAR rays to bend abruptly in passing nearby. The VSWCM ray diagram contains several caustics, where grazing rays cross at small angles of about 5 degrees. At one station, a crossed sea was detected on the SAR image near a caustic predicted by the model. At the other sites of predicted caustics, however, there were no corresponding crossed seas on the SAR image. Indeed, at several places the details present in VSWCM diagrams cannot be discerned in the available SAR image or measurements. These details include subtle curves in rays (gentle convergence and divergence), and crossed seas at small angles. With respect to wave

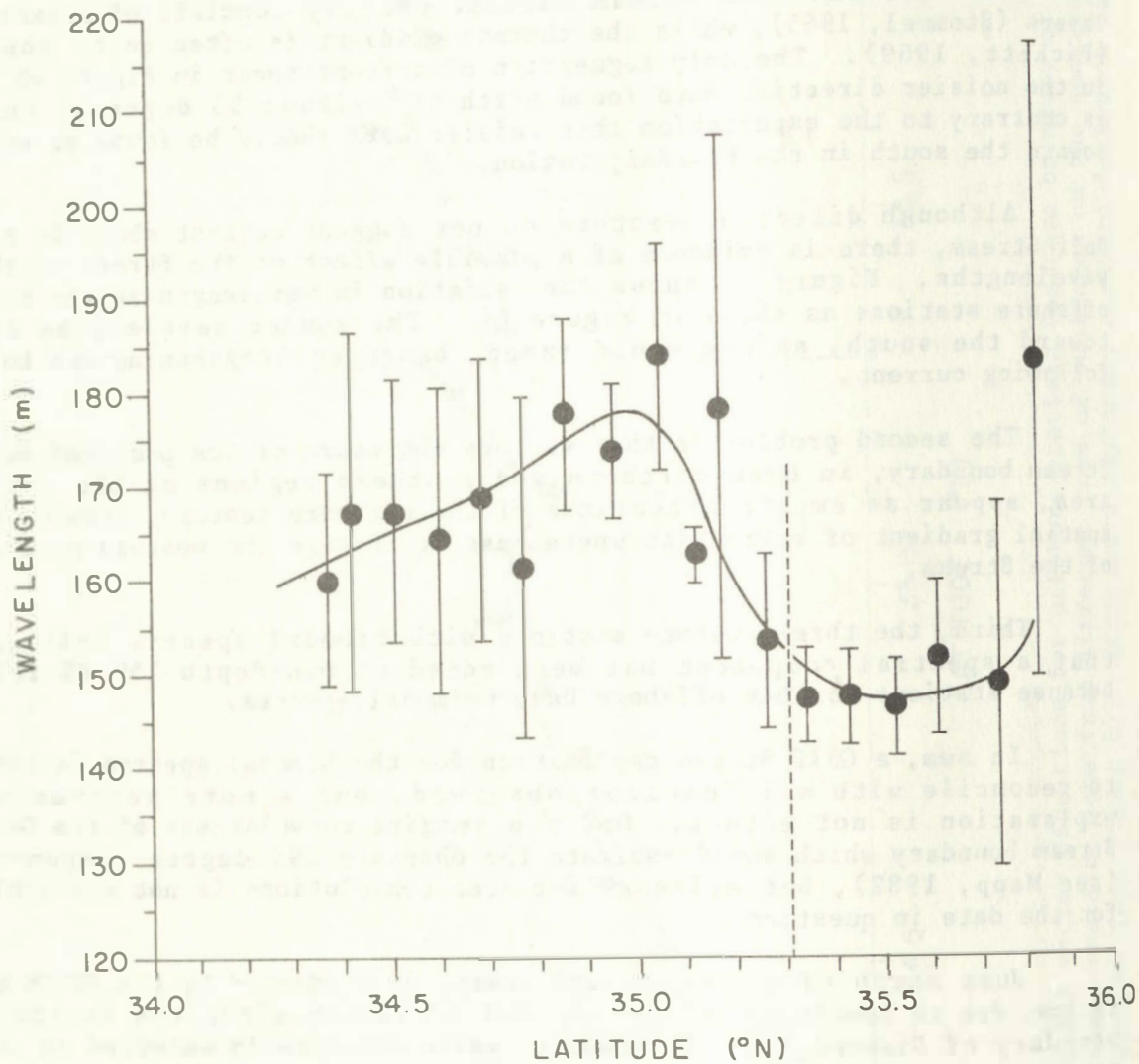


Figure 41. Variation of SAR vector wavelengths for offshore stations. See the legend of Figure 40.

directions in Zone III, the measured directions are within 5 degrees of predicted values.

Zone IV

Zone IV includes Wimble Shoals and areas seaward. Here the Continental Shelf begins to broaden and lose the hilly character of the shelf edge in Zone III. Near the shelf edge, there is a slight 5 degree angular bias northward of several VSWCM rays. The cause of this deviation may be inaccurate input data--a correction of +5 degrees for one SAR station would remove the deviation.

For the remaining 24 SAR vectors in Zone IV, 7 show a northerly deviation and 1 a southerly deviation from VSWCM predicted rays. Many of these deviations are the consequence of southerly deflections of predicted rays when they first encounter depths less than 100 feet. Slightly greater depths, or smaller wavelengths, near the shelf break would have improved the SAR-VSWCM match.

Zone V

In Zone V, there is again a slight discrepancy of about 5 degrees between model rays and SAR data near the shelf edge, but the polarity of the discrepancy is not consistent. The topography of this area is a mildly sloping outer shelf grading into the beginning of the ridge and swale pattern typical of the mid-Atlantic Bight. Further inshore is the region of Platt Shoals, and here the model predicts a major caustic region. Ten rays in the simulation of Figure 21 converge and cross a few kilometres seaward. The strength of convergence and divergence predicted by the model is not corroborated by the SAR vectors, which show only weak convergence. In fact, if the VSWCM rays did not converge here, the resulting pattern would agree well with the SAR data. It appears from the SAR grid measurements that the VSWCM simulation is inadequate here (but see section 2 below).

Zone VI

Zone VI is an area of intermediate depths and deep water, with a gently sloping outer shelf area gradually changing into ridge and swale topography. Both the modeled field and SAR "vectors" show slightly curved rays in this area, and with one exception the agreement between predicted rays and SAR "vectors" is within 5 degrees, slightly more than 2 sigma of error in direction measurements. However, 14 SAR vectors have a northerly deviation from predicted rays. Again, slightly greater depths or smaller wavelengths would have improved the match.

All Zones

Finally, the pattern of deviations between the SAR vectors and the VSWCM predictions was examined in its entirety. Deviations in direction were calculated for all of the 140 ZTS stations, and displayed in the histogram of Figure 42. A machine-drawn contour map of these deviations is shown in Figure 43. The one large deviation derives from the 295 degree wave train at the Cape itself. All remaining ± 10 degree

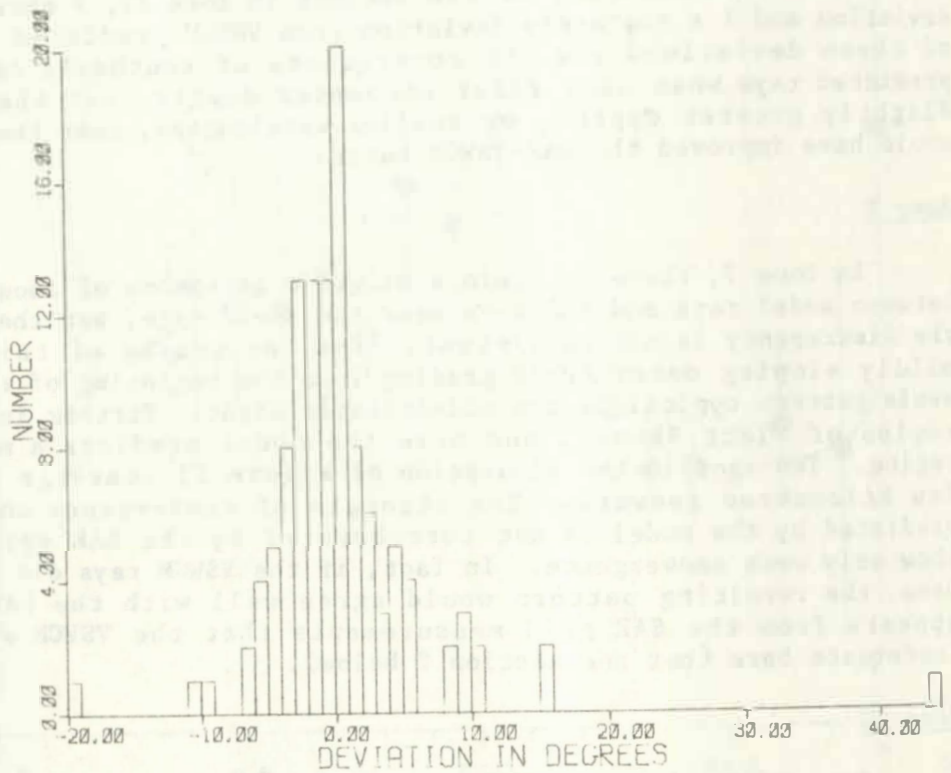


Figure 42. Histogram of direction deviations (SAR vs. VSWCM) for the area of study.



SEASAT DELDOR DATA

PLOT NO. 1

DATE 01/26/82

TIME 11:16:04

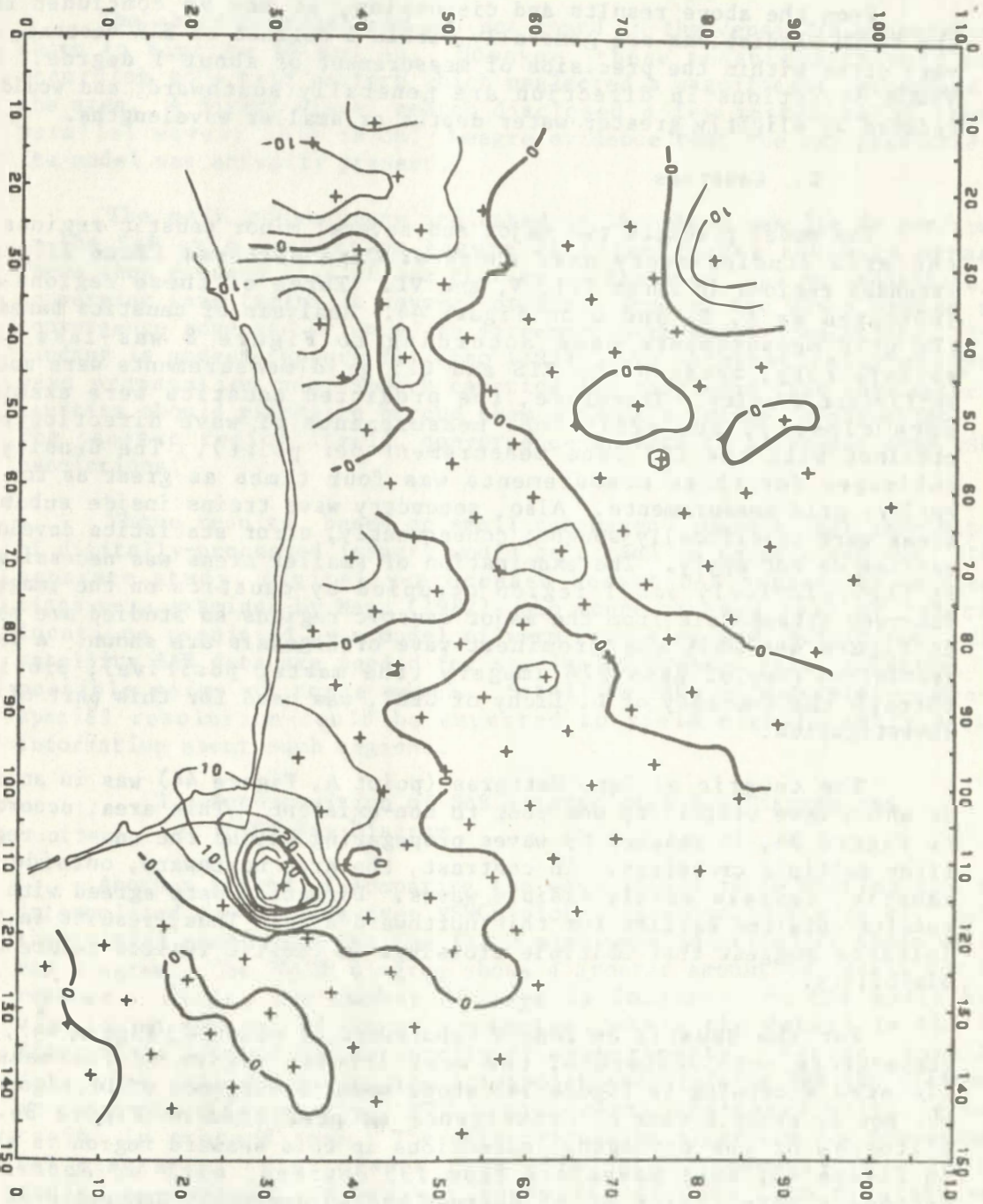


Figure 43. Contour map of direction deviations (SAR vs. VSWCM) for the area of study.

contours, except for one, are located around the shoremost stations where measurements are difficult, bathymetry is the least stable, and refraction is maximal. The offshore station toward the north showing a deviation larger than 10 degrees was obtained from a portion of imagery showing much less contrast than elsewhere. The deviation may be a consequence of poor wave visibility.

Nearly half (46%) of the deviations are within ± 2 degrees.

From the above results and discussion, it may be concluded that the VSWCM predictions are generally within 5 degrees of SAR vectors, and very often within the precision of measurement of about 1 degree. The VSWCM deviations in direction are generally southward, and would be reduced by slightly greater water depths or smaller wavelengths.

2. Caustics

The model predicts two major and several minor caustic regions in the area studied--very near shore at Cape Hatteras (Zone II), and extended regions in Zones III, V, and VI. Three of these regions are indicated as A, B, and C on Figure 44. Analysis of caustics based on the grid measurements made according to Figure 8 was less than satisfactory, because the ZTS and OFT grid measurements were not of sufficient density. Therefore, the predicted caustics were examined more closely, and additional measurements of wave direction were obtained with the ZTS (one measurement per point). The density of subimages for these measurements was four times as great as for the earlier grid measurements. Also, secondary wave trains inside subimage areas were specifically sought; consequently, error statistics developed earlier do not apply. The examination of smaller areas was necessitated by the relatively small region occupied by caustics on the imagery. Observed orthogonals from the major caustic regions so studied are shown in Figure 44--only the prominent wave orthogonals are shown. A finer resolution copy of pass 974 imagery (the master positive), provided through the courtesy of D. Lichy of CERC, was used for this part of the investigation.

The caustic at Cape Hatteras (point A, Figure 44) was in an area in which wave visibility was poor to non-existent. This area, according to Figure 34, is reached by waves propagating beyond the caustic region after multiple crossings. In contrast, the area northward, outside the caustic, reveals easily visible waves. Direction data agreed with the results obtained earlier for this northward area. Thus, results in this instance suggest that multiple crossings in caustic regions reduce wave visibility.

For the caustic in Zone V (shoreward of point C, Figure 44), the convergence zone seaward of the most intense region of the caustic (located according to Figure 34) shows some convergence of orthogonals, but not as sharp a cone of convergence as predicted on Figure 34. A histogram of the orthogonal directions in this seaward region is shown in Figure 45; most waves are from 135 degrees, with evidence for secondary wave trains at 95 degrees and 45 degrees. Shoreward of the intense region, Figure 34 indicates that there should be crossing wave

trains from three directions, including one ray aligned parallel to shore. Figure 44 indicates that fragments from two of the three directions were found. In particular, well-defined convergence is evident. A histogram of the orthogonals in this region is presented in Figure 46, and it shows some indication of seas which are more confused than further offshore. At 135 degrees, there is a peak which is broader than that seen offshore in Figure 45, the probable result of convergence.

The shore-parallel ray was not found in the dense ZTS measurements shown in Figures 44 and 46. However, these measurements were made according to a grid pattern which neglected a significant percentage of the area. A direct visual search disclosed a few instances of shore-parallel waves; this is only meagre evidence that the ray predicted by the model was actually present.

The main convergence indicated in the above results is confirmed in the SAR grid vectors on Figure 21 (from larger subimage areas). These show crossed seas at one station in the area, and an indication of converging wave trains at several others. Some of the waves beyond the convergence zone are oriented in agreement with model predictions. This finding is modest support for Chao (1971), who mathematically analyzed wave propagation near smooth caustics and concluded that rays entering caustics should propagate beyond them without a change in direction. In the caustic region itself, convergence appears to be weaker than VSWCM predictions.

These results, based on small subimages, suggest that examination of digitally-processed imagery would be useful in caustic regions. In a separate study, digitally-processed Seasat SAR imagery of warm core rings were examined by Mapp (1982), who found crossed seas at relative locations predicted by a model of warm core ring wave refraction. More satellite SAR data are needed for studies of crossed seas, caustics, and possible sites of rogue waves. Satellite SARs of moderately-improved spatial resolution could be expected to yield significantly better information about such regions.

3. Superposition of SAR Interpolated Ray Diagram and VSWCM Ray Diagram

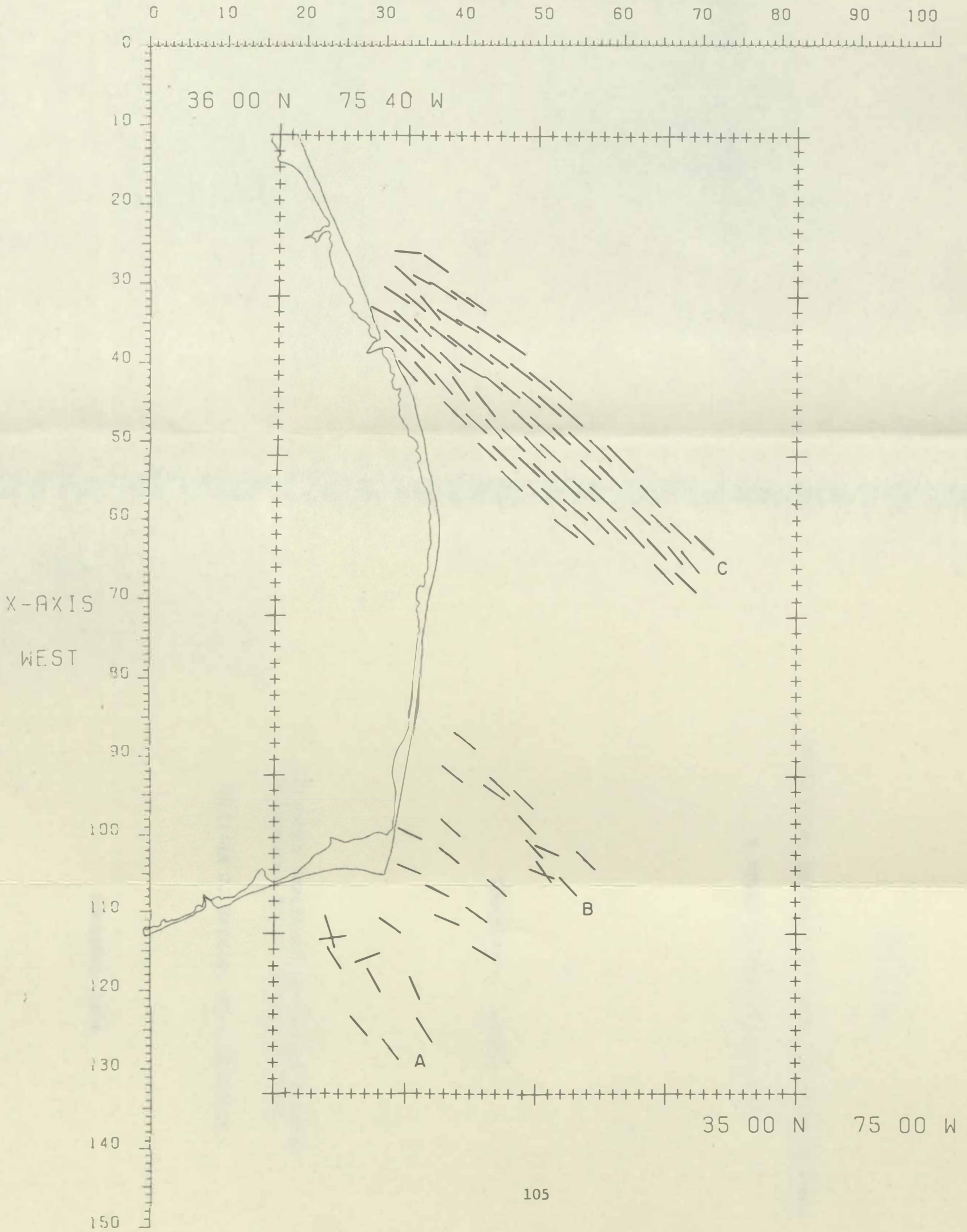
Another method of comparing the wave fields is to overlay the SAR interpolated ray diagram over VSWCM plots, as shown in Figure 47. Here, the initial conditions for the VSWCM plot were identical to those of the SAR diagram. The VSWCM diagram shows a greater amount of detail for two reasons. First, the number of rays is increased in the model by a simple change of an input parameter, while the detail in the SAR diagrams is limited by the density of measurements. Second, some SAR data were excluded during the interpolations yielding SAR ray diagrams, in cases where the original ZTS measurements indicated multiple wave trains in crossed seas. The data processing algorithm for producing a SAR diagram of interpolated rays eliminated secondary rays in the following manner. To prevent inclusion of data from separate wave trains in the calculation of the mean vector from a set of four (sometimes more) replicate ZTS measurements, the minimum number of

Figure 44. Orthogonals from additional ZTS measurements in the region of caustics predicted by the VSWCM. Secondary orthogonals from each subimage not plotted.

VSWCM WAVE RAY PLOT FOR CAPE HATTERAS

TIDE 1.8

Y-AXIS - NORTH



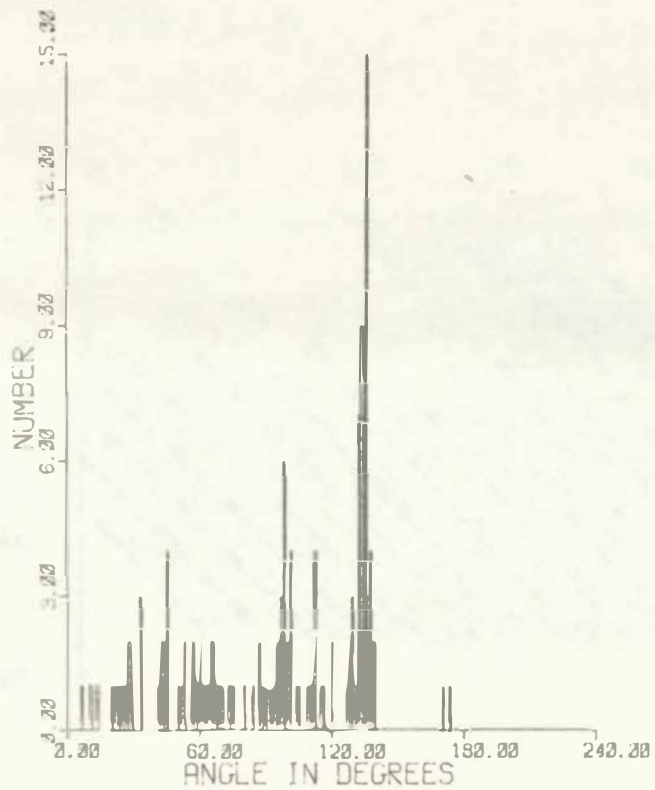


Figure 45. Histogram of orthogonals seaward of the predicted caustic C in Figure 44.

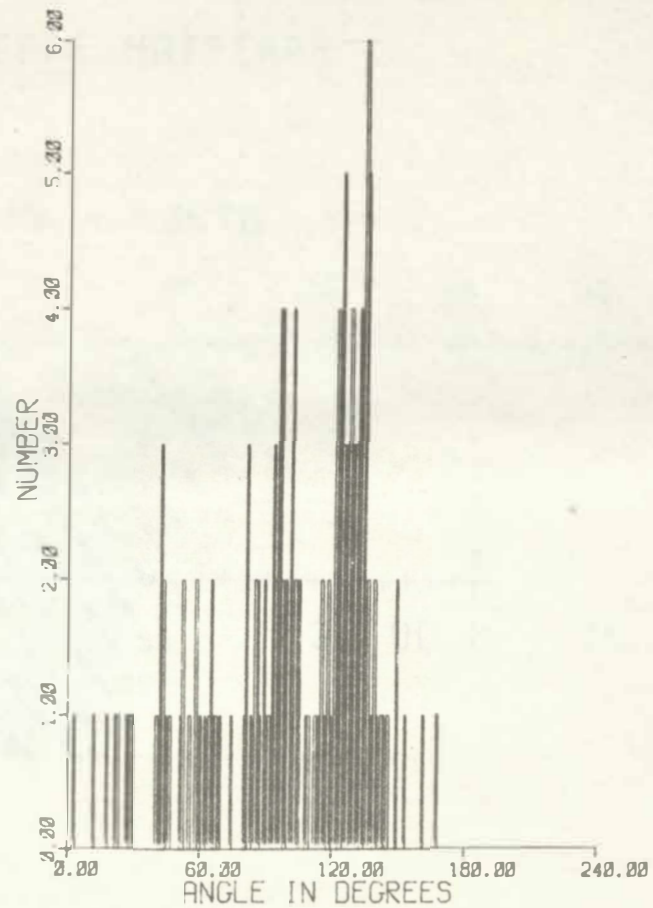


Figure 46. Histogram of orthogonals shoreward of the predicted caustic C in Figure 44.

Figure 47. Overlay of VSWCM predicted rays onto SAR interpolated rays.



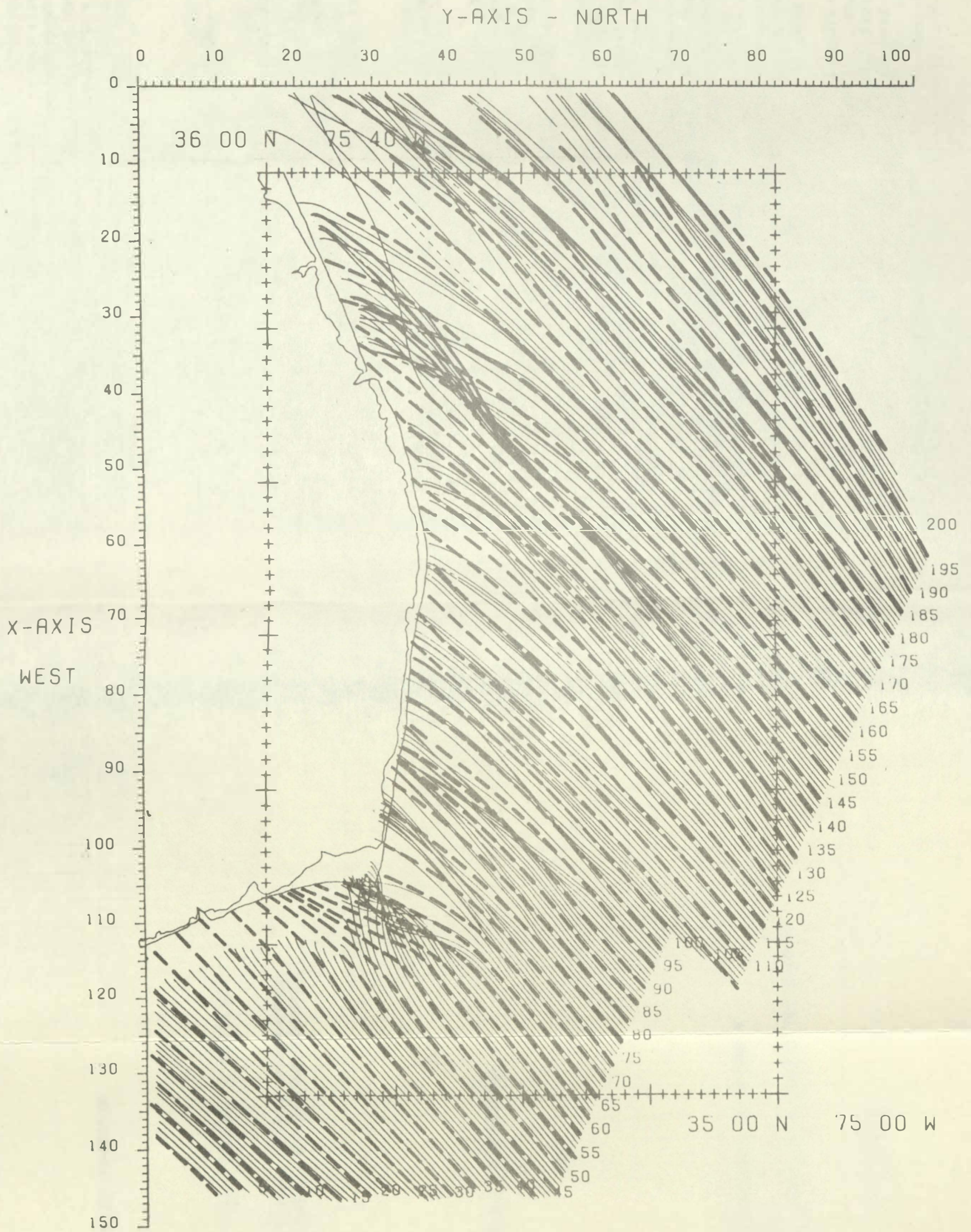
Figure 47. Overlay of VSWCM predicted rays onto SAR interpolated rays.

Figure 48. Overlay of VSWCM predicted rays onto SAR interpolated rays.



VSWCM WAVE RAY PLOT FOR CAPE HATTERAS

TIDE 1.8



measurements considered acceptable was set at two, and no outlier with a direction deviant by greater than eight degrees was included. This feature of the algorithm preserved accuracy by preventing averaging of data from separate wave trains, but eliminated the possibility of mapping separate rays, when directions differed by less than eight degrees. Thus, the mapping of some crossed seas is prohibited by the interpolation algorithm.

In the VSWCM plots, most refraction is observed, naturally, in the shallower areas with depths less than 30 metres. The model predicts complex crossed seas at Diamond and Platt Shoals. Using 5-mm circles and the 7 km grid pattern developed for SAR measurements, it was impossible to extract a great amount of detail near the shoreline and in these shoal regions. In general, the wave visibility declined markedly over both shoals, making difficult the resolution of wave trains. In other nearshore areas, there were often crossed seas observed in visual inspection of the imagery, which failed to be extracted by the ZTS technique in which the area surrounding the small-size circular subimages was masked. This masking prevented viewer bias involving surrounding wave patterns, but also eliminated helpful clues in discerning marginally visible wave trains in the sampling region.

Another reason for potential discrepancies nearshore is smearing due to computational interpolation--the field nearshore is experiencing the greatest refraction and is not regular enough for interpolation to produce accurate results. A third level of density in the sampling grid nearshore might prove beneficial.

Thus, in general, the level of detail visible on model ray diagrams exceeds that in SAR ray diagrams. The areas offshore are more amenable to analysis than inshore areas, but offshore there is less refraction.

Despite these drawbacks, the inspection of SAR ray diagrams has revealed the following: generally, the deviations of VSWCM output from the SAR diagram are southerly, as expected from interpretations of the SAR vector plot discussed earlier. Slightly better agreement would result from increases in depth or decreases in wavelength in the model to reduce the overall amount of refraction. Note that the changes required are small.

Second, observed patterns of gentle convergence and divergence generally agree with predicted locations of crossed seas and caustic regions.

Third, it is evident there are several areas near the shelf edge where there are slight (5 degree) discrepancies between the model and SAR data. To see if these may have been due to inappropriate initial conditions, a search was made for the best-fitting VSWCM rays from all the VSWCM runs for bracketing conditions. Figure 48 (see also Table 10) reveals a regular pattern of rays with better fits to the SAR data whose initial conditions have small angular offsets from the SAR measured initial conditions. The angular offsets (disregarding wavelength changes) as a function of initial position show a smooth variation.

...the ... of the ...

...the ... of the ...

...the ... of the ...

Figure 48. Collation of best-fit rays from all VSWCM runs.

...the ... of the ...

...the ... of the ...

...the ... of the ...

...the ... of the ...

VSWCM WAVE RAY PLOT FOR CAPE HATTERAS

TIDE 1.8

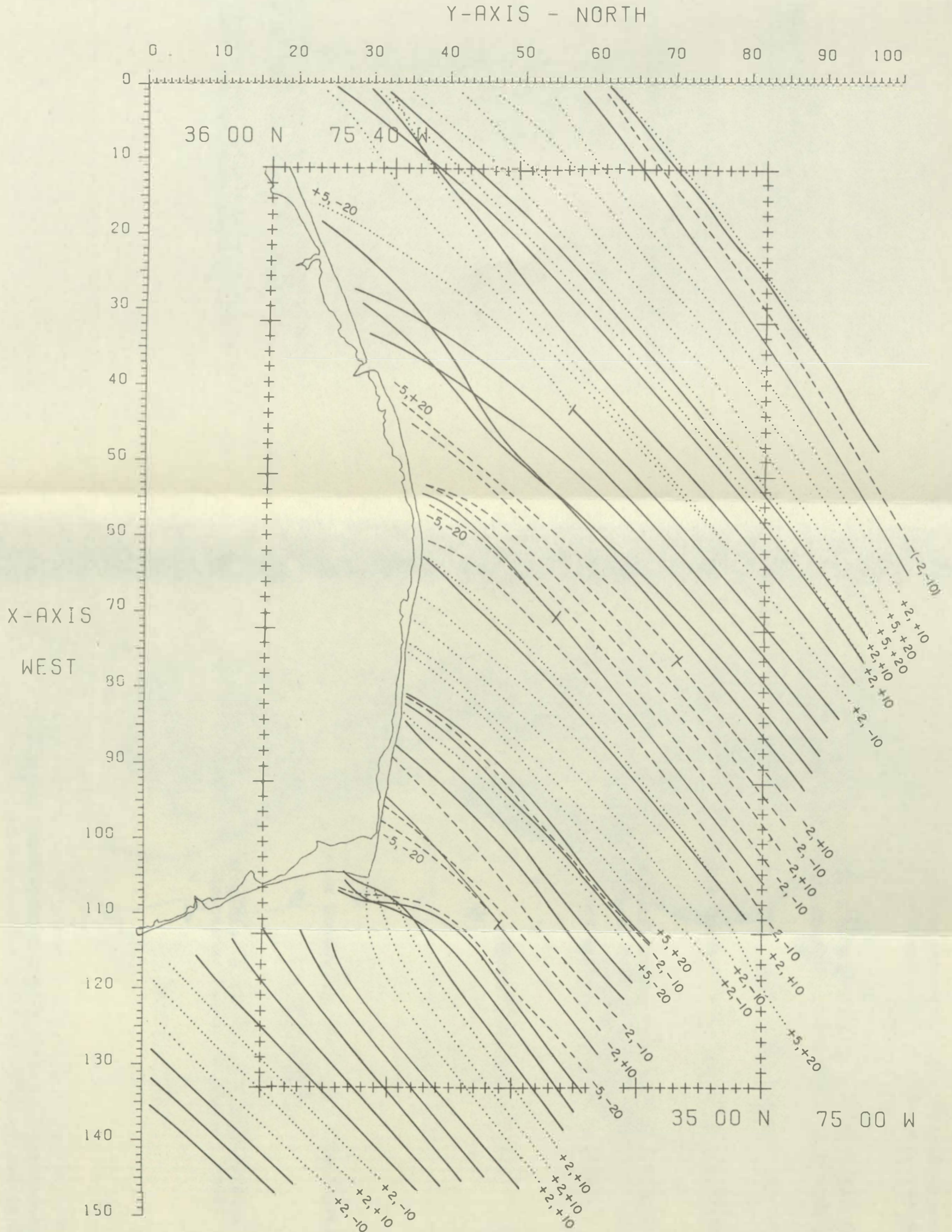


TABLE 10

Comparison of Best-fit VSWCM Runs for Ray Collinearity and Shoreline Ray Density.

Best-fit VSWCM Runs[#]

Shore Segment	Zone	Collinear Rays (Degrees, m) [#]	Shoreline Ray Density (Degrees, m) [#]
I	I	+2, -10 (3)*	
	II	+2, +10 (3)	+5, -20
		-5, -20 (1)	
II	III	-2, +10 (1)	-5, -20
		IV	
		+5, -20 (1)	
		-2, -10 (1)	
		+5, +20 (1)	
		+2, -10 (2)	
		+5, +20 (1)	
III	V	+2, +10 (1)	0, 0
		-2, -10 (2)	
		-2, -10 (1)	
		-2, +10 (1)	
		+2, -10 (1)	
		+2, +10 (2)	

[#]Changes needed in degrees and metres of direction and wavelength in nominal VSWCM run in order to produce best-fit run.

*Number of rays in parentheses given in order south to north. Zone VI omitted due to lack of overlap with shore segments.

This finding suggests that the SAR-measured initial conditions may have been distorted by shearing currents. The pattern of variations is too complex to be explained by a linear Gulf Stream boundary (see Mapp, 1982, and section C.1 above). However, Welch et al. (1981, see Appendix E) have suggested that the pattern of alternating positive and negative deviations in direction could be the result of tidal oscillations acting on the Gulf Stream.

Although the agreement between the model and SAR data increases with the use of rays from bracketing runs of the model, there are still areas of discrepancy not eliminated by selected changes in the initial ray directions, notably over Diamond Shoals and Platt Shoals, and in the hilly areas of Zone III.

4. Wavelength Versus Ray Distance Plots

Another measure of the goodness of fit between VSWCM predictions and SAR data is agreement between wavelength values. In the course of calculations for the SAR ray diagram, wavelength was interpolated at each incremental step using the same type of algorithm and weighting factor as for direction. Thirteen rays were then chosen from that VSWCM run which was based on initial conditions identical to those of the SAR rays. The rays selected were those most nearly collinear with SAR interpolated rays (within 5 km). Plots of predicted (VSWCM) wavelength, and interpolated values of SAR wavelength, were then constructed as a function of distance along rays. The resulting diagrams for the 13 rays are found in Appendix 4. On the SAR wavelength plots, error brackets of + and - 1 Sd bar (based on the original ZTS measurements at each point) were added to the plots at all locations where the interpolated rays passed within 2.5 km (5 mm on the SAR image) of a ZTS measurement point (the interval 2.5 km is necessary because the interpolated rays rarely crossed the actual points of ZTS measurements). Agreement between predicted and observed wavelengths along collinear rays was generally within one standard deviation of the mean of measurement.

In the comparison of these wavelength plots, for nearly all rays the agreement was within 15 metres until the VSWCM approached the shoreline, where the predicted value dropped sharply. Figure 49 shows the diagram of the wavelength values for one of the rays, ray # 18. For rays # 18 and 17 there was significant disagreement over Diamond Shoals. For rays # 46 and 45, there was an area near the shelf edge where the discrepancy was nearly 20 metres, but this was an area of poorer wave visibility on the SAR image (indicated by the wide error bars on ray # 45). Overall, the agreement is generally within the limits set by the error bars, indicating satisfactory wavelength simulation by the VSWCM over the area studied.

5. Shoreline Ray Density

Measurement of Shoreline Wave Energy

Another measure of agreement between SAR data and VSWCM predictions is comparison of wave energy at the shoreline. From either measured or computed wave-field energy spectra $S(f)$ as a function of

WAVELENGTH VS RAY DISTANCE

◇ = SAR OBSERVATIONS
* = MODEL PREDICTION
NRAY = 18

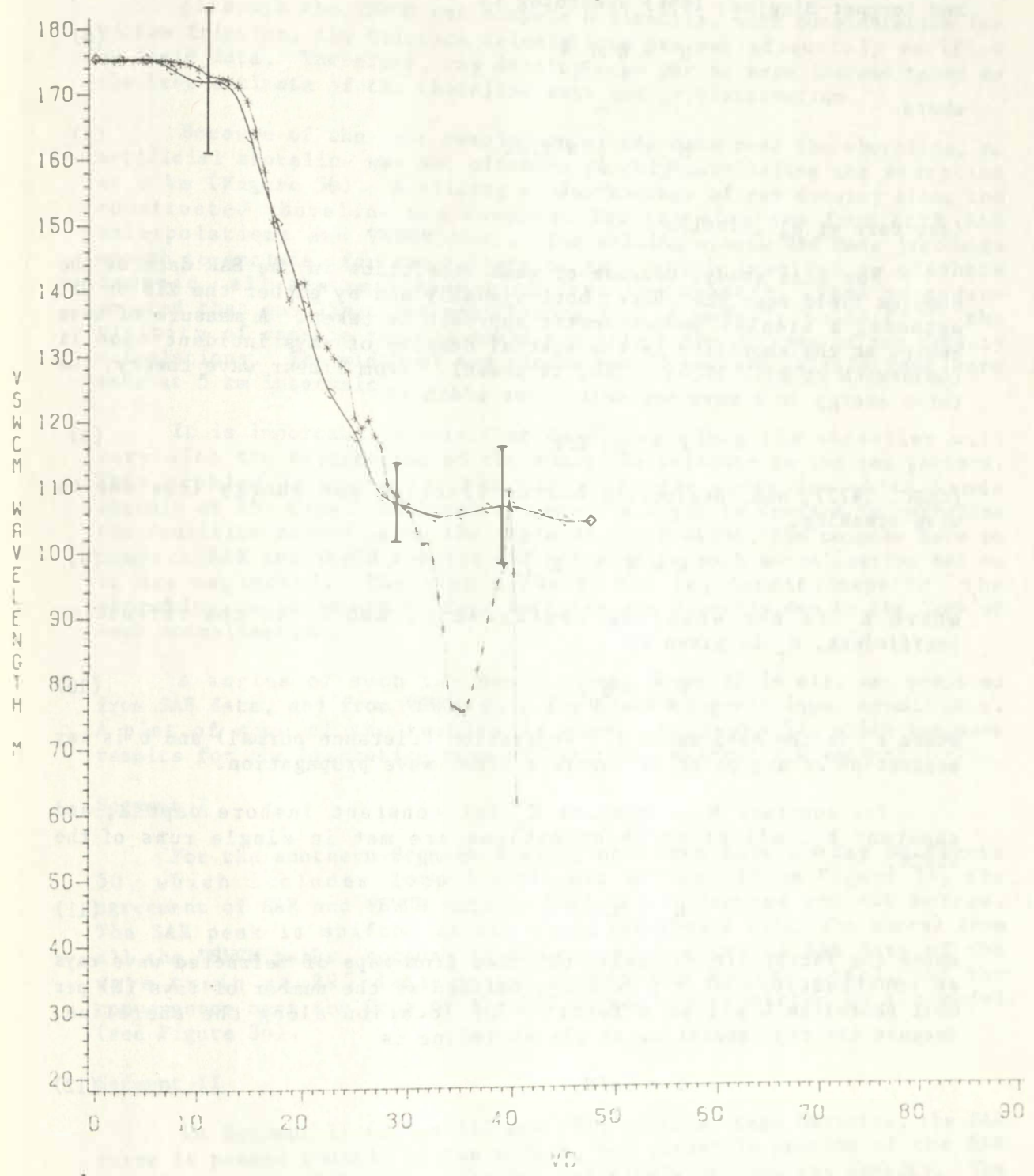


Figure 49. VSWCM and SAR wavelength values along ray #18. Standard deviation error bars are shown for SAR data.

frequency f , wave energy can be estimated from the square of the significant wave height H_s . The inshore value of H_s can be calculated from the zero order moment of the inshore energy spectrum (Cartwright and Longuet-Higgins, 1956) according to

$$H_s = 4 M_0^{1/2} \quad (6)$$

where

$$M_0 = \int_0^{\infty} S(f) df \quad (7)$$

(see Carr et al., 1981).

For this study, because of weak resolution in the SAR data of the complex field near the shore, both visually and by either the ZTS or OFT methods, a simpler monochromatic approach is taken. A measure of wave energy at the shoreline is the spatial density of rays incident upon it (Goldsmith et al., 1974; Allen, in press). From linear wave theory, the total energy in a wave per unit crest width is

$$E = \rho g H^2 L / 8 \quad (8)$$

(CERC, 1977), and, neglecting bottom friction and energy loss due to wave breaking,

$$H = H_0 K_s K_r, \quad (9)$$

where K_s is the shoaling coefficient, and K_r is the refraction coefficient. K_r is given by

$$K_r^2 = b_0 / b, \quad (10)$$

where b_0 is the deep water ray separation (distance normal) and b is ray separation at any point of interest after wave propagation.

For constant H_0 , constant K_s (at constant inshore depth), and constant b_0 , all of which conditions are met in single runs of the VSWCM,

$$E \propto 1/b \quad (11)$$

where the factor $1/b$ is easily obtained from maps of refracted wave rays as constructions of ray density, defined as the number of rays (N) per unit shoreline (Δs), as a function of location along the shoreline. Because the ray separation at the shoreline is

$$b = \Delta s / N, \quad (12)$$

ray density maps are plots of $1/b$, which by Equation (11) is proportional to E .

Although the VSWCM can compute H directly, with consideration for bottom friction, the friction calculations are not adequately verified by field data. Therefore, ray density maps per se were instead taken as the best estimate of the shoreline wave energy distribution.

Because of the poor resolution of SAR data near the shoreline, an artificial shoreline was set offshore roughly paralleling the shoreline at 3 km (Figure 50). A sliding window average of ray density along the constructed shoreline was computed for ray diagrams from both SAR interpolations and VSWCM runs. The sliding window was made just wide enough to include, for any pattern of rays which involved an offshore caustic, all the rays emanating from the caustic. This procedure ensured that any lingering uncertainty in the model's validity in the vicinity of caustic regions would not affect the outcome of ray density calculations. The width of the window was 15 km, and calculations were made at 5 km intervals.

It is important to note that densities along the shoreline will vary with the orientation of the shoreline relative to the ray pattern. This problem is acute for the Cape Hatteras shoreline which bends sharply at the Cape. Although a procedure might be devised to normalize the densities according to the angle of orientation, the purpose here to compare SAR and VSWCM results did not require such normalization and so it was neglected. The high peaks in the ray density maps for the shoreline region south of Cape Hatteras are directly due to the lack of such normalization.

A series of such ray density maps, over 30 in all, was prepared from SAR data, and from VSWCM data for bracketing-run input conditions. A plot of some of the results is shown in Figure 51, which includes results for the bracketing runs of (degrees, metres) 0,0 and +5, +20.

Segment I

For the southern Segment I along northern Raleigh Bay on Figure 50, which includes Zone I and most of Zone II on Figure 35, the agreement of SAR and VSWCM data is best for +5 degrees and -20 metres. The SAR peak is shifted to the right (southward along the shore) from all the VSWCM peaks, because of the appearance in the SAR data of the wave train at 295 degrees not predicted by the model, and the convergence near the Cape of the 320 degree ray predicted by the model (see Figure 34).

Segment II

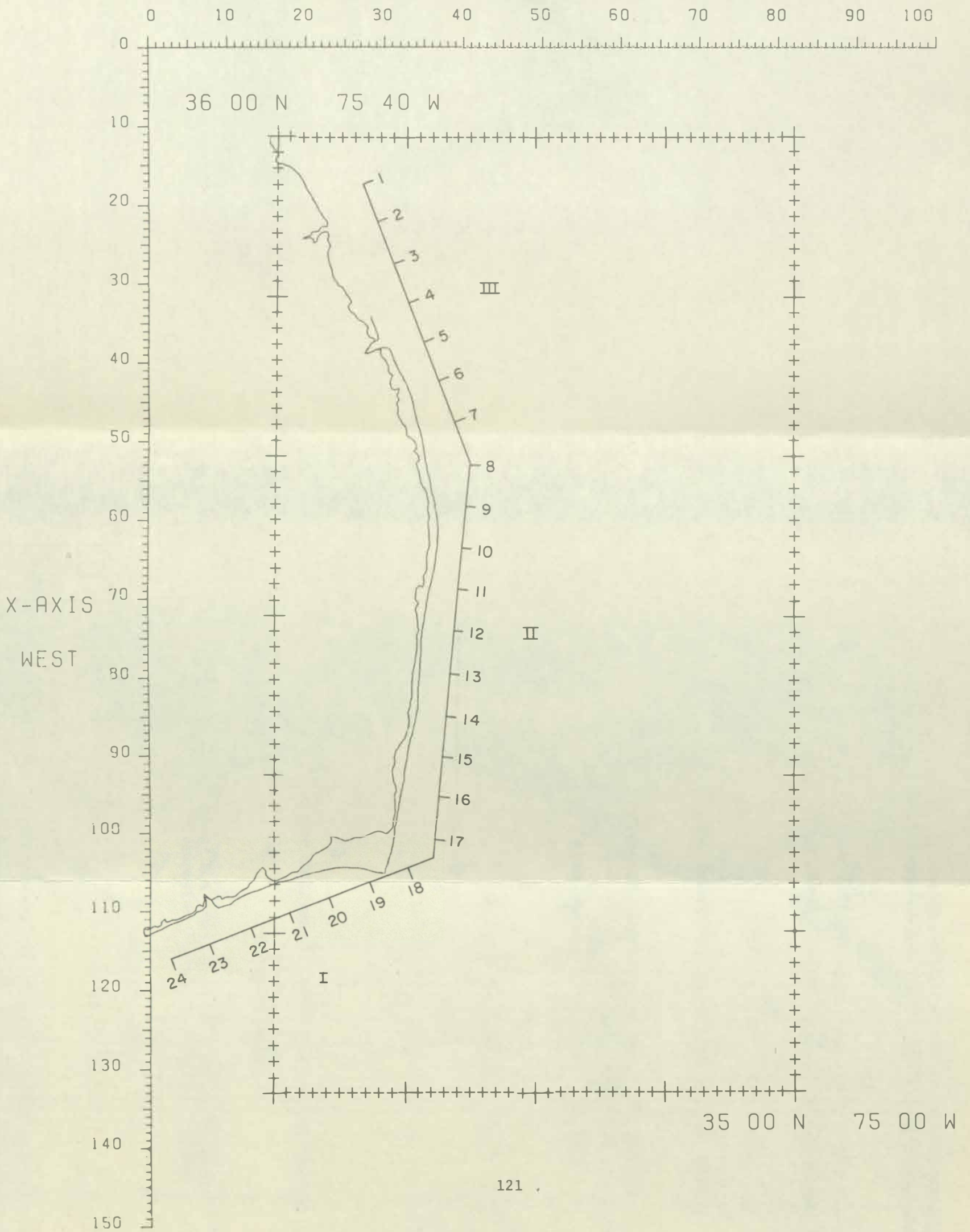
In Segment II (Zones III and IV), north of Cape Hatteras, the SAR curve is peaked roughly in the middle, but visual inspection of the SAR ray diagram shows that the area has relatively uniform ray density. The VSWCM ray density curves are not as uniform, peaking slightly to the south of the middle of the segment. The VSWCM appears to have slightly overestimated the southerly refraction of rays in this segment (as

Figure 50. Artificial shoreline constructed for ray density analysis.

VSWCM WAVE RAY PLOT FOR CAPE HATTERAS

TIDE 1.8

Y-AXIS - NORTH



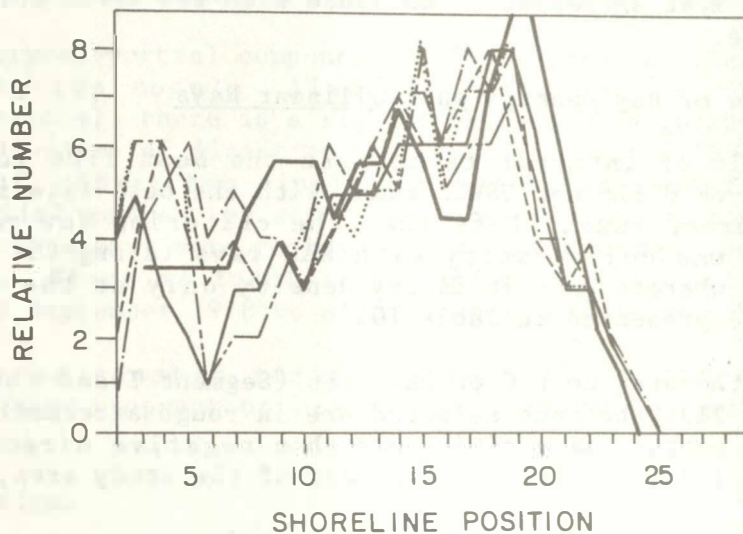


Figure 51. A composite of ray density at the artificial shoreline for various SAR and VSWCM ray diagrams. The SAR results are shown as The VSWCM results are shown as a) nominal case , b) +5 degrees, +20 m . , c) +5, -20 , d) -5, +20 . , e) -5, -20 .

mentioned previously). Best agreement with SAR data is given by the VSWCM curve for -5 degrees, and -20 metres.

Segment III

Finally, in the northern Segment III (Zones V and VI), which includes Platt Shoals, the SAR curve peaks only on the southern portion, while the VSWCM curves peak to the north. Visual inspection of the ray diagrams shows SAR ray density to be relatively uniform in this segment. The VSWCM maps, however, show a marked increase in the number of rays intersecting the northern portion, due mainly to convergence in the "shadow" of the caustic at Platt Shoals. As mentioned before, the VSWCM ray diagrams show rays converging southeast of the Shoals, and subsequently diverging as they pass over the Shoals, a feature not revealed in the SAR ray diagram because of the interpolation algorithm. Removing the rays involved in this convergence pattern causes the VSWCM graph to peak toward the center of the segment, with more agreement with SAR data. Best agreement is obtained with the VSWCM curve for 0 degree and 0 metre.

Comparisons of Ray Density and Collinear Rays

It is of interest to compare the best fits in shoreline ray density from different VSWCM runs, with the best-fits in collinear rays from different runs. Note that the criterion for ray selection in Figure 48 was collinearity with SAR rays (along the entire length of each ray), whereas here it is ray density only at the shoreline. The results are presented in Table 10.

For the area near Cape Hatteras (Segment I and the adjacent part of Segment II), the runs selected are in rough agreement: from south to north, the pattern is positive and then negative direction deviations (see Table 10). In the northern half of the study area, the results are mixed.

Summary

In general, the agreement between SAR and VSWCM ray density maps is fair. In shoreline Segment I, SAR ray density is higher toward the southerly portion, due to the absence of the bimodal component in VSWCM output at the Cape. In Segment II, the VSWCM overestimated southerly refraction. In Segment III, the VSWCM overestimated convergence in the caustic region.

These results emphasize the situation in shallow water, therefore, some amount of the disagreement probably originates in factors mentioned earlier for nearshore measurements, namely, insufficient sampling density, weak SAR wave discrimination, and small measurement areas. Also, in shallow water, where refraction is at a maximum, any errors accumulating from improper simulation over the shelf will be magnified.

D. General Summary for the Cape Hatteras Region

The Virginian Sea Wave Climate Model for the Cape Hatteras region is generally validated by the Seasat Synthetic Aperture Radar data. Overall, agreement between SAR data and VSWCM predictions is very close for the great bulk of the individual rays over the continental shelf. Nearly half of the SAR direction data are within 2 degrees of VSWCM output. The model produces slightly greater southerly refraction than indicated by the SAR data. Prediction of wavelength along rays is generally within the error of measurement. Model prediction of ray density at the shoreline is in fair agreement with SAR data. The model and SAR observations differed significantly in a small region south of Diamond Shoals. The model showed convergence at the point of Cape Hatteras, while the SAR observations showed convergence south of the point. This discrepancy, striking as it appears, involves poor wave clarity over Diamond Shoals itself. Qualitative observation of the SAR imagery bears out the actual convergence of waves at the point.

An observed spectral component of 295 degrees at the Cape was not predicted by the model. Also, from bracketing runs (based on measurement errors), there is a regular pattern of angular offsets from offshore SAR values of direction which produce better VSWCM simulations over the shelf. These two findings might be explained by a current shear and tidal current effects along the Gulf Stream boundary, if the Stream at the boundary were to have appropriate curvature, speed, and orientation. There is insufficient information about the Gulf Stream boundary on 3 September 1978 to allow a more definitive conclusion.

Observed caustic regions were less "intense" than model predictions. Wave propagation beyond caustics was in general modeled successfully.

II. Long Island

A. Pass Selection

Imagery held by the National Environmental Satellite Service and by D. Lichy (U.S. Army Corps of Engineers) was inspected for additional passes which would be useful in wave refraction analyses. Two segments of imagery covering portions of Long Island, New York were deemed to be marginally suitable. The two segments cover areas included in the bathymetric grid assembled for an earlier project supported by the Bureau of Land Management. No imagery for regions outside areas covered by available bathymetric grid data was found to be any more suitable than the selected Long Island segments. The two segments are for passes 1404 and 974. The analyses for these two segments are brief compared to that for Cape Hatteras, pass 974, principally because the data from all relevant perspectives are of poorer quality for wave refraction study: visibility of wave patterns is patchy, the bottom topography off Long Island in the area of SAR coverage is a smoothly-graded one-dimensional slope, and the wave orthogonal directions over the area are nearly normal to shore, yielding only small direction changes due to refraction.

B. Pass 1404, Long Island

The eastern tip of Long Island is covered in pass 1404. Stations in the region of available bathymetric data were sampled using the ZTS technique as described earlier. The wavelength vector results are shown in Figure 52. The raw data from the ZTS observations display dispersions in standard deviation of the mean which are similar to those in the case of Cape Hatteras--for direction the most probable value is less than one degree, and for wavelength the most probable value is in the range 5-10 metres (Figures 53a and b). It was somewhat surprising to find these low values, because by inspection the wave visibility as noted above was poorer than at Cape Hatteras, and noisier observational data were therefore expected.

The SAR-measured orthogonal wave vectors, shown in Figure 52, are not as regular over the area covered as in the case of Cape Hatteras. The evidence suggests that more than one wave train is present. Preliminary VSWCM runs produced ray patterns showing very small refraction; yet, a wide range of directions was found at mid-depth stations. At offshore stations where refraction was negligible, a histogram of directions shows a 20-degree range of directions, substantially larger than the one-degree precision of measurement (Figure 54). At many stations both observers noted multiple wave trains with similar directions, as indicated in Figure 52. The wave visibility at most stations was too poor within the 5-mm subimages for OFT analysis to be of help in further discrimination of the wave field.

Due to the irregular pattern of offshore directions, the VSWCM was run by initiating rays only at the locations of SAR stations; no interpolation was performed to generate additional input data as before. As a result, the number of VSWCM rays is small, and the base on which to compare VSWCM output and SAR data is considerably smaller than for Cape Hatteras.

The VSWCM ray diagram for a tidal height of 1.8 feet above mean low water is shown in Figure 55. The tidal height at Shinnecock Inlet was 0.44 foot (predicted), at the time of the overpass, 2357 hours on 2 October 1978 (local time and date). Actual weather at the time was mild (Montauk: winds N 7 kt, vis. 10 mi., T 69° F., P 29.9 in. At Sandy Hook: winds NNW 10 kt, vis. 6 mi., T 68° F., P 30.03 in.). VSWCM results for a height of 0.0 feet were indistinguishable on graphical output, and negligibly different in the line printer listings of position, wavelength, and direction along each stepped ray.

A visual comparison between the VSWCM ray plot and SAR vector data emphasizes the direction aspects only. There is agreement in the general pattern, but the dispersion in the SAR-measured directions over the field (see Figure 54), together with the very small amount of refraction, precludes a detailed comparison along the length of each ray, as was done for Cape Hatteras. A histogram of the deviations between SAR-measured directions and VSWCM ray directions, for all cases where the normal distance between a SAR station and a nearby VSWCM ray was less than 4 mm (2 km, less than the diameter of each SAR subimage),

SAR WAVELENGTH VECTORS, LI

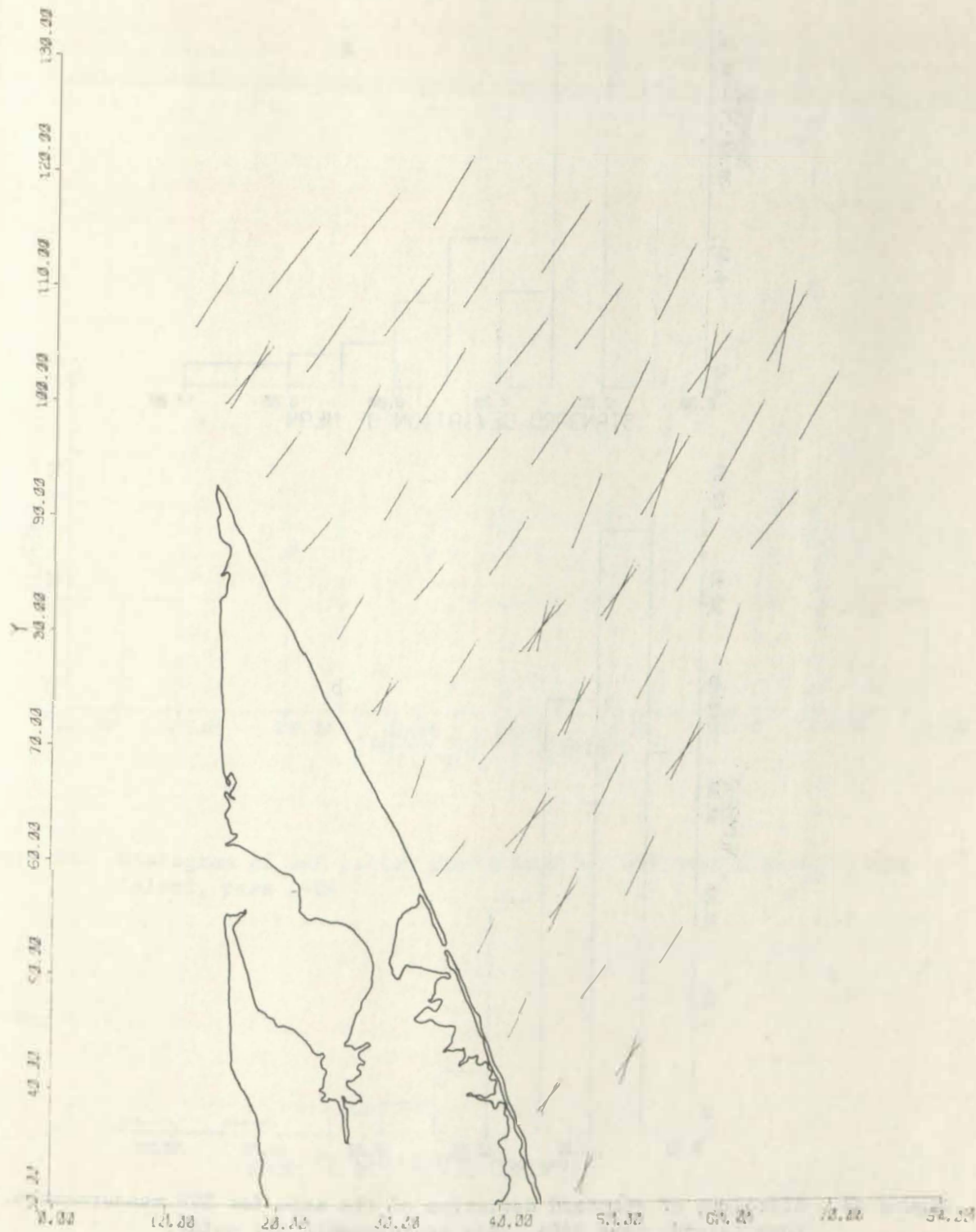


Figure 52. SAR wavelength vectors measured with the ZTS for Long Island, pass 1404. The vector length is proportional to SAR-measured wavelength.

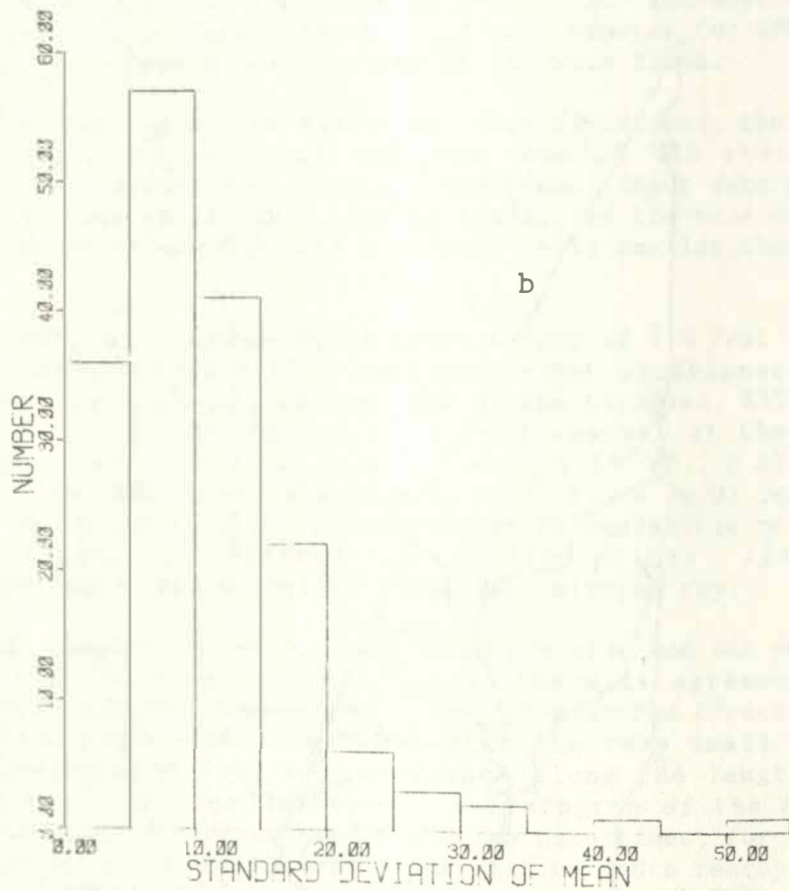
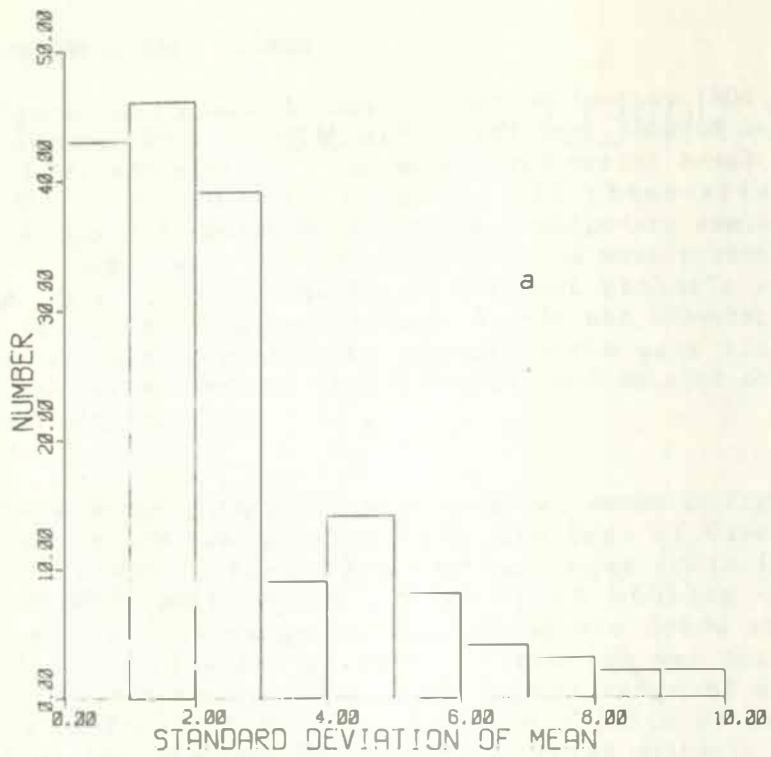


Figure 53. Histogram of standard deviation of the mean for ZTS measurements. Long Island, pass 1404. Six measurements per point. a. direction. b. wavelength.

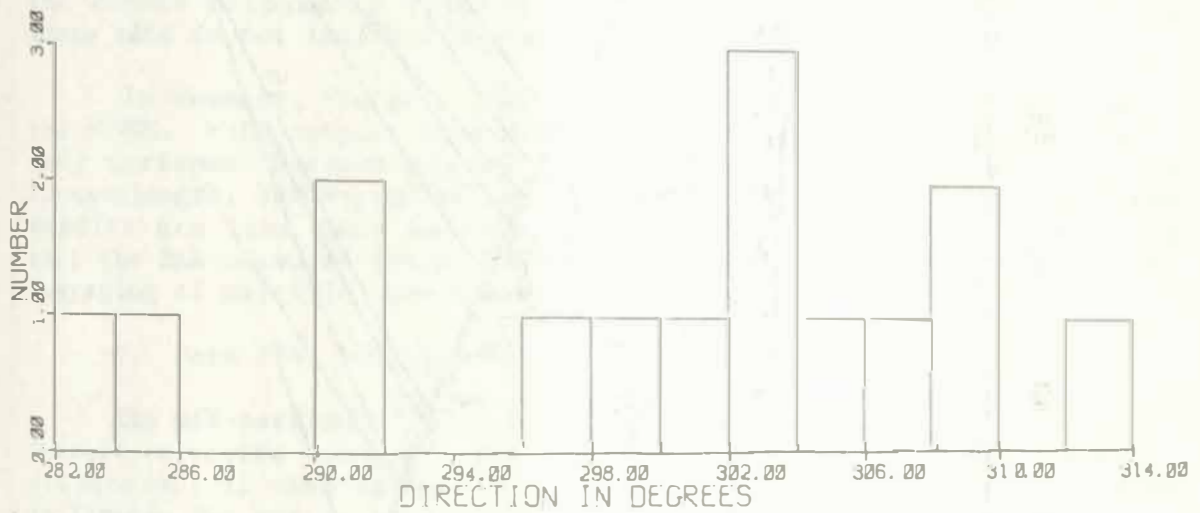


Figure 54. Histogram of SAR vector directions for offshore stations, Long Island, pass 1404.

VSWCM WAVE RAY PLOT FOR LONG ISLAND

TIDE1.9

r-AXIS - NORTH

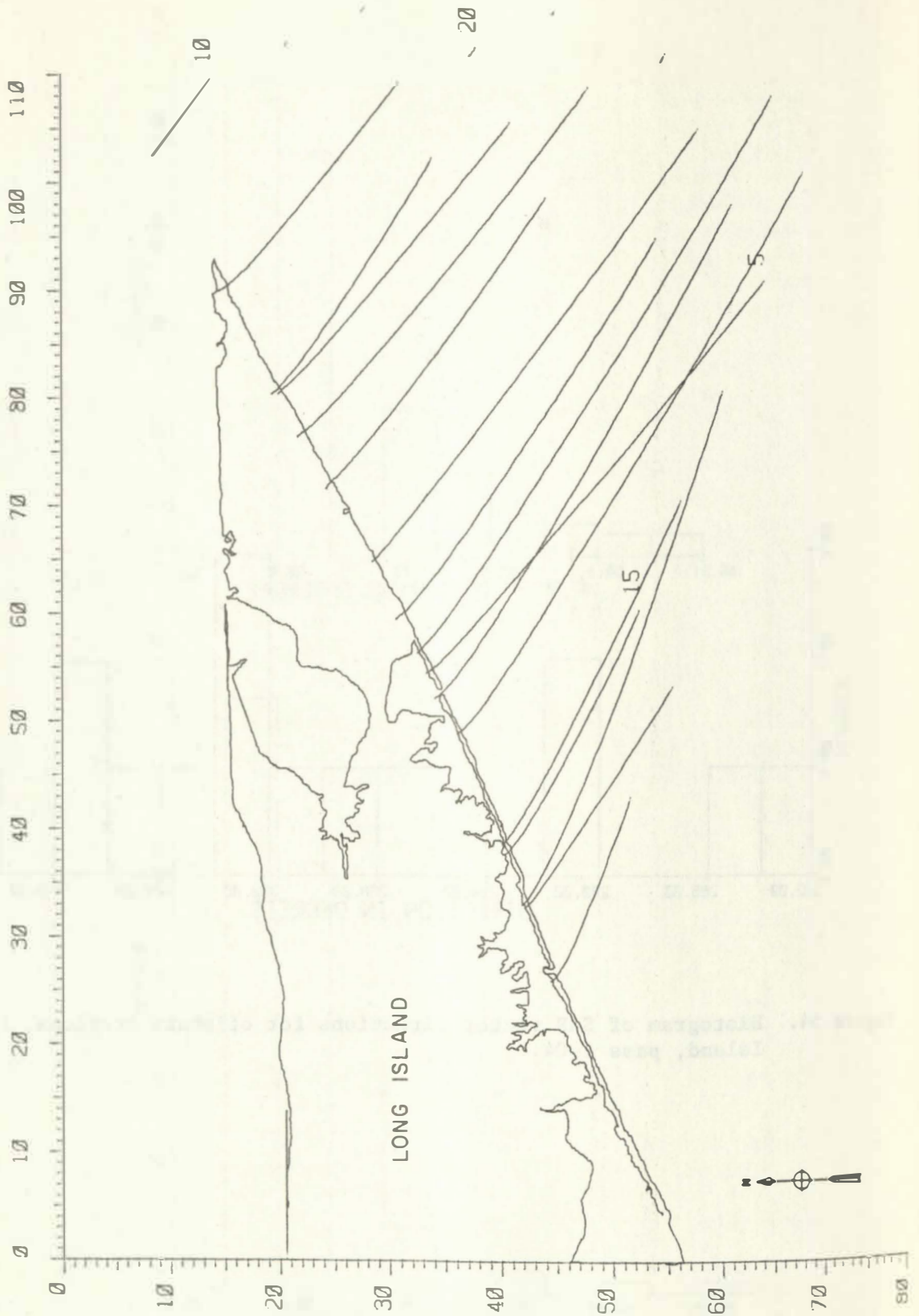


Figure 55. VSWCM run with initial conditions obtained from offshore SAR measurements. Long Island, pass 1404.

is shown in Figure 56. The deviations are centered on zero degrees, but the spread of deviations is very wide compared to the Cape Hatteras observations. The distribution has no doubt been widened by comparisons involving wave trains progressing in different directions; the extent of this effect can not be determined, because the different wave trains are not separable over the area of interest.

A similar histogram of wavelength deviations is greatly biased, with most VSWCM wavelengths exceeding SAR-measured values by an average of 30 metres (Figure 57). The bias is not at all affected by changing the tide level in the model. The accuracy of these results has been degraded by the poor wave visibility, but there are sufficiently clear wave patterns at some locations in the imagery to yield reliable wavelengths. The results from such locations are generally in agreement with wavelengths measured in areas of poorer visibility.

Not producing a VSWCM run with a high density of rays has precluded any investigation of possible caustics in the area of study. The smooth bathymetry suggests that none would be generated, and the image data do not indicate any strong convergences.

In summary, the pass 1404 permits at best only a marginal test of the VSWCM. With respect to direction of wave orthogonals, there is only fair agreement between the SAR data and the VSWCM output. With respect to wavelength, VSWCM predictions are an average of 30 metres high. The results are less than satisfactory. This outcome is due to the fact that the SAR-measured vector field is irregular and probably involved averaging of multiple wave trains of similar directions.

C. Pass 974, Long Island

The mid-section of Long Island is covered in pass 974. Wavelength vectors extracted using the ZTS technique are shown in Figure 58. The dispersions in standard deviation of the mean of the raw data are shown in Figures 59a and b; for direction the most probable value is in the range 1-2 degrees, and for wavelength, the most probable value is in the range 5-10 metres.

The SAR-measured orthogonal wave vectors, shown in Figure 58, are obviously irregular over the study area, and there are numerous crossed seas. OFTs obtained for a sample of the stations confirmed the results of the ZTS measurements. The pattern of results indicates that interfering waves are present; fortunately, for the most part the different wave trains have widely different directions, which has facilitated the exclusion of all but one wave train from the vector results in the comparisons which follow.

The VSWCM was run using as input the SAR data from stations with the 330-degree wave train, obviously the dominant wave train in the field. The results of the run are shown in Figure 60. This run, for a tide level of 1.8 feet above mean low water, was nearly identical to a run for a tide level of 0.0 feet; the Shinnecock Inlet tide level during the overpass was 1.0 foot (predicted) during the overpass, 2148 hours on 2 September 1978 (local time and date). Actual weather at the time was

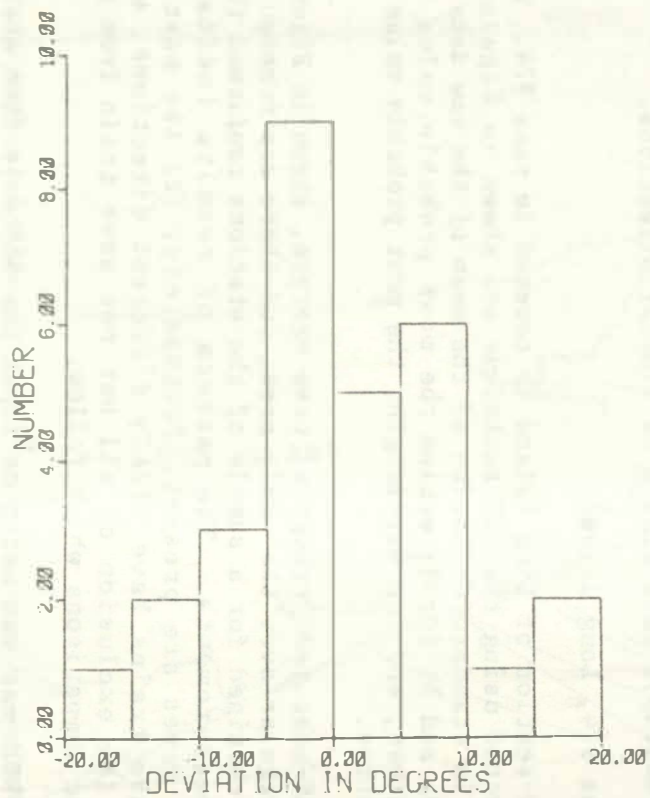


Figure 56. Histogram of direction deviations (SAR vs. VSWCM) for Long Island, pass 1404.

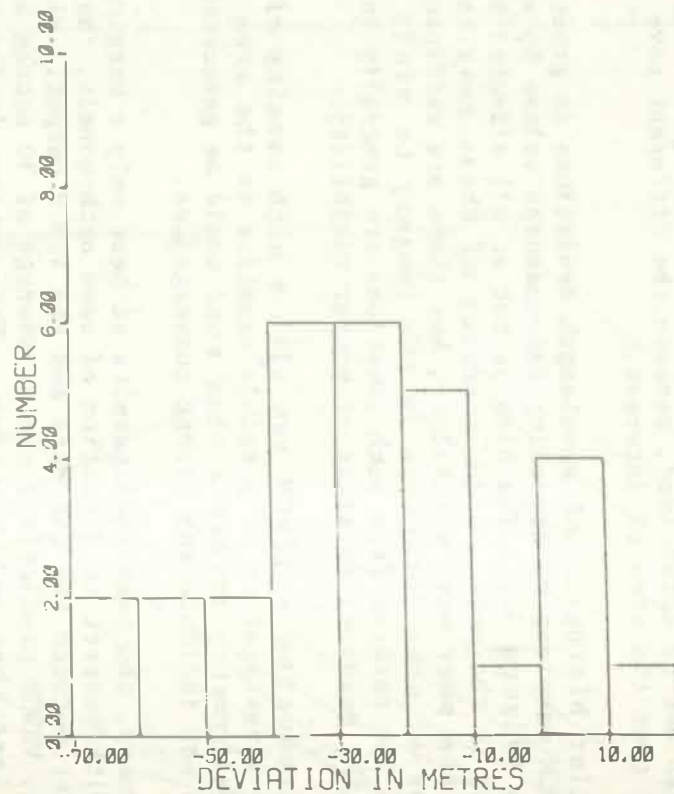


Figure 57. Histogram of wavelength deviations (SAR vs. VSWCM) for Long Island, pass 1404.

mild (Montauk: winds SSW 7 kt, vis. 5 mi., T 70⁰ F., P 30.19 in. At Sandy Hook: winds SW 9 kt, vis. 6 mi., P 30.12).

A histogram of the deviations between SAR-measured directions and VSWCM ray directions, for all cases where the normal distance between stations and rays was less than 4 mm, and excluding cases with obviously different wave trains, is shown in Figure 61. More than 45% of the deviations lie within ± 2 degrees, and more than 70% lie within ± 3 degrees. The small range in deviations is partly the result of the small amount of refraction for this pass, which averaged only 8.57 degrees for 21 VSWCM rays.

A histogram of the deviations between measured and predicted wavelengths is shown in Figure 62. The most probable value is - 4 metres, indicating that VSWCM wavelengths tend to exceed SAR-measured wavelengths. More than 43% of the deviations lie within the range - 12 to + 4 metres, and 63% lie within - 16 to + 8 metres. The better agreement here compared to pass 1404 is believed to result from the exclusion of other wave trains before analysis, made possible by their widely different directions.

In summary, the pass 974 Long Island results provide at best a fair agreement between model and measurement. As in the other passes, the wavelength data contain more noise and yield less agreement than the direction data. Lack of better agreement is attributed to the low quality of the data in the wave field on the imagery supplied.

... ..

... ..

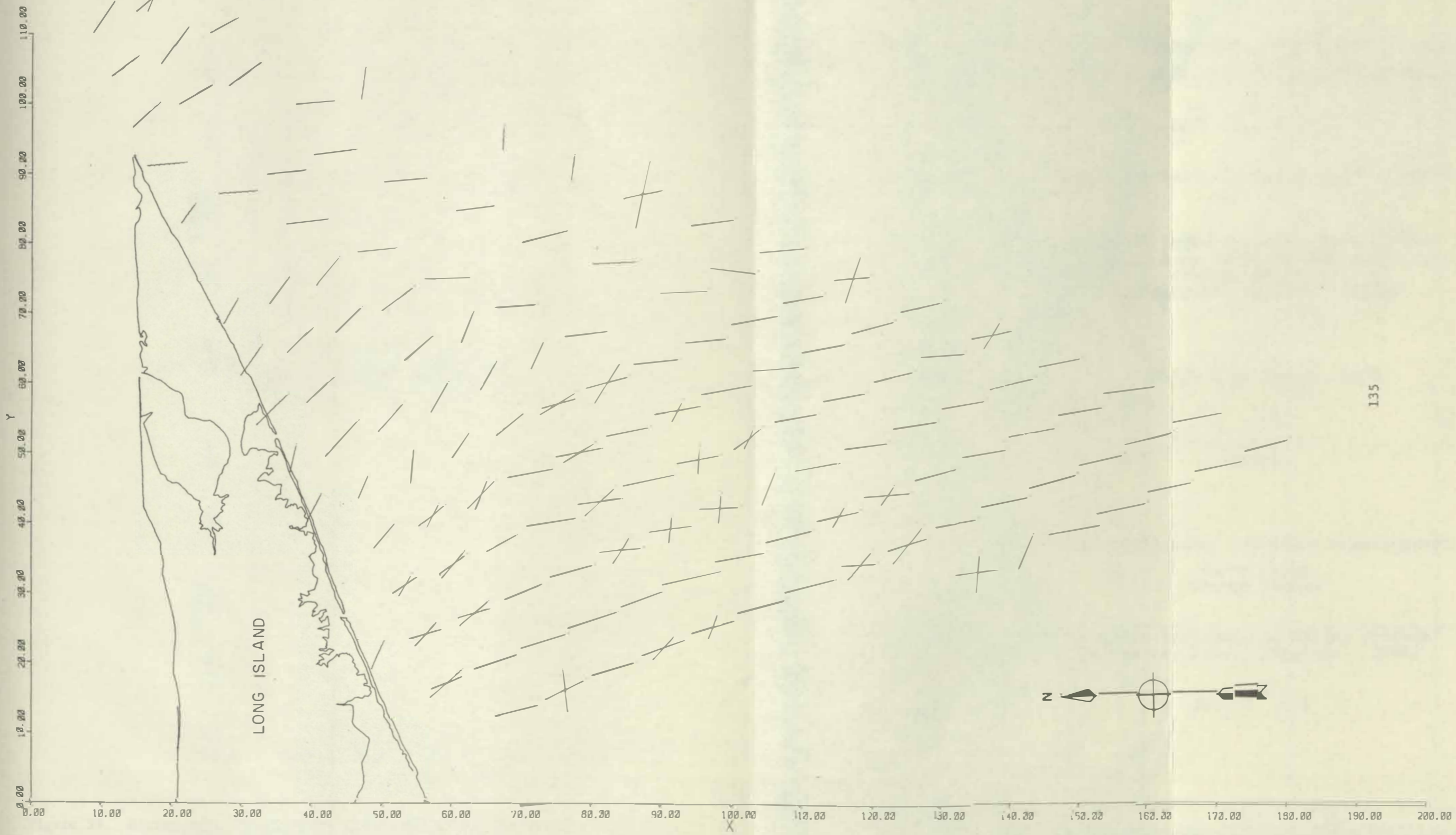
... ..

... ..

Figure 58. SAR wavelength vectors measured with the ZTS at Long Island, pass 974. The vector length is proportional to SAR-measured wavelength.



SAR WAVELENGTH VECTORS, LI



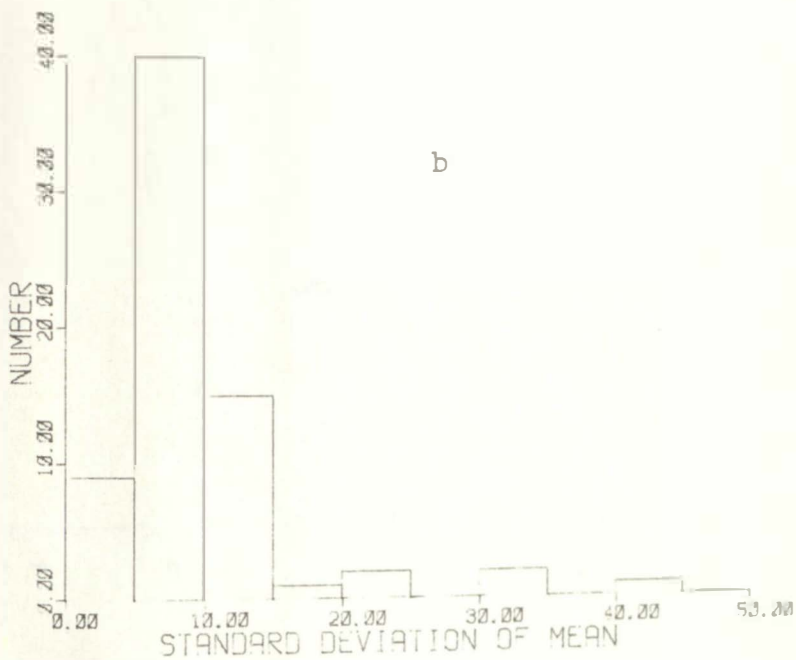
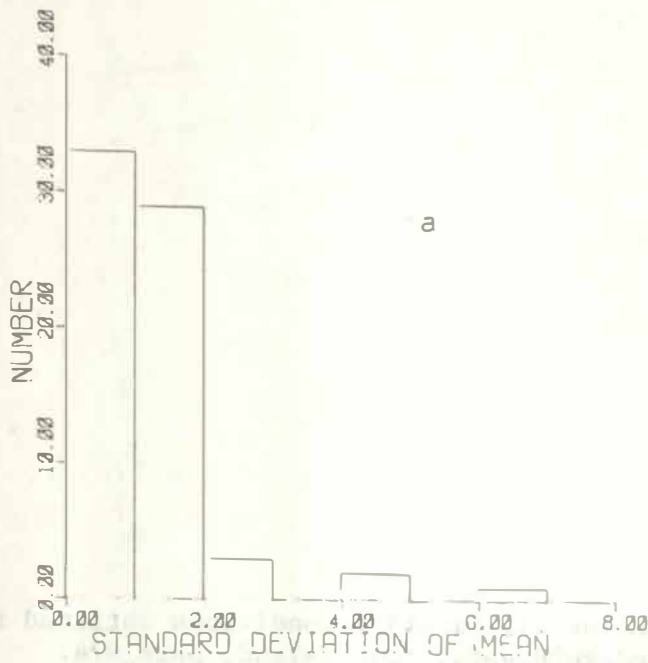


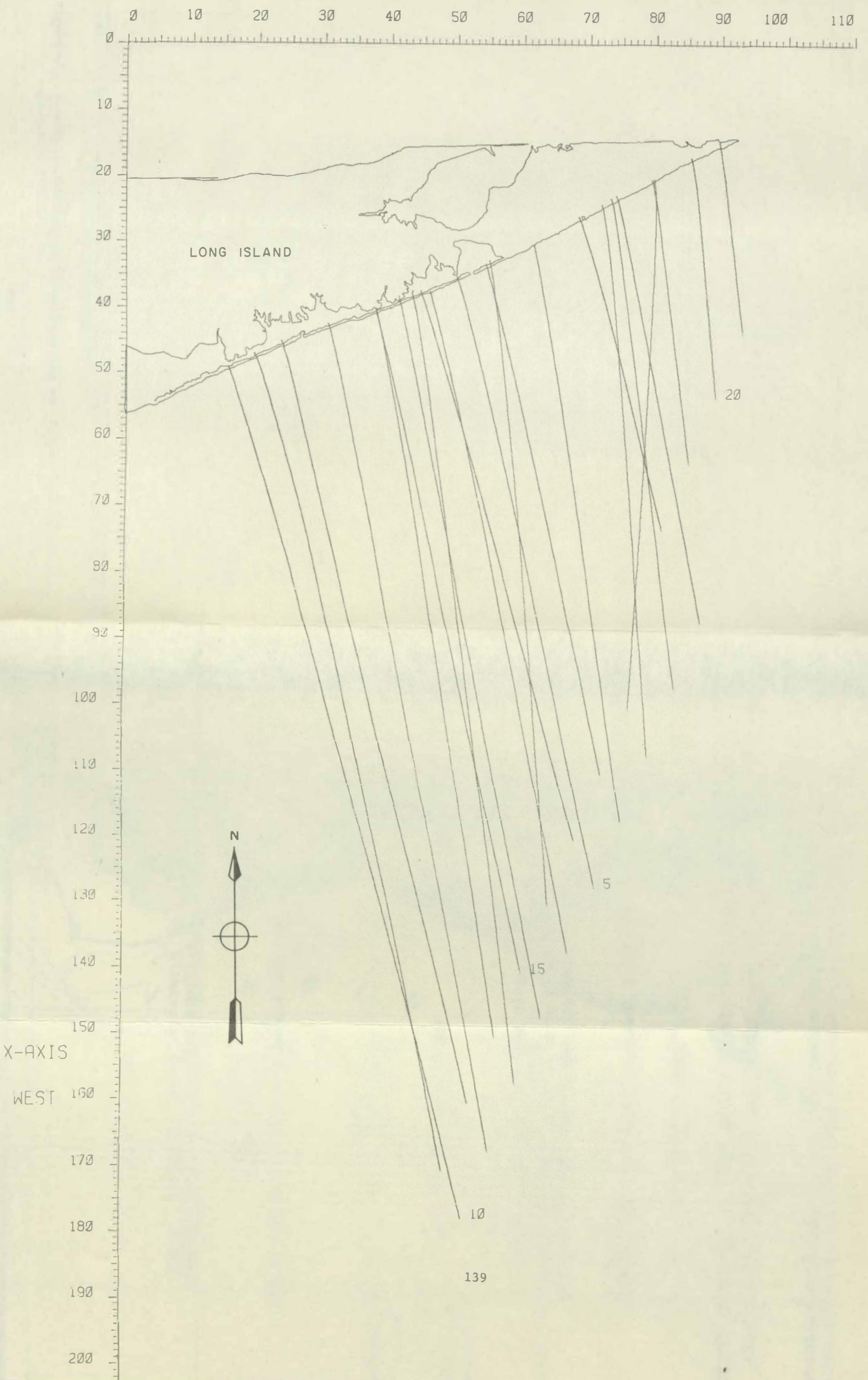
Figure 59. Histogram of standard deviation of the mean for ZTS measurements, Long Island, pass 974.
 a. direction. b. wavelength.

Figure 60. VSWCM run with initial conditions obtained from offshore SAR measurements, Long Island, pass 974.

VSWCM WAVE RAY PLOT FOR LONG ISLAND

TIDE 1.8

Y-AXIS - NORTH



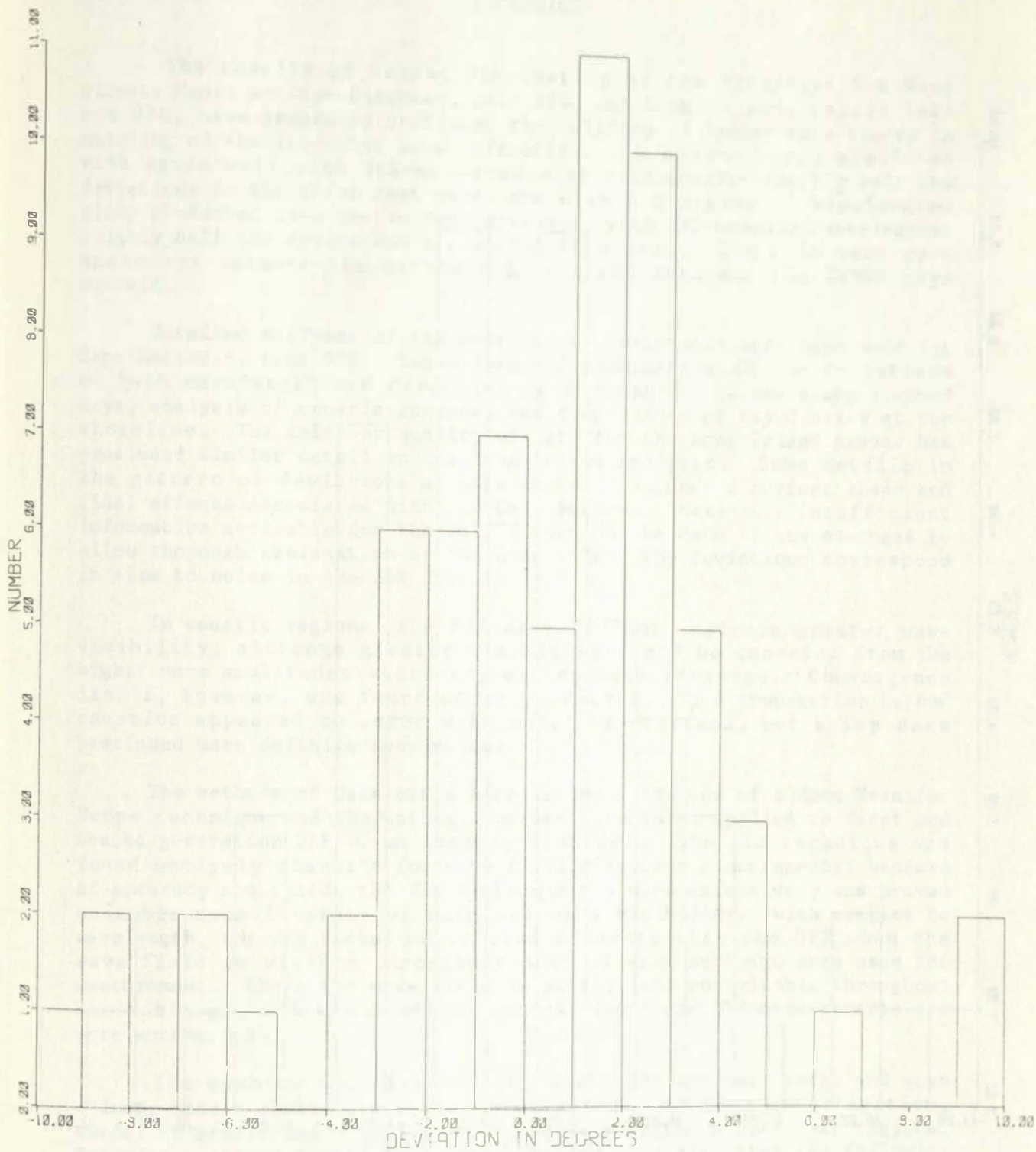


Figure 61. Histogram of direction deviations (SAR vs. VSWCM) for Long Island, pass 974.

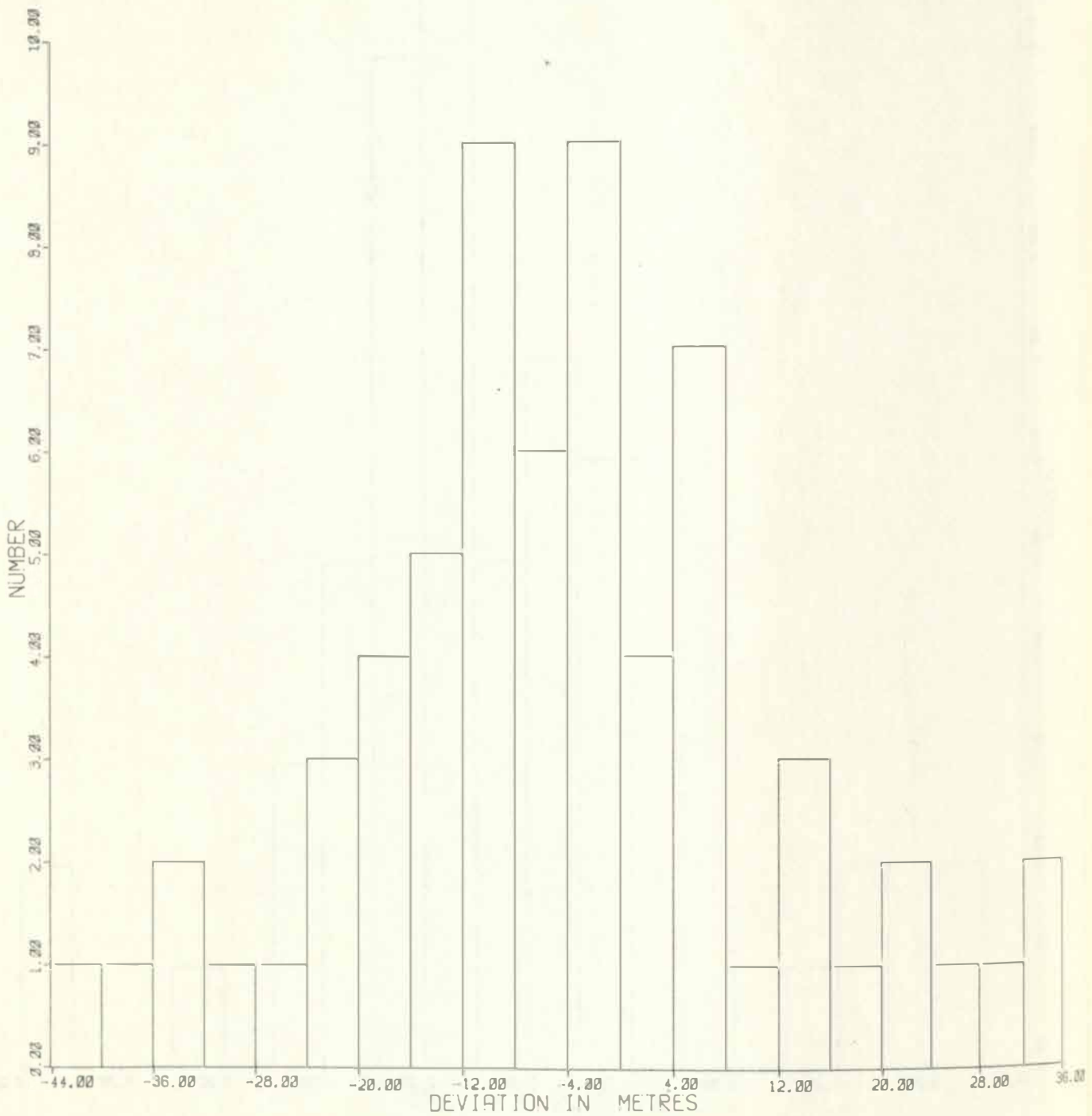


Figure 62. Histogram of wavelength deviations (SAR vs. VSWCM) for Long Island, pass 974.

CONCLUSION

The results of Seasat SAR testing of the Virginian Sea Wave Climate Model at Cape Hatteras, pass 974, and Long Island, passes 1404 and 974, have generally confirmed the validity of linear wave theory in modeling of shallow-water wave refraction. Directions along predicted rays agree well with SAR-measured wave orthogonals--roughly half the deviations in the three test cases are within 2 degrees. Wavelengths along predicted rays are in fair agreement with SAR-measured wavelength: roughly half the deviations are within 10 metres. There is very good agreement between the patterns in the SAR data and the VSWCM rays overall.

Detailed analyses of the patterns of deviations have been made for Cape Hatteras, pass 974. These involved examination of the deviations of both wavelength and direction from measured values along stepped rays, analysis of caustic regions, and comparisons of ray density at the shoreline. The inferior quality of data for the Long Island passes has precluded similar detail in the Long Island analyses. Some details in the pattern of deviations at Cape Hatteras suggested current shear and tidal effects associated with the Gulf Stream. There was insufficient information available for the Gulf Stream on the date of the overpass to allow thorough explanation of these details. The deviations correspond in size to noise in the SAR data.

In caustic regions, the SAR data did not indicate greater wave visibility, although greater visibility would be expected from the higher wave amplitudes where ray orthogonals converge. Convergence itself, however, was found where predicted. Wave propagation beyond caustics appeared to agree with model predictions, but noisy data precluded more definite conclusions.

The methods of data extraction included the use of a Zoom Transfer Scope technique and the Optical Fourier Transform, applied to first and second generation SAR 70 mm imagery from JPL. The ZTS technique was found entirely adequate for wave field direction measurements; because of accuracy and speed, the ZTS technique was used extensively and proved suitable even in areas of marginal wave visibility. With respect to wavelength, the ZTS technique is less accurate than the OFT when the wave field is visible throughout most of each subimage area used for measurement. Where the wave field is patchy, and not visible throughout the subimage, OFT measurements are difficult and ZTS measurements are more successful.

The combination of satellite synthetic aperture radar and wave climate models should prove, based on results of this investigation, useful in predicting wave direction and wavelength in nearshore regions. Experience gained during this investigation indicates that the following considerations need to be addressed for success in such a venture:

1. Complete automation of the data extraction phase will be difficult. The exclusive use of OFTs obtained digitally or automatically via optical methods will necessitate the use of

algorithms to find spectral peaks in the transform plane. Smoothing techniques and signal/noise ratios will be required, and for wave patterns on the margin of detectability, extremely noisy results will be probable. OFT spectra typically show quite large variations in wavelength (much larger proportionally than for direction). The percentage error possible for cases of marginal visibility will be very high. Moreover, multiple wave trains are common, not exceptional. Wave trains with similar directions will easily be confused during an automated process, unless the data rejection threshold is high. For these various reasons, significant improvement in data acceptance and/or accuracy can be expected with the incorporation of visual methods. These would include both visual quality control, and visual techniques of data extraction.

2. Bathymetric data comparable to that used in this investigation will be adequate for wave climate modeling. The Cape Hatteras analysis did not indicate that any significant gain would derive from improved bathymetric data.
3. Timing mark data for offshore synthetic aperture radar imagery (optically-correlated) must have high accuracy. Care in cartographic technique is required for passes covering significant arcs of the earth's surface.

COMMENTS ON FURTHER ANALYSIS

1. The Cape Hatteras pass could be analyzed with higher precision using digital imagery and digital Fourier Transforms exclusively. Data could be corrected for slant range distortion. The error analyses of the present investigation indicate that deviations between SAR data and VSWCM runs are close in size to probable errors of measurement. The more precise data expected from exclusive use of digital methods would sharpen the analysis, particularly in caustic regions. It is uncertain, however, that digital methods would alter the conclusions significantly.
2. Under the assumption that Fourier Transforms provide a measure of wave energy spectra, digital Fourier Transforms could be used to test the VSWCM for its wave height predictions. For energy calibration of the Transforms, however, the data are meager, consisting of a one-dimensional wave spectrum available for pass 974 taken at the U.S. Army Corps of Engineers CERC pier at Duck, North Carolina.
3. The VSWCM could be modified to provide a better simulation of wave behavior in the region of caustics, and new comparisons made of the results with SAR data.

4. The present analysis has suggested that the general behavior of polychromatic wave trains of small bandwidth would be insignificantly different from the behavior of monochromatic wave trains. This finding has resulted from the use of bracketing ranges of wavelength and direction in the simulations. However, a true polychromatic analysis with mathematical superposition of results and non-linear interactions has not been performed. Some minor details not uncovered in the present analysis might appear in a truly polychromatic analysis. Also, the slight bias of the SAR toward enhancement of the longer wavelengths could be corrected in additional analysis, but the impact would probably be negligible.

REFERENCES

- Allen, J.R. 1981 preprint. Theoretical model of shoreline dynamics at Sandy Hook Spit, New Jersey. *Northeastern Geol.*, 11 p.
- Barber, N.F. 1949. A diffraction analysis of a photograph of the sea. *Nature* 164(4168):485.
- Beal, R.C. 1980. Spaceborne imaging radar: monitoring of ocean waves. *Science* 208:1373-1375.
- Beal, R.C. 1981. Spatial evolution of ocean wave spectra. In: *Spaceborne Synthetic Aperture Radar for Oceanography*, R.C. Beal, F.S. DeLeonibus, and I. Katz (eds.), Johns Hopkins Univ. Press, Baltimore, Md., p. 110-127.
- Carr, A.P., H.L. King, A.D. Heathershaw, and B.J. Lees. 1981. Sizewell-Dunwich Banks field study Topic Report 6: wave data: observed and computed climates. Report No. 128, Inst. Oceanogr. Sci., Taunton, Somerset, England, 97 p.
- Cartwright, D.E. and M.S. Longuet-Higgins. 1956. The statistical distribution of the maxima of a random fluctuation. *Proc. Royal Soc. A*(231):212-232.
- Chao, Y.-Y. 1971. An asymptotic evaluation of the gravity wave field near a smooth caustic. *J. Geophys. Res.* 76(30):7401-7408.
- Coastal Engineering Research Center. 1977. Shore protection manual (3rd ed.). Vol. I, U.S. Army, U.S.G.P.O., Washington, D.C. sep. p.
- Dobson, R.S. 1967. Some applications of a digital computer to hydraulic engineering problems. Techn. Rep. No. 80, Dep. Civil Eng., Stanford Univ. (available from DDC as AD 659 309).
- Egbert, D., J. McCauley, F. Ulaby, and J. McNaughton. 1974. Optical data processing analysis of stream patterns exhibited on ERTS-1 imagery. *Proc. 9th Int. Symp. Remote Sensing of Env., Env. Res. Inst. Michigan, Ann Arbor*, p. 1933-1951.
- Goldsmith, V. and J.M. Colonell. 1974. Results of ocean wave-continental shelf interaction. *Proc. 14th Int. Coastal Eng. Conf., ASCE, New York*, 6 p.
- Goldsmith, V., W.D. Morris, R.J. Byrne, and C.H. Whitlock. 1974. Wave climate model of the Mid-Atlantic shelf and shoreline (Virginian Sea). NASA SP-358, VIMS SRAMSOE No. 38, NASA Hq, Washington, D.C., 146 p.
- Gonzales, F.I., R.C. Beal, W.E. Brown, J.F.R. Gower, D. Lichy, D.B. Ross, C.L. Rufenach, and R.A. Shuchman. 1979. Seasat Synthetic Aperture Radar: ocean wave detection capabilities. *Science* 204:1418-1421.

- Johnson, J.W. 1947. The refraction of surface waves by currents. Trans. Am. Geophys. Un. 28(6):867-874.
- Kasevich, R.S., C.H. Tang, and S.W. Henriksen. 1971. Energy spectra of sea waves from photographic interpretation. Proc. 7th Int. Symp. Remote Sensing of Env., Env. Res. Inst. Michigan, Ann Arbor, p. 607-624.
- Kasischke, E.S., R.A. Shuchman, G.A. Meadows, P.L. Jackson, Y. Tseng, and J.D. Lyden. 1981. Further Seasat SAR coastal ocean wave analysis. ERIM Final Report No. 138600-6-F, Ann Arbor, Michigan, 139 p. + app.
- Kirby, M.E. and D. Steiner. 1977. A theoretical model for evaluation of the interactions between Landsat data and UTM maps in geometric transformations. Remote Sensing of Earth Resources, vol. 6, Univ. Tennessee Space Inst., Tullahoma, p. 407-422.
- Mapp, G.R. 1982. Wave refraction by warm core rings. M.A. Thesis, College of William and Mary, Gloucester Point, Virginia, 60 p. + app.
- Phillips, O.M. 1981. The structure of short gravity waves on the ocean surface. In: Spaceborne Synthetic Aperture Radar for Oceanography, R.C. Beal, P.S. DeLeonibus, and I. Katz (eds.), Johns Hopkins Univ. Press, Baltimore, Md., p. 24-31.
- Pickett, R.L. 1966. Environmental corrections for an airborne radiation thermometer. Proc. 4th Symp. Remote Sensing of Env., Env. Res. Inst. Michigan, Ann Arbor, p. 259-262.
- Raney, R.K. 1980. SAR processing of partially coherent and sinusoidally dynamic ocean waves. Proc. 6th Canadian Symp. Remote Sensing, Halifax, Canad. Aero. Space Inst., Ottawa, Ontario, Canada, p. 243-248.
- Shuchman, R.A., E.S. Kasischke, A. Klooster, and P.L. Jackson. 1979. SAR coastal ocean wave analysis--a wave refraction and diffraction study. ERIM Final Report No. 138600-2-F, Ann Arbor, Michigan, 78 p. + app.
- Stilwell, D., Jr. 1969. Directional energy spectra of the sea from photographs. J. Geophys. Res. 74(8):1974-1986.
- Stommel, H. 1965. The Gulf Stream: a physical and dynamical description. Univ. California Press, Berkeley, 248 p.
- Wu, C., B. Barkan, B. Huneycutt, C. Leang, and S. Pang. 1981. An introduction to the interim digital SAR processor and the characteristics of the associated SEASAT SAR imagery. Jet Prop. Lab., California Inst. Techn., Pasadena, 82 p. + app.

APPENDICES

- A. Calculating ground range at any point on image.
- B. Calculating errors for measured values of wavelength and direction.
- C. VSWCM ray diagrams simulating conditions at Cape Hatteras, 3 September 1978.
- D. Wavelength versus ray distance plots.
- E. Abstracts of previous reports under this project.

APPENDIX A

CALCULATING GROUND RANGE AT ANY POINT ON IMAGE

Calculate ground range to near edge of subswath

Read:

slant range of swath edge, r_e (km)

altitude, H (km)

radius of earth, R_e (km)

Calculate:

radar look angle for swath edge, A_e (radians)

ground range of swath edge, X_e (km)

Calculate ground range to any point on image

Read:

image range from near edge of subswath, x (cm)

ratio: change in slant range/change in image range

This quantity, dr/dx (km/cm), is equal to "slant range scale factor" divided by 10 degrees

Note: The value for "slant range scale factor" taken from the auxiliary data listing is approximately 200 and unitless.

Calculate:

new slant range to point on image, r (km)

Note: $r = x*dr/dx + r_e$.

new incidence angle to point on image, A (radians)

ground range to point on image, X

ground range to near edge of swath, $X - X_e$

Note: The value of $X - X_e$ can be compared to that calculated using a uniform scale of 1/500,000.

APPENDIX B

CALCULATING ERRORS FOR MEASURED VALUES OF WAVELENGTH AND DIRECTION

Calculate components of wavelength "vector":

Read measured values of wavelength and direction, L (m) and D (degrees)

Convert direction, D into radians, A with respect to azimuth

Calculate azimuth and range components of wavelength, L_x and L_y, using scale of 1/500,000

Recalculate range component of wavelength:

Enter image range from near edge of subswath, x, for area of interest

Calculate ground range from near edge of subswath, X (X-X_e in Appendix A)

Calculate exact range scale for sampling location, dr/dX

Calculate range scale $dx/dX = (dr/dX)*(dx/dr)$

Note: dr/dx is defined in Appendix A.

Calculate corrected azimuth component of wavelength,
 $L_y = (dX/dx)*(1/500,000)$

Calculate corrected wavelength and direction, L and A

Note: $L = (L_x^{**2} + L_y^{**2})^{**1/2}$.

Also, $A = \text{arc tan}(L_y/L_x)$

Convert A to D

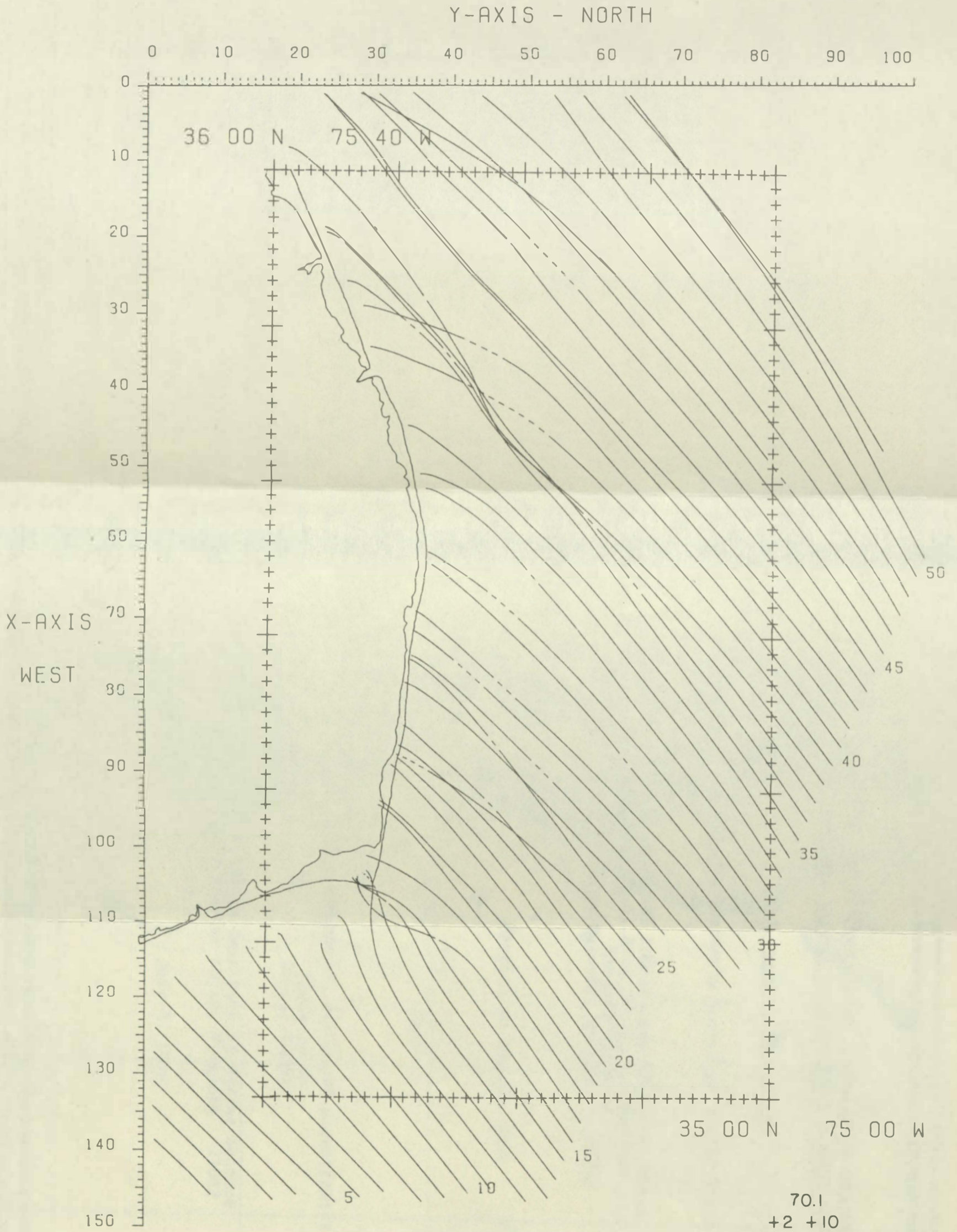
New values can now be compared to uncorrected values

APPENDIX C

VSWCM Ray Diagrams Simulating Conditions
at Cape Hatteras, 3 September 1978

VSWCM WAVE RAY PLOT FOR CAPE HATTERAS

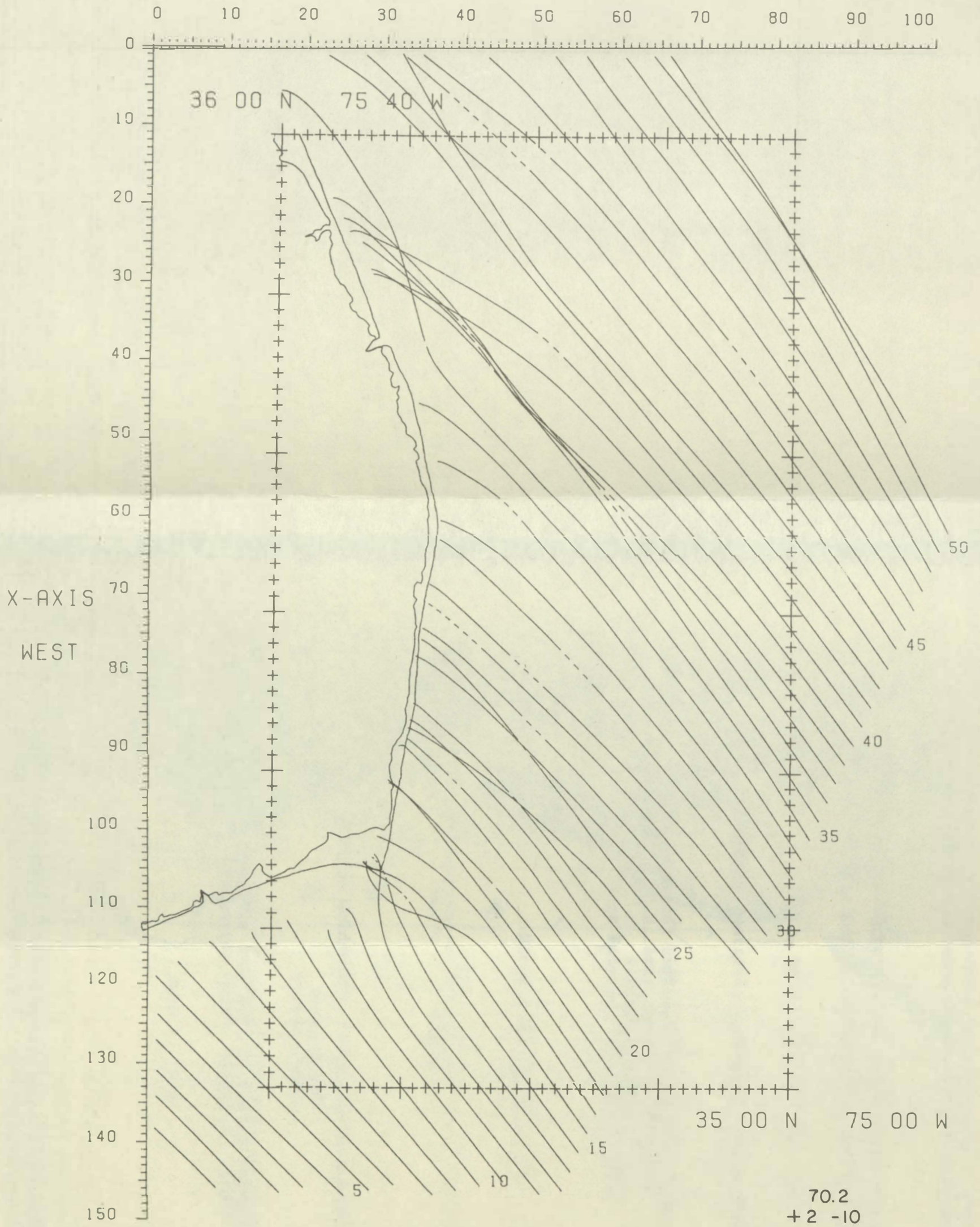
TIDE 1.8



VSWCM WAVE RAY PLOT FOR CAPE HATTERAS

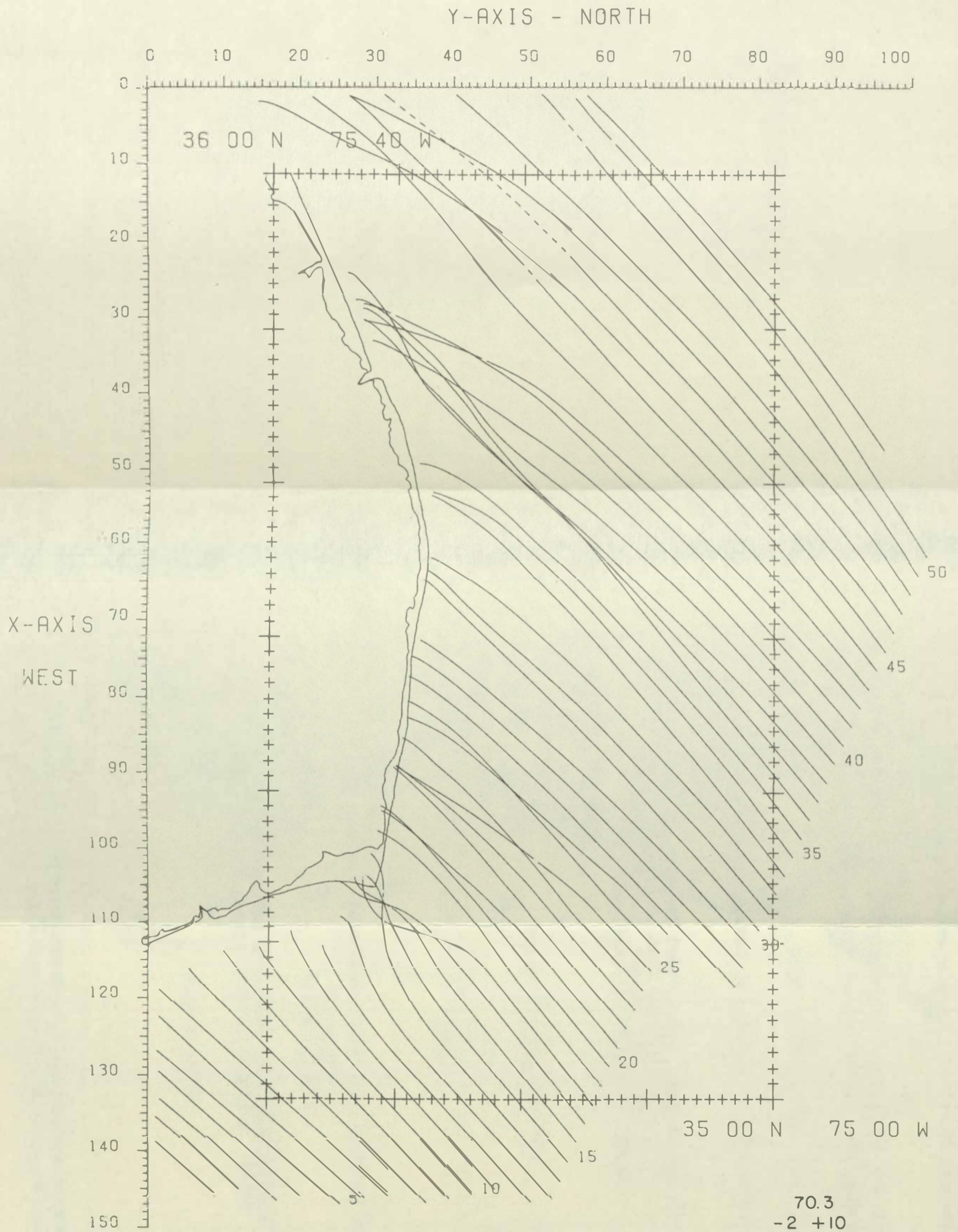
TIDE 1.8

Y-AXIS - NORTH



VSWCM WAVE RAY PLOT FOR CAPE HATTERAS

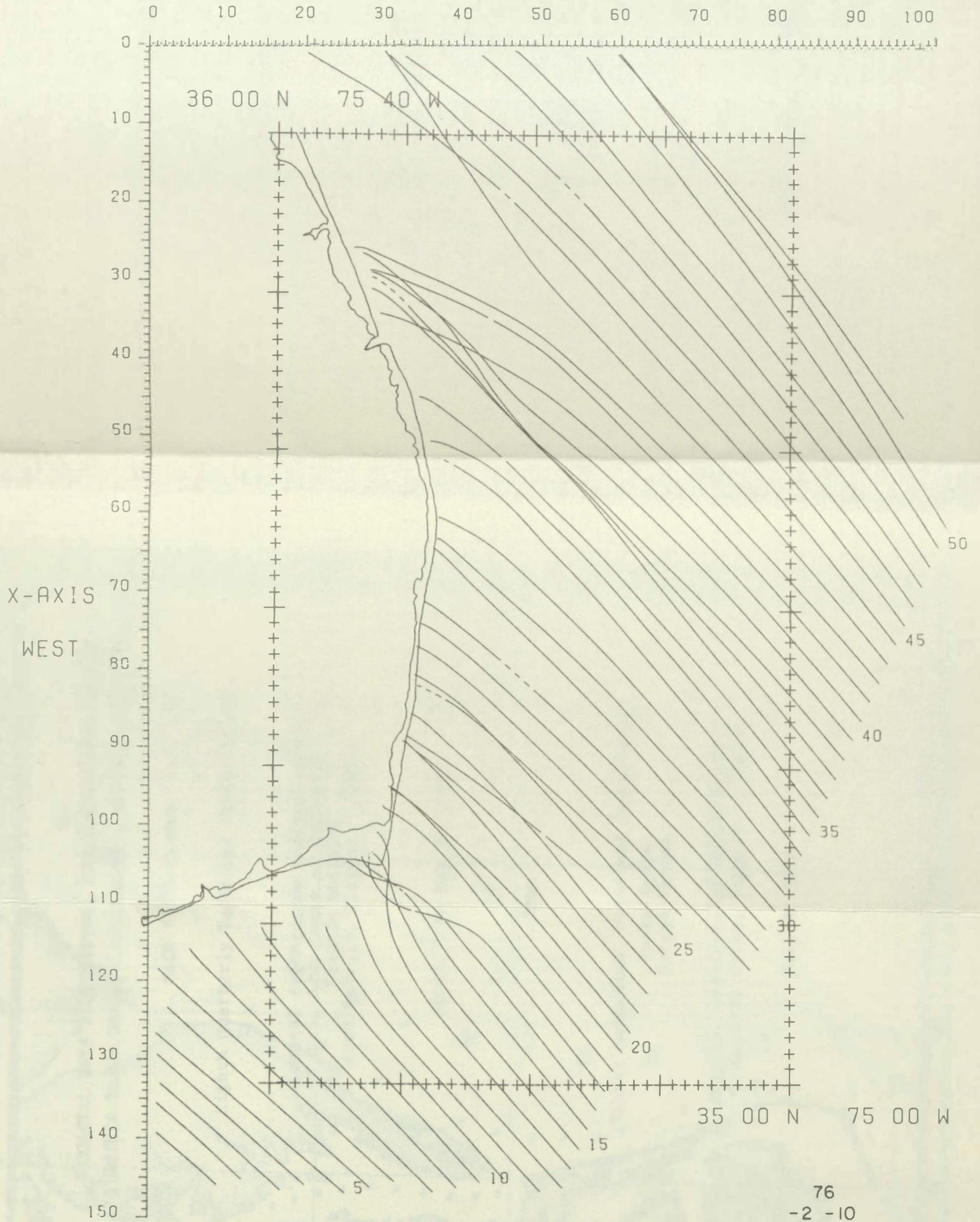
TIDE 1.8



VSWCM WAVE RAY PLOT FOR CAPE HATTERAS

TIDE 1.8

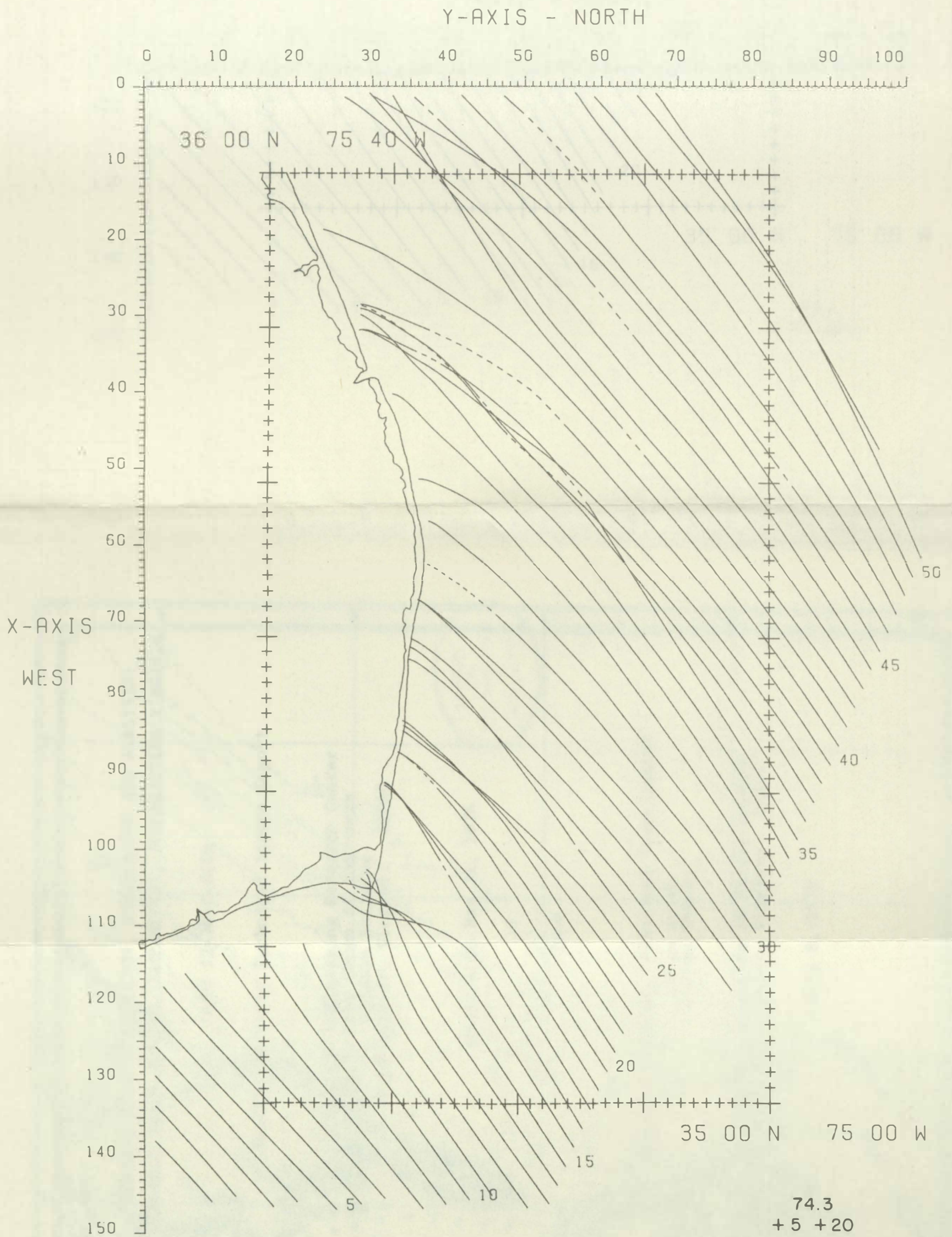
Y-AXIS - NORTH



76
-2 -10

VSWCM WAVE RAY PLOT FOR CAPE HATTERAS

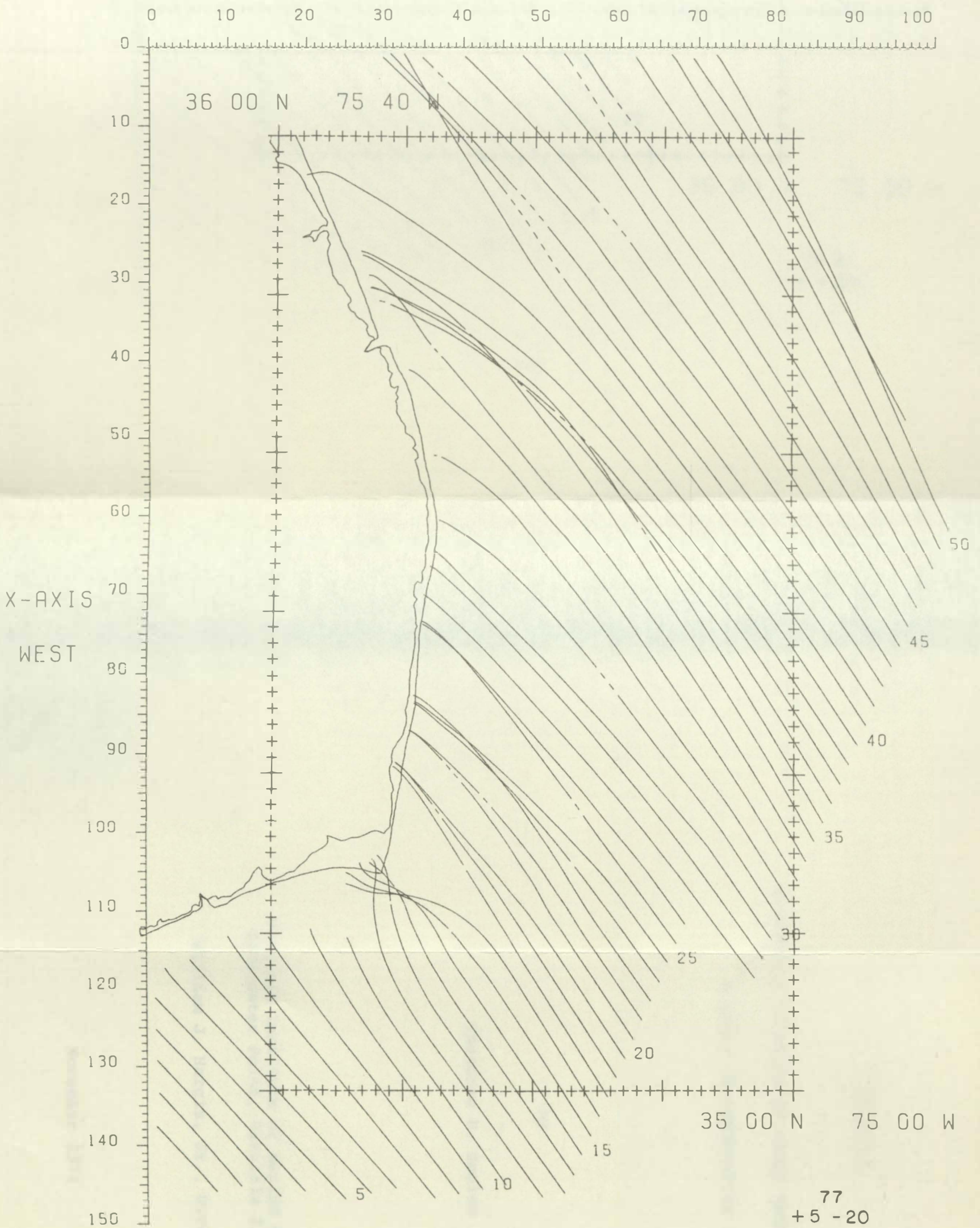
TIDE 1.8



VSWCM WAVE RAY PLOT FOR CAPE HATTERAS

TIDE 1.8

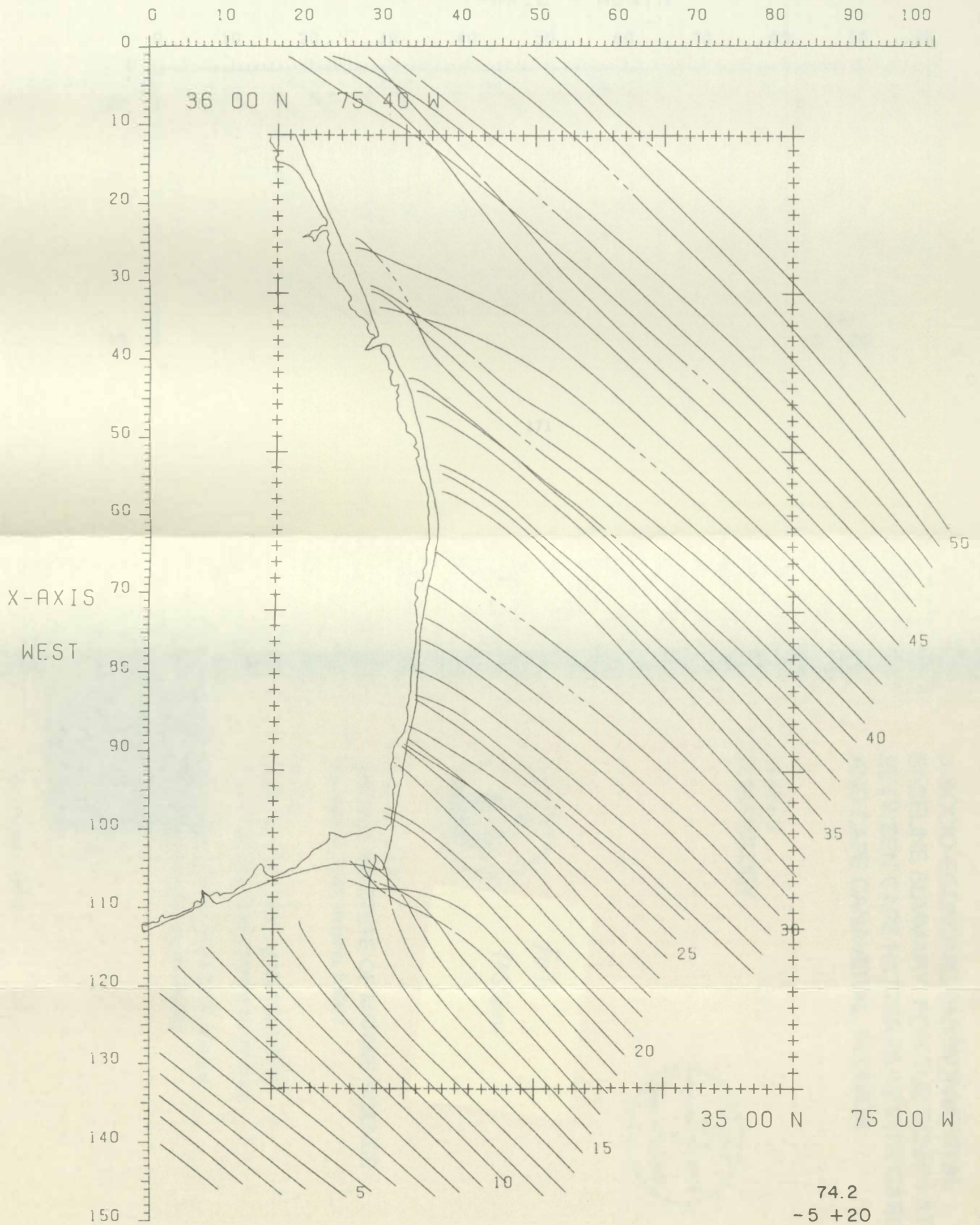
Y-AXIS - NORTH



VSWCM WAVE RAY PLOT FOR CAPE HATTERAS

TIDE 1.8

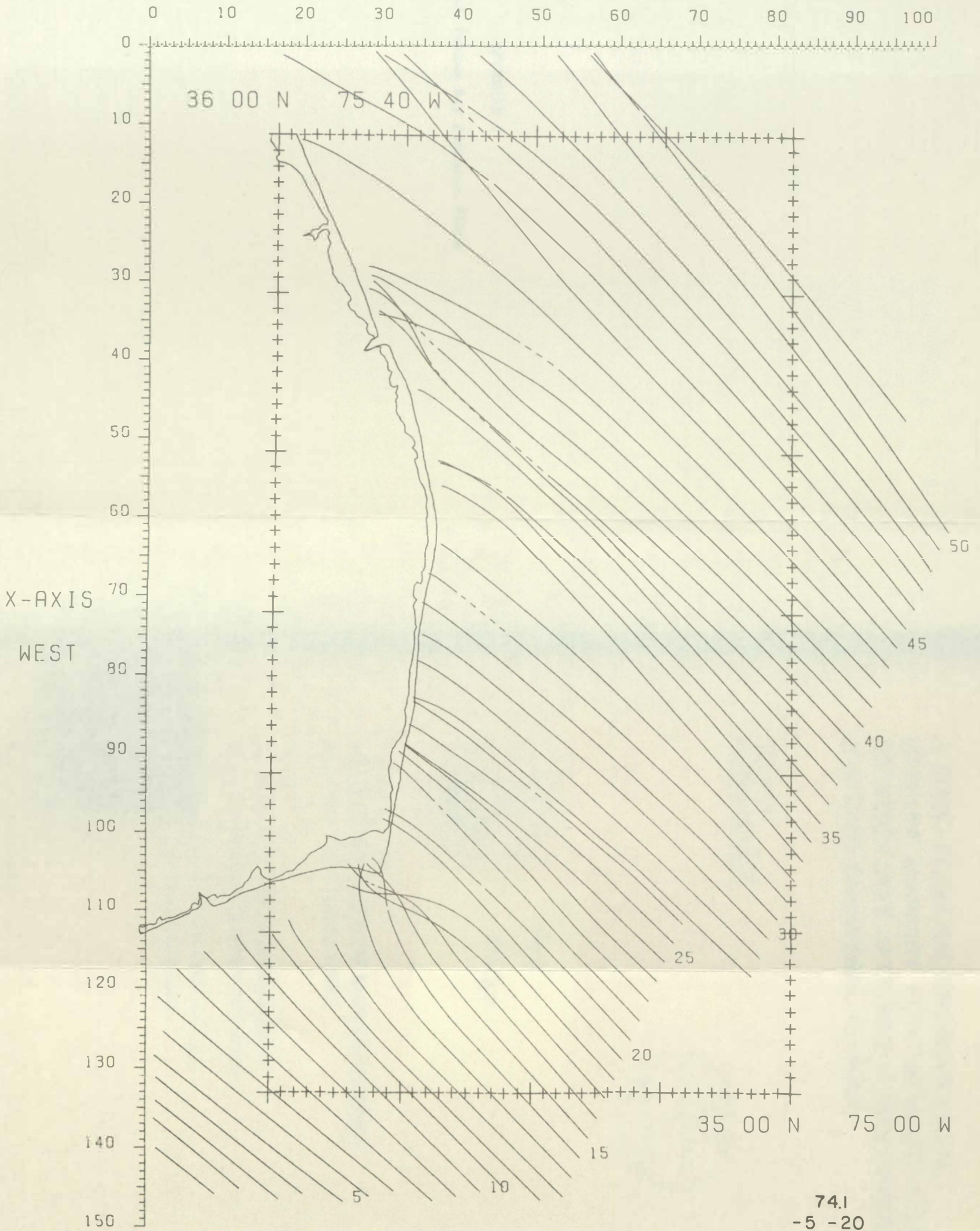
Y-AXIS - NORTH



VSWCM WAVE RAY PLOT FOR CAPE HATTERAS

TIDE 1.8

Y-AXIS - NORTH

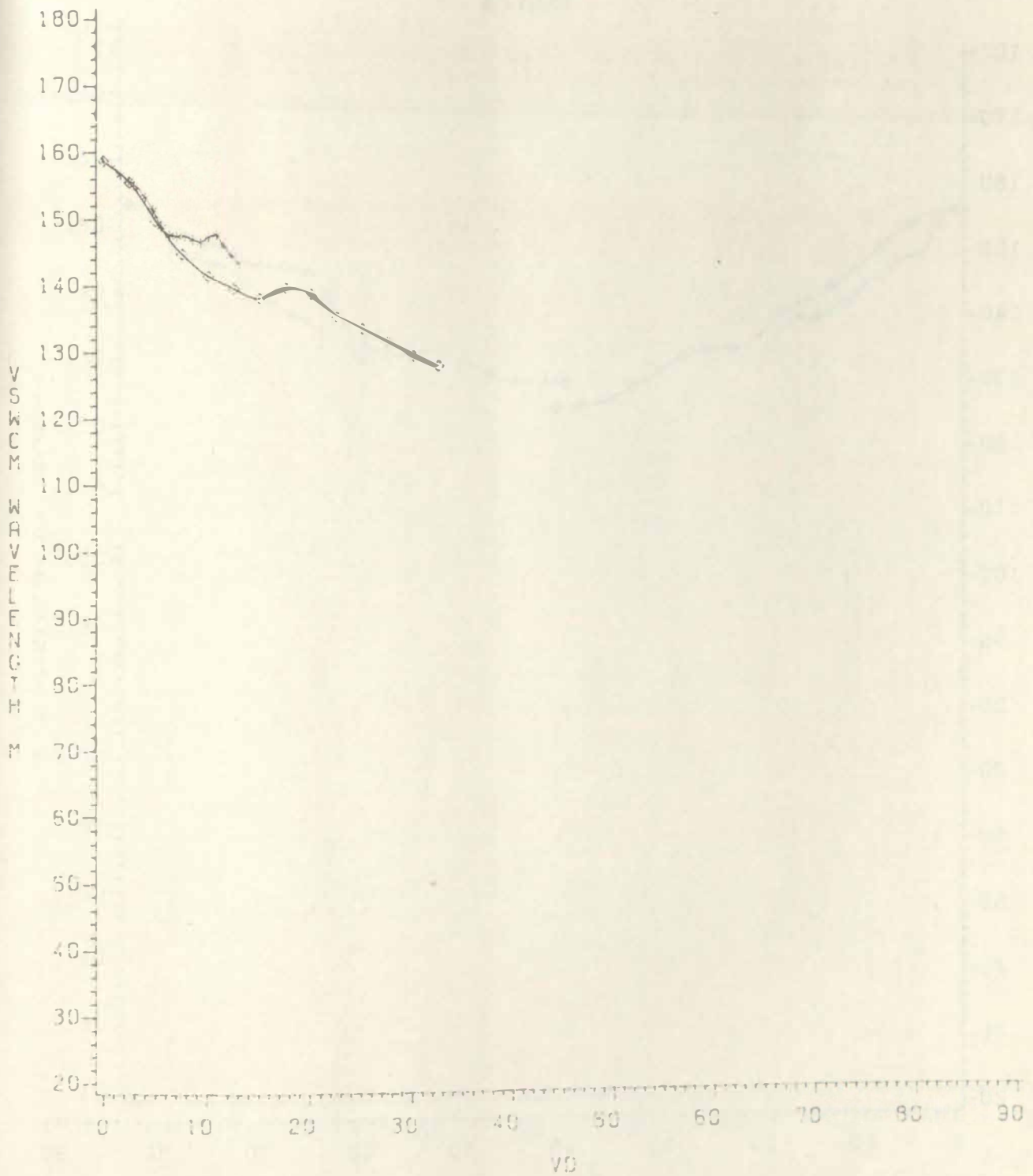


APPENDIX D

Wavelength Versus Ray Distance Plots

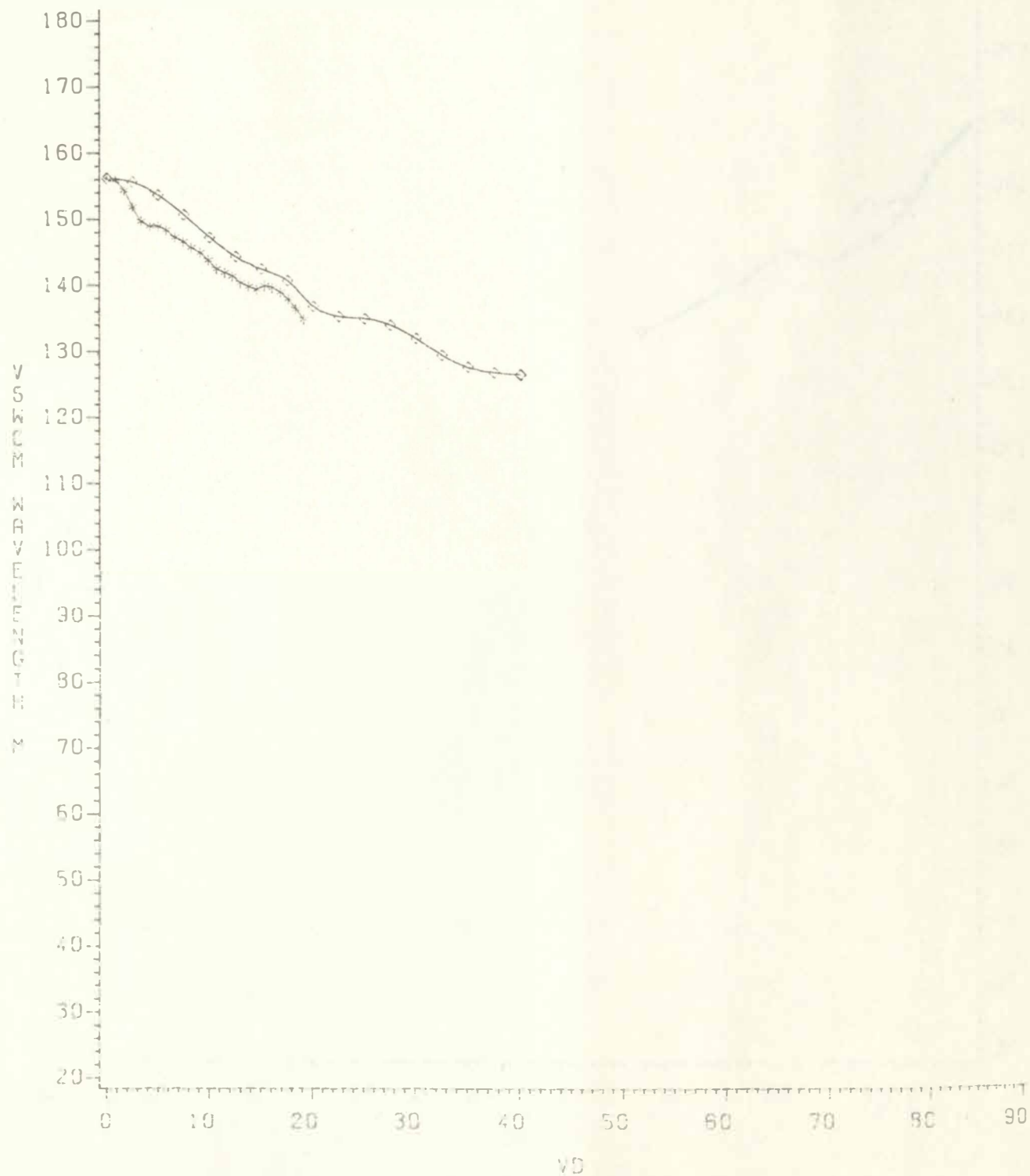
WAVELENGTH VS RAY DISTANCE

◇ = SAR OBSERVATIONS
* = MODEL PREDICTION
NRAY = 2



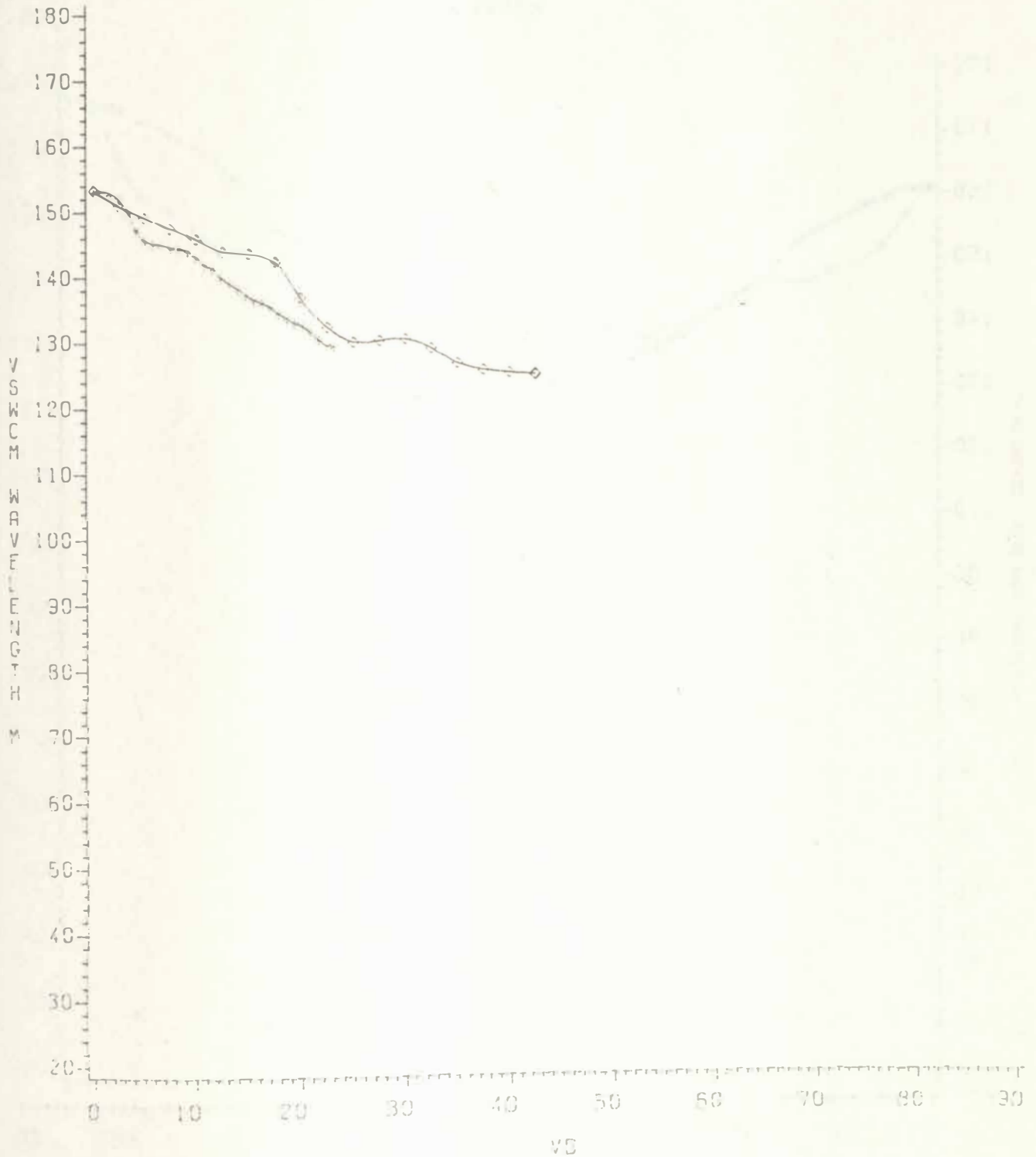
WAVELENGTH VS RAY DISTANCE

◇ = SAR OBSERVATIONS
* = MODEL PREDICTION
NRAY = 3



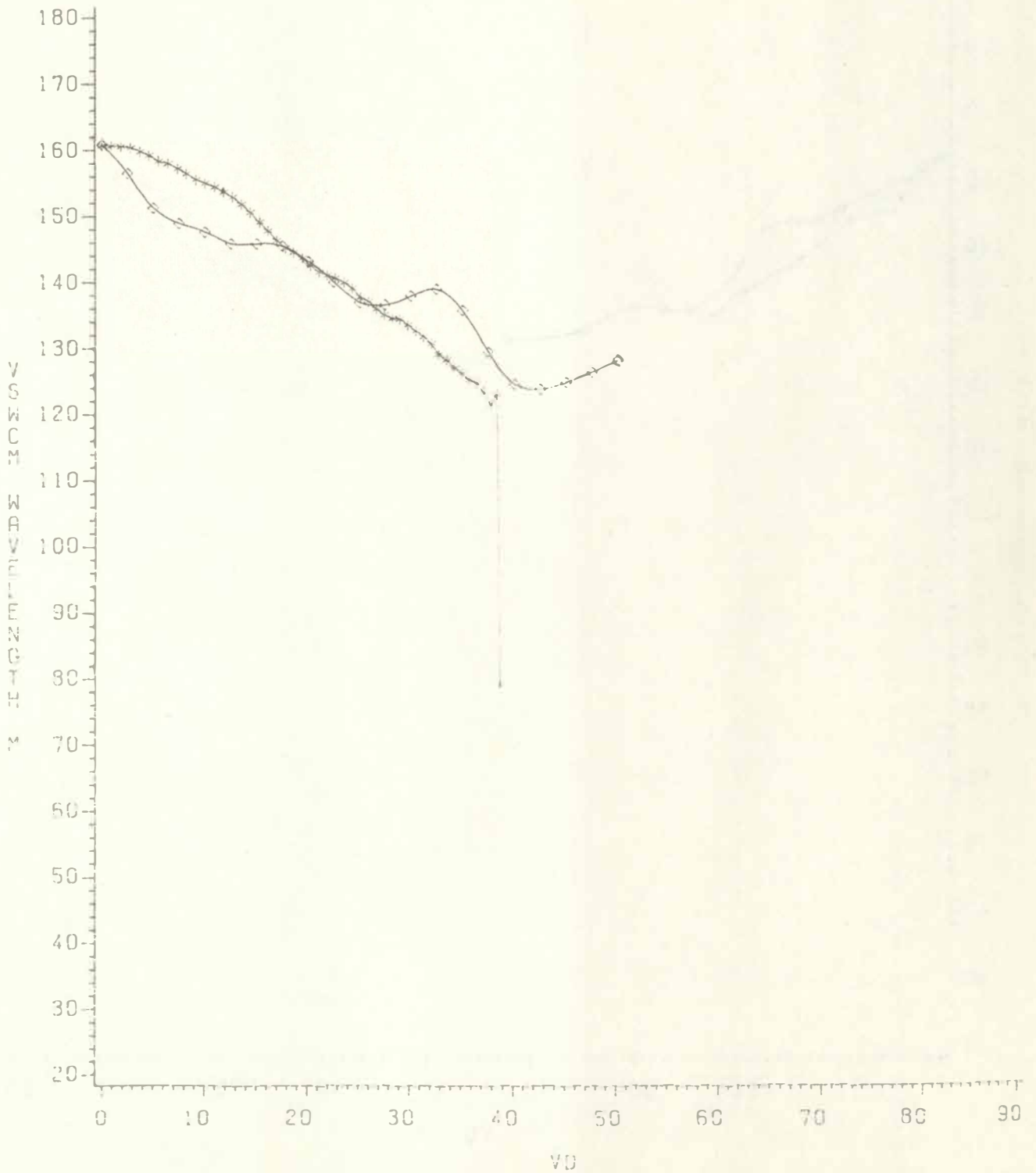
WAVELENGTH VS RAY DISTANCE

◇ = SAR OBSERVATIONS
* = MODEL PREDICTION
NRAY = 4



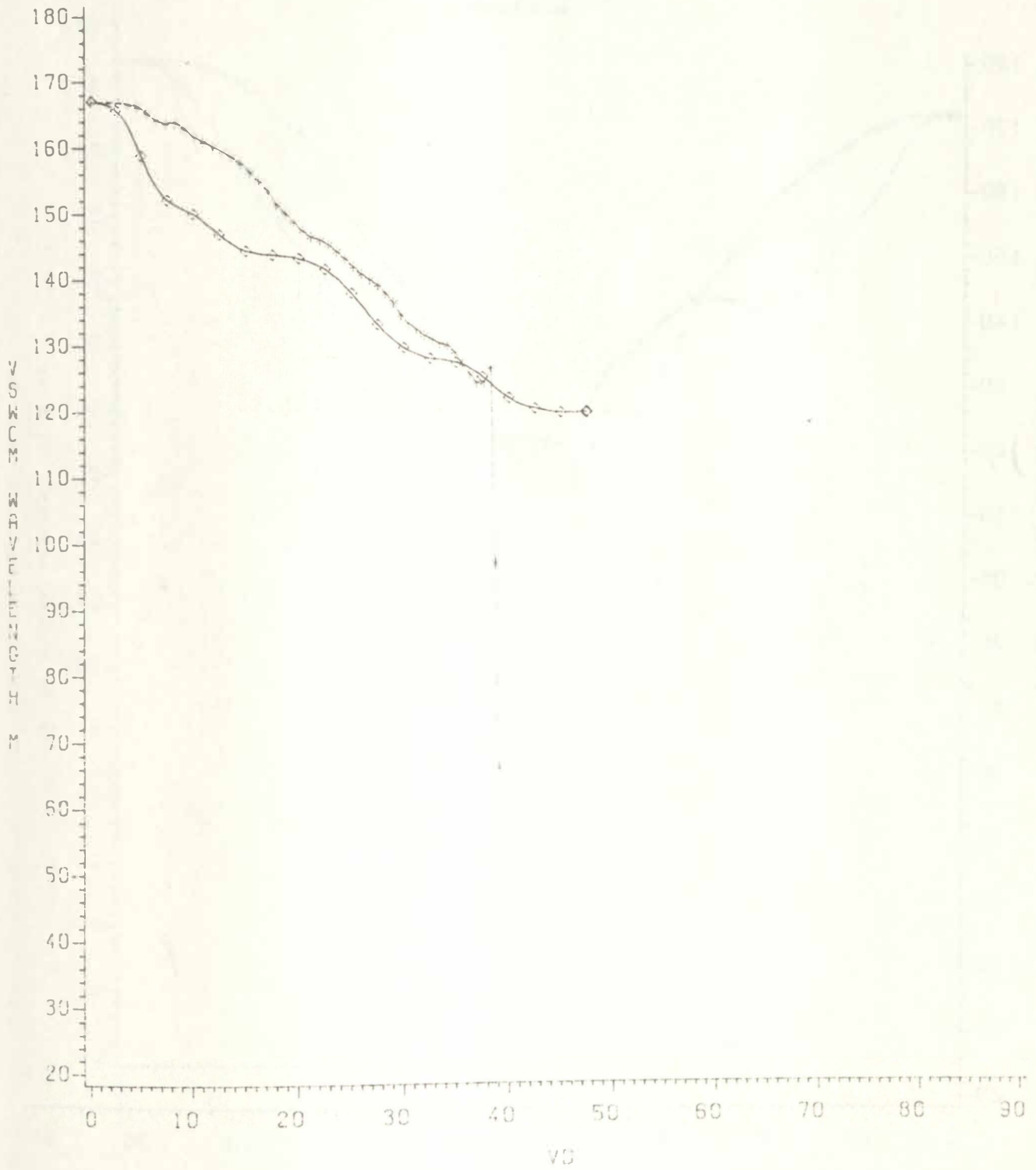
WAVELENGTH VS RAY DISTANCE

◇ = SAR OBSERVATIONS
* = MODEL PREDICTION
NRAY = 8



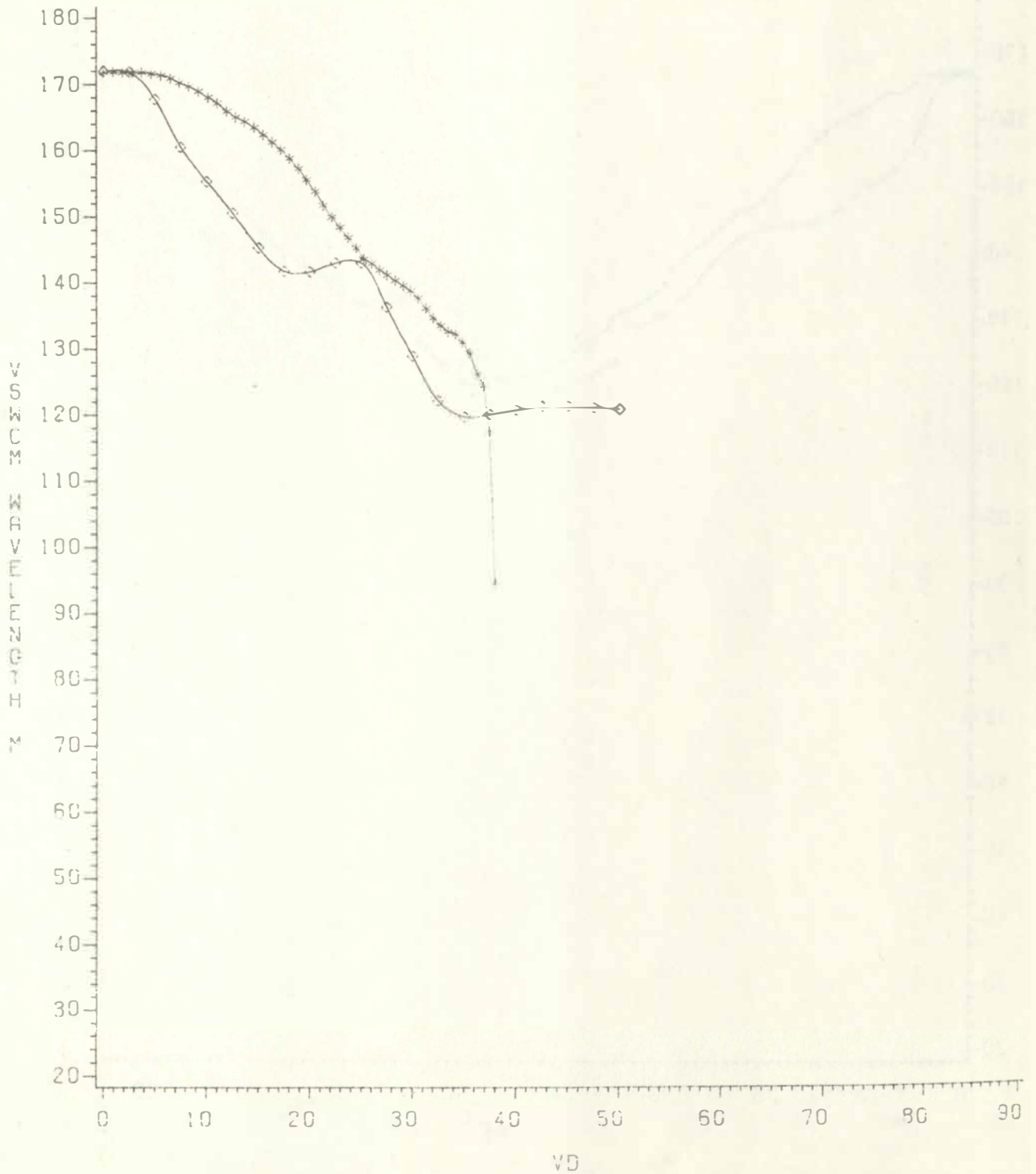
WAVELENGTH VS RAY DISTANCE

◇ = SAR OBSERVATIONS
* = MODEL PREDICTION
NRAY = 9



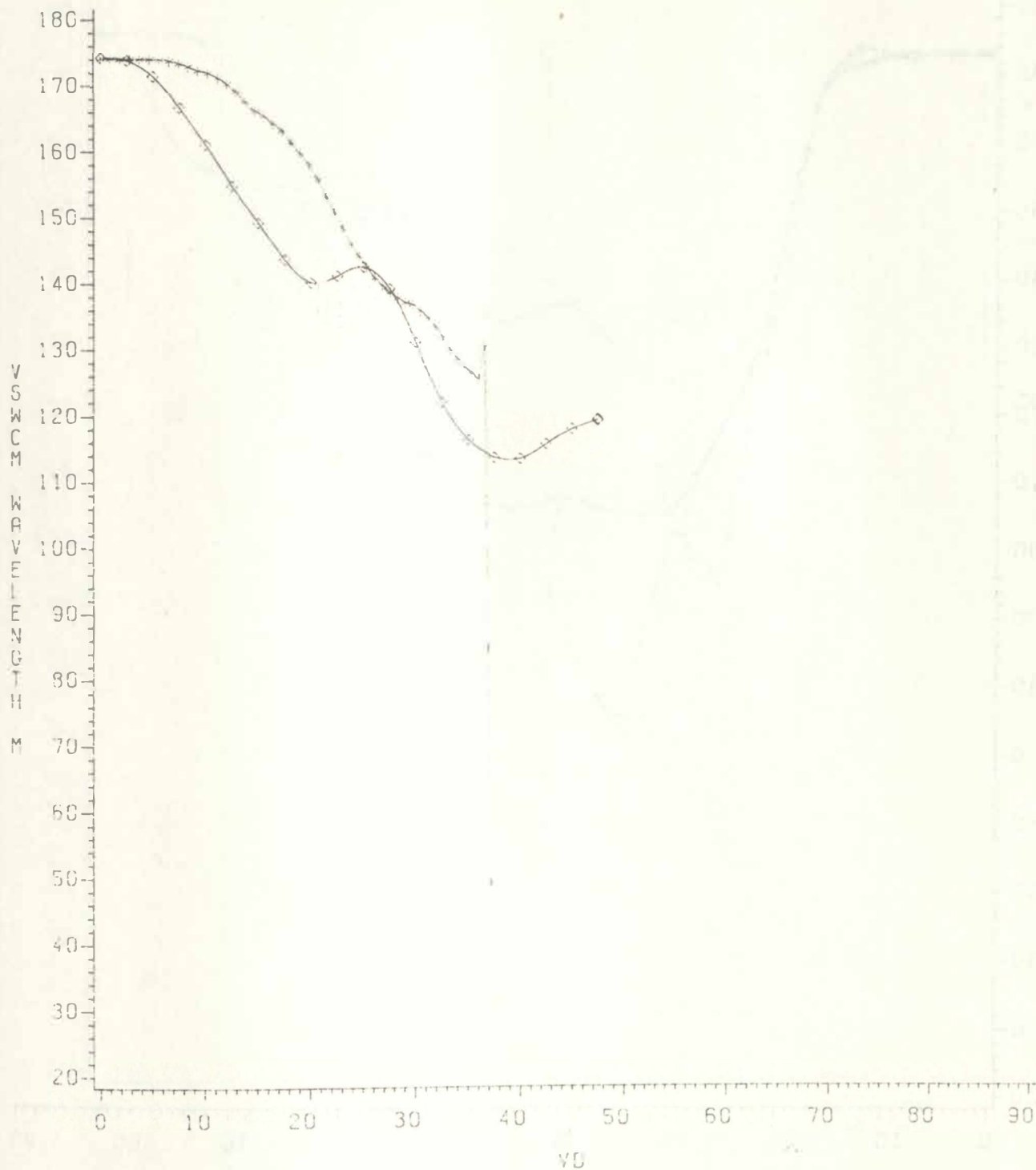
WAVELENGTH VS RAY DISTANCE

◇ = SAR OBSERVATIONS
* = MODEL PREDICTION
NRAY = 10



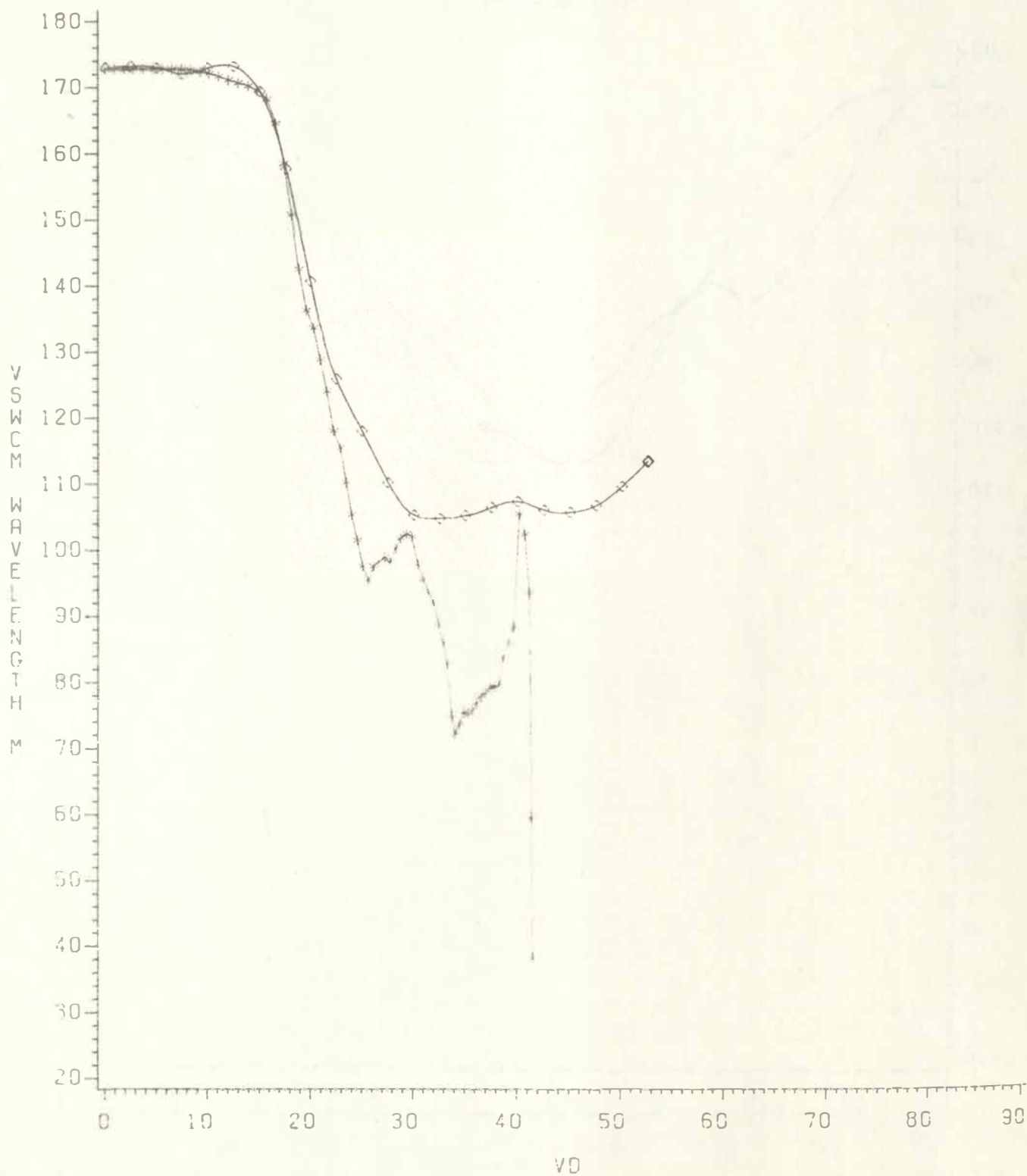
WAVELENGTH VS RAY DISTANCE

◇ = SAR OBSERVATIONS
* = MODEL PREDICTION
NRAY = 11



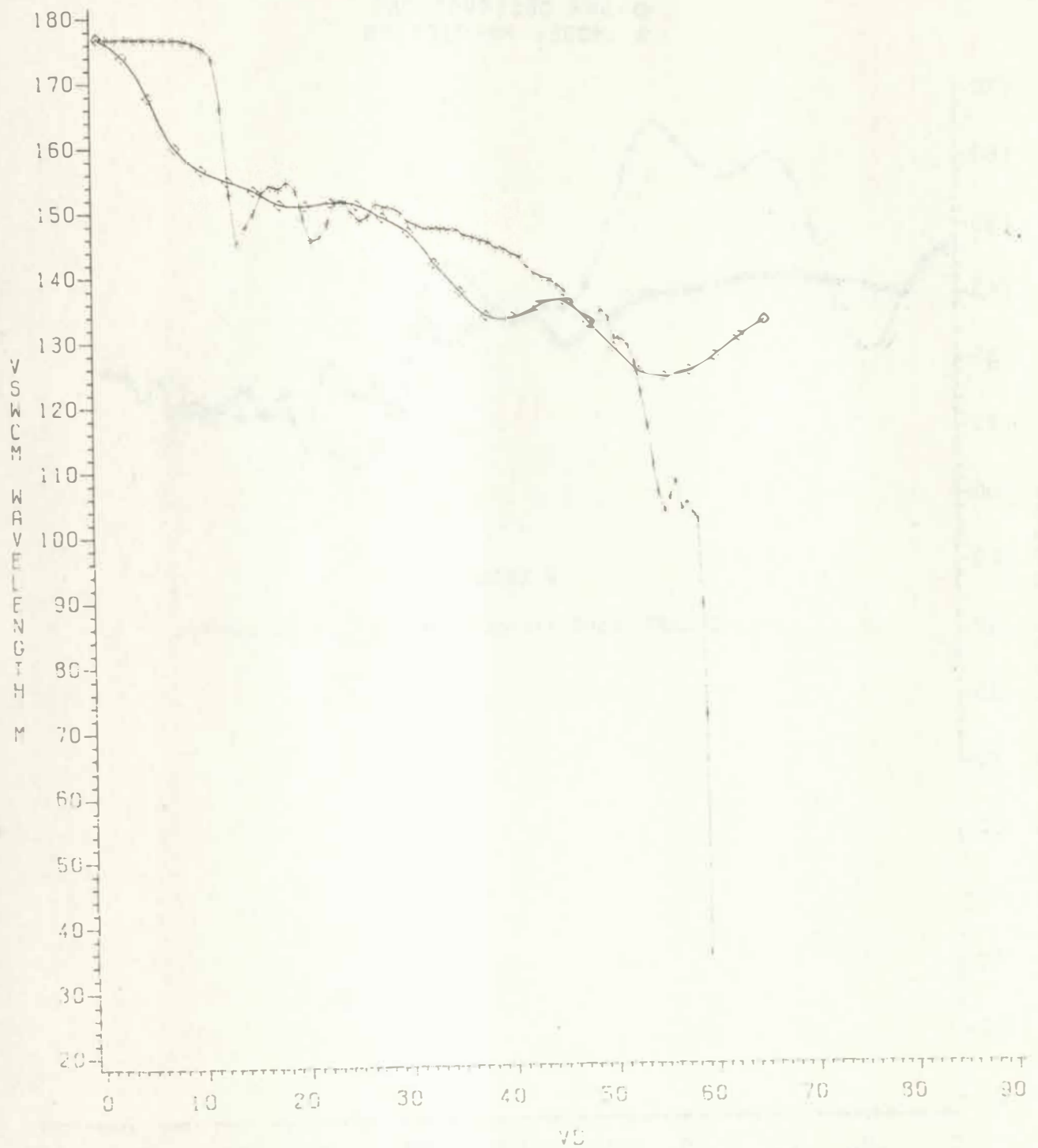
WAVELENGTH VS RAY DISTANCE

◇ = SAR OBSERVATIONS
* = MODEL PREDICTION
NRAY = 17



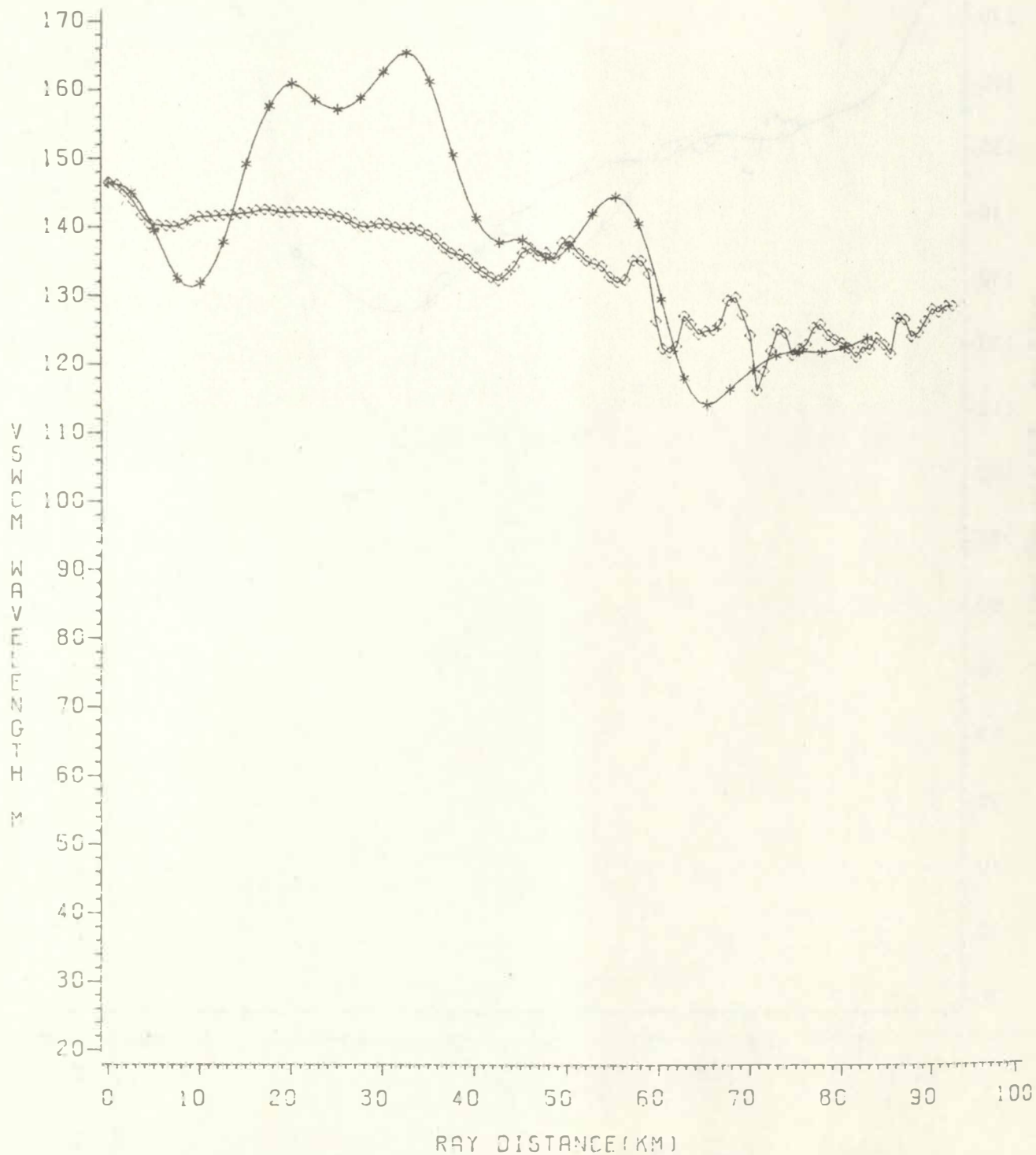
WAVELENGTH VS RAY DISTANCE

◇ = SAR OBSERVATIONS
* = MODEL PREDICTION
NRAY = 31



WAVELENGTH VS RAY DISTANCE

◇ = SAR OBSERVATIONS
* = MODEL PREDICTION



CONSTITUTION OF THE UNITED STATES OF AMERICA
ARTICLE I, SECTION 8, CLAUSE 18

Section 8181, STATUTE OF THE STATE OF CALIFORNIA
Section 8182, STATUTE OF THE STATE OF CALIFORNIA

Section 8183, STATUTE OF THE STATE OF CALIFORNIA
Section 8184, STATUTE OF THE STATE OF CALIFORNIA

Section 8185, STATUTE OF THE STATE OF CALIFORNIA
Section 8186, STATUTE OF THE STATE OF CALIFORNIA

Section 8187, STATUTE OF THE STATE OF CALIFORNIA
Section 8188, STATUTE OF THE STATE OF CALIFORNIA

APPENDIX E

Abstracts of Previous Reports Under This Project

Section 8189, STATUTE OF THE STATE OF CALIFORNIA
Section 8190, STATUTE OF THE STATE OF CALIFORNIA

COMPARISON OF SEASAT-SAR IMAGED WAVES WITH THE
VIRGINIAN SEA WAVE CLIMATE MODEL (VSWCM)

C. S. Welch (Virginia Institute of Marine Science
Gloucester Point, Virginia 23062)

J. C. Munday

G. R. Mapp

Surface waves on a SEASAT-SAR image (revolution number 974 on 3 September 1978) are clearly visible to the naked eye. These waves show changes in direction as they approach the shoreline, plausibly due to wave refraction, as the area in the image includes Cape Hatteras and Diamond Shoals.

Measurements of the length and direction of these waves have been made by comparing sub-images on a regular grid of points with lines on a Ronchi Ruling using a Zoom-Transfer Scope. The grid encompassed both deep water and the continental shelf. Intercomparison measurements have also been made on a subset of the points using Optical Fourier Transform methods. Rays have been constructed by interpolating the direction field between grid point measurements.

For comparison with these rays, model simulations with the VSWCM have been constructed using SAR deep water data for ray initialization. Sensitivity runs have been made by bracketing the starting data with estimated uncertainties. Comparisons between SAR data and model simulations show areas of agreement as well as areas of significant disagreement. Disagreements include veering of SAR rays in deep water, crossed rays in model runs, and differences in nearshore ray densities.

Hypotheses examined for these discrepancies include kinematic ray veering associated with source motion, inappropriate simulation of depth data, and wave number spectrum modification from non-linear interactions.

WAVE REFRACTION BY WARM CORE RINGS

G. R. Mapp (School of Marine Science, College of William and Mary
Gloucester Point, Virginia 23062

J. C. Munday

C. S. Welch

On September 21 and October 3, 1978 (revolutions 1232 and 1404 respectively), the SEASAT SAR imaged ocean swell propagating through the lee side of a warm core ring. Using Optical Fourier transforms, wavelength and direction have been measured for a network of grid areas on the imagery. On this grid, rays were constructed incrementally by successive interpolations of wave direction. Rays from these maps are compared with those predicted by a model for current induced refraction of deep water waves. This model is initialized with 1) incident wave data measured on the SAR imagery adjacent to the ring; and 2) current field estimated from several sources. These are a) plan views of the ring on SAR and IR imagery, b) typical values of current velocities from other warm ring studies, and c) traces of ring topography from SEASAT altimeter. Comparisons of SAR rays with model rays are based on qualitative observations of regions of convergence and divergence and quantitative measures of density of rays intersecting the perimeter of the ring.



4963

CHARTERED 1693
COLLEGE OF WILLIAM AND MARY
VIRGINIA INSTITUTE OF MARINE SCIENCE
SCHOOL OF MARINE SCIENCE



Gloucester Point, Virginia 23062

Phone (804) 642-2111

May 9, 1984

Mr. Pat DeLeonibus
NOAA/NESDIS/CESL
Oceanic Sciences Branch
Code E/RA13
Suitland Professional Center
Washington, D.C. 20233

Dear Pat:

At long last our Seasat SAR report has been published. Under separate mailing, I am sending you, as requested, 120 copies of our report, "Seasat SAR Test of the Virginian Sea Wave Climate Model" by John C. Munday, Jr., George M. Mapp, and Christopher S. Welch. This submission completes our work on and constitutes our Final Report on Contract No. NA79-SAC-00775 with NOAA/NESDIS/CESL.

In accord with permission you granted us, we have dated the report as 1982. A substantial draft of the report was completed as of mid-1982, and numerous circumstances have produced the delay until now of final publication. In terms of the scientific literature, the date 1982 is an appropriate one. Were we to have put 1984 as the date, we would have been obligated to consider in our analyses certain publications which became available between 1982 and 1984; however, contract funds were exhausted, which prevented any further analyses to be performed before final publication.

The circumstances causing the delays included my heart attack and surgery in 1982, the loss from the Institute of every person on the team of workers for the project between 1981 and 1983, and financial repercussions of these delays due to inflation. You will also remember that the original team of workers included Dr. Victor Goldsmith, who departed the Institute just before the project was to begin.

Despite these cataclysms, the finished report pleases me and Dr. Christopher Welch very much. (Mr. George Mapp, who is now in Mississippi, has not seen the absolutely final copy as yet, but I am certain he will also be very pleased.) Our analyses have produced substantial evidence that wave climate modeling and orbital SAR data yield maps of coastal wave refraction which are in close agreement. Each method is thus strengthened

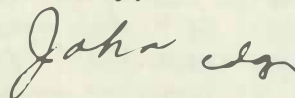
Mr. Pat DeLeonibus
NOAA/NESDIS/CESL
Oceanic Sciences Branch
Code E/RA13
Suitland Professional Center
Washington, D.C. 20233

May 9, 1984

Page 2

in its validity for future applications to coastal wave research and to coastal wave climate forecasting. Although a system incorporating orbital SARs and computerized wave climate models, integrated to produce coastal wave climate forecasts on a near-real-time basis, is still some time period into the future, this research has demonstrated its distinct feasibility for producing accurate information. In this endeavor, we are happy to have been part of the very productive Seasat program, and thank you for your support and encouragement.

Sincerely,



John C. Munday, Jr.

JCM/cdg

cc: Dr. L. D. Wright
Dr. R. J. Byrne
Dr. C. S. Welch
Mr. G. M. Mapp
Ms. J. B. Petrolia ✓